2016

Tunable hydrophoresis for bio-particle focusing and separation using dielectrophoresis-assisted and magnetophoresis-assisted hybrid techniques

Sheng Yan

University of Wollongong

UNIVERSITY OF WOLLONGONG

School of Mechanical, Materials and Mechatronic Engineering

Faculty of Engineering and Information Sciences

Tunable hydrophoresis for bio-particle focusing and separation using dielectrophoresis-assisted and magnetophoresis-assisted hybrid techniques

Sheng YAN

"This thesis is presented as part of the requirements for the award of the Degree of Doctor of Philosophy in Mechanical Engineering University of Wollongong"

September 2016

ABSTRACT

Hydrophoresis is a sheathless and passive method that utilises a pressure gradient induced by the microstructure and steric effect between the particles and grooves. In the past decade, the hydrophoresis has been intensively developed for biomedical applications. However, this technique has limitation in a wide operational range due to the lack of flexibility. That is, once a channel is fabricated, the size of particles to be focused is pre-determined by the height of the channel.

Hybrid microfluidics, as an emerging technique, fulfills the higher requirements for stable performance, versatility, and convenience, including (i) capability to process multi-target cells, (ii) enhanced ability for multiplexed separation, (iii) higher sensitivity, and (iv) tunability for wider operational range. Due to the above-mentioned features, hybrid approaches can separate cells not only based on their dielectric property, magnetic property, refractive index and compressibility but also on their volume, size and deformability. In addition, tunability of hybrid microfluidic platform relaxes the strict prerequisite of designing and fabricating the micro-channels for the specific applications.

The main purpose of this research is to develop tunable microfluidic system that can relax the strict channel height of hydrophoretic channel for a given sample. Firstly, a new concept of dielectrophoresis (DEP)-assisted hydrophoresis was proposed. This hybrid microfluidic device consists of anisotropic microstructures embedded on the top of the channel which generate lateral pressure gradients while interdigitated electrodes lay on the bottom of the channel which can push particles or cells into a higher level using negative DEP force. The polystyrene particles and cells were used to verify the tunability of the DEP-assisted hydrophoretic device. Furthermore, this method is extended to isolate plasma from whole blood. The blood cells can be focused onto the sidewalls of the channel under appropriate working condition and plasma can be collected from the middle outlet of the channel.

Stepwise, DEP-assisted hydrophoresis is modified to separate particles. Since the lateral positions of particle are such close, a sorting region is involved to lead the small particles to another sidewall of the channel. The good separation of 3 μm and 10 μm

beads was observed. Besides, due to differences in membrane potentials under the non-uniform electric field, viable and non-viable cells were separated using a modified DEP-assisted hydrophoretic device. To achieve dual function, the microposts were embedded into the DEP-assisted hydrophoretic channel. The filtration or separation mode was switched by altering the power supply voltages.

To eliminate the bulk peripheral equipment, a magnetophoresis (MP)-assisted hydrophoresis was developed, which employed the hand-held permanent magnets to modulate the particle trajectories in a diluted ferrofluid. Diamagnetic particles suspended in a ferrofluidic medium were repelled to the vicinity of the grooves by negative magnetophoretic force, and then interact with grooves to obtain an excellent hydrophoretic ordering. Besides, the magnetic and non-magnetic beads were separated based on this MP-assisted hydrophoresis.

Overall, the proposed devices are flexible and tunable systems that can control the particle movement by modulating the external physical fields, and because it is easy to operate, it is easily compatible with other microfluidic platforms that are used for downstream detection and analysis.

ACKNOWLEDGEMENTS

First of all, I would like to express my greatest gratitude to my supervisor, Professor Weihua Li, for bringing me to this fantastic field. He sheds the lights on my way to explore the unknown world. I am deeply touched and inspired by his smart vision, diligent working style, teamwork spirit, and infinite passion. Moreover, his encouragement makes me up when I encounter with the numerous technical issues. He is not only a supervisor in my research but also a lifelong friend who could always trust.

Then, I would like to thank Prof. Yonggang Zhu and his group members Dr. Huaying Chen, Mrs. Karolina Petkovic etc. at the Commonwealth Scientific and Industrial Research Organisation (CSIRO), for their great support and invaluable suggestions during my visiting at CSIRO. I much appreciated the help and support given by Prof. Gursel Alici and Prof. Haiping Du in this research.

Furthermore, I would like to show great appreciation to Prof. Xu-Feng Huang and Mr. Tiantian Jin. They kindly provided the technical training and support on the cell culture and staining which are crucial in the testing of my microfluidic devices. In addition, I am very thankful for Prof. Ronald Sluyter on donating the blood samples to my research.

Special thanks go to Dr. Jun Zhang for his rich practical experience in microfluidics and patient instruction, which really helped me fix a lot of problems at the very beginning of my Ph.D. study. Dr. Jun is my best friend who gave me a lot of help and advice in both life and work. I am also grateful to other colleagues who helped me in this or that way: Dr. Ming Li, Dr. Tongfei, Miss Dan Yuan, Mr. Qianbin Zhao and Mr. Chao Pan etc. I appreciate financial support from University of Wollongong -China Scholarship Council joint scholarships and the CSIRO Office of Chief Executive (OCE) Top-up Scholarship. Without these financial supports, I can’t come to this beautiful place to continue my higher degree study.

Last but not least, my deep gratitude goes to my family members for their support and encouragement and especially my wife, Mrs. Yuan Yuan, for her love and care in my daily life. They make this work more meaningful than it is.

TABLE OF CONTENTS

TABLE OF FIGURES

1. Introduction

1.1. Backgrounds and motivation

Lab-on-a-chip (LOC) is a concept that integrates and scales down laboratory functions into a small chip which can provide controlled conditions for scientific research or measurements. Typically, all LOC systems have several common characteristics including microfluidics and sensing capabilities [1]. Microfluidics is a multidisciplinary field intersecting chemistry, biology, physics and engineering that handles with small volumes of fluids. Microfluidics emerged in the beginning of the 1980s and the primary idea of microfluidic chips was to integrate assay operations such as detection, sample preparation, and sample pre-treatment. During last decade, microfluidic devices have experienced rapid developments to manipulate biological or synthetic micro-particles due to reduced reagent volume, faster response, lower fabrication expenses and their compactness, sensitivity, portability, and parallelisation features. To date, microfluidic techniques have been successfully employed to synthetise various bio-functionalised nanoparticles such as metallic nanoparticles [2] and other industrially relevant materials (e.g., polymer particles) [3]. Also, microfluidics is contributing to revolutionize biological procedures for enzyme revolution, DNA analysis (e.g., polymerase chain reaction and high-throughput sequencing), and proteomics. An emerging application is clinical diagnosis, especially the immediate point-of-care diagnosis of diseases. Since microfluidics-based devices have the capability to continuous processing and real-time detection of biochemical toxin and hazardous pathogens, they have the potential to be an alarm for early warning.

The manipulation (e.g., focusing, separation and sorting) of micro-particles plays a significant role in the field of biology, chemistry, and medicine. Focusing particles into a narrow stream is required in various instruments such as flow cytometry for counting, detecting, and sorting micro-beads [4]. Separation of target cells from biological samples has importance in preparative applications as well as in analytical applications where the separated cells are carefully investigated. Also, sorting micro-particles based on their sizes has a wide application in the fields of industrial production, chemical industry, environmental assessment and biological research [5]. This application can be

categorised into the active and passive manipulation of particles. Active manipulation utilises external energy such as acoustophoresis [6], magnetophoresis [7] and dielectrophoresis [8-19], whereas passive manipulation includes hydrodynamic [20-23], inertial [24], and hydrophoretic [25-29] methodologies that can be used to dominate the trajectory of particles. For active methods, the field gradient perpendicular to particle flows is generated to push particles towards the gradient direction and differentially drive them based on their size. Although active methods can precisely control particles with quite a good accuracy, their low throughput and complex structure have limited their developments and applications in wider fields. Unlike active methods can induce physical fields, passive methods utilize intrinsic hydrodynamic phenomena, which make it difficult to generate field gradient to drive particles from one side of the channel to the other one. Therefore, special channel geometries, micro-structures, and sheath flows were introduced to confine particles into a specific position [30]. However, the passive method has merits of high-throughput and simplicity, also, challenged by relatively low accuracy.

To bridge this gap, hybrid microfluidics has emerged in the past decade. Hybrid technique fulfils higher requirements for performance, versatility, and convenience, including (i) capability to process multi-target cells, (ii) enhanced ability for multiplexed separation, (iii) higher sensitivity, and (iv) tunability for a wide operational range. Due to the superior features, hybrid approaches can separate cells not only based on their dielectric property, magnetic property, refractive index and compressibility but also on their volume, size, and deformability. In addition, a hybrid device could be used in a visual feedback system, where the separation results are monitored under a microscope and the running parameters are adjusted real-time to get the optimal outcome [31]. Except for the live feedback, tunability of hybrid microfluidic platform relaxes the strict prerequisite of designing and fabricating the micro-channels for the specific applications.

Recently, an emerging technique, called “hydrophoresis”, provides new capabilities for accurate and fast manipulation of a small amount of particles. Hydrophoresis is a sheathless and passive method that utilises a pressure gradient induced by the microstructure and steric effect between the particles and grooves[29]. The concept of

hydrophoresis has demonstrated to separate micro-particles, blood cells and cell-cycle synchrony, sort adherent cells, and focus particles and cells without external fields in microfluidic channels [30]. However, once a channel is fabricated, the size of particles to be focused is pre-determined by the height of the channel.

1.2. Objectives

Normally, combining two techniques can benefit best from the two methods. So the ultimate purpose of this work is to develop a tunable microfluidic system that can relax the strict channel height of hydrophoretic channel for a given sample. The major objectives of our work are:

1) To propose the concept of DEP-assisted hydrophoresis, which enable to focus particles and cells in a high-throughput manner.
2) To isolate plasma from blood using a DEP-assisted hydrophoretic device.
3) To design and fabricate a DEP-assisted hydrophoretic separator, which separates particles and cells based on either size or surface dielectric property.
4) To develop a magnetophoresis-assisted hydrophoresis for rapid particle ordering and separation of magnetic and non-magnetic particles in a diluted ferrofluid.

1.3. Outline of the thesis

Chapter 1 provides the background and motivation of this work. A brief introduction of the latest techniques of particle manipulation in microfluidics, including active and passive methods, is presented. The objectives of the work are also discussed.

Chapter 2 introduces the mechanism of the hydrophoresis and summarises its applications in biology. Then, the fundamental physics and typical formats of hybrid microfluidic devices are discussed. The up-to-date examples on cell sorting to highlight the advantage and usefulness of hybrid microfluidics on biomedicine are also presented. Finally, the challenges and perspective on the future development and promising research direction in this field are discussed.

Chapter 3 proposes a novel concept of dielectrophoresis (DEP)-active hydrophoretic focusing of micro-particles and murine erythroleukemia (MEL) cells. The DEP-assisted

hydrophoretic platform consists of crescent-shaped grooves and interdigitated electrodes that generate lateral pressure gradients. The embedded interdigitated electrodes exert a negative DEP force onto the particles by pushing them into a narrow space in the channel where the particle-groove interaction is intensive and hydrophoretic ordering occurs. Particles passing through the microfluidic device are directed towards the sidewalls of the channel. The critical limitation of DEP operating at a low flow rate and the specific hydrophoretic device for focusing given-sized particles were overcome with the proposed microfluidic device. The focusing pattern can be modulated by varying the voltage and flow rate. The MEL cells will also be utilised to verify the effectiveness of the DEP-assisted hydrophoretic device.

Chapter 4 describes a DEP-assisted hydrophoretic method to isolate plasma from blood in a high-throughput manner. This microfluidic device consists of anisotropic microstructures embedded on the top of the channel which generate lateral pressure gradients while interdigitised electrodes lay on the bottom of the channel which can push particles or cells into a higher level using negative DEP force. Large and small particles or cells (3 μm and 10 μm particles, and red blood cells, white blood cells, and platelets) can focus at the same time in our DEP-assisted hydrophoretic device under an appropriate flow rate and applied voltage. Based on this principle, all the blood cells can be filtrated from whole blood and then plasma will be extracted. This solved the challenging problem caused by the relatively low throughput of the DEP based device.

Chapter 5 explores DEP-assisted hydrophoresis in sorting particles and cells. The device consists of the pre-focusing region and sorting region with the great potential to be integrated into advanced lab-on-a-chip bioanalysis devices. Particles or cells can be focused in the pre-focusing region and then sorted in the sorting region. The DEP-assisted hydrophoretic sorting is not only based on size but also on complex permittivity of the particles or cells of interest without any labelling. Separation of 3 μm and 10 μm particles is achieved. According to the different dielectric property of viable and nonviable Chinese Hamster Ovary (CHO) cells in the customised DEP buffer, the viable CHO cells are sorted from cell sample. To achieve dual function, the microposts are embedded into the DEP-assisted hydrophoretic channel. The filtration or separation mode was switched by altering the power supply voltages.

Chapter 6 reports a work to tune and improve the dynamic range of hydrophoresis device using magnetophoresis. In this work, a novel approach is presented to fabricate the lateral fluidic ports, which allow the flipped chip to remain stable on the stage of microscope. Diamagnetic polystyrene microparticles suspended in a ferrofluidic medium is repelled to the lower level of the channel by negative magnetophoretic force, and then interact with grooves of microchannel to obtain an excellent hydrophoretic ordering. The effects of (i) flow rate, (ii) particle size, (iii) magnetic susceptibility of the medium, and (iv) number of magnets on the particle focusing efficiency are also verified.

Chapter 7 proposes a high-throughput, sheathless, magnetophoretic separation of magnetic and non-magnetic beads in a hydrophoretic channel, and also report on an interesting phenomenon where the same magnetic beads in the same microchannel, but with different setups, has different particle tracing; a binary mixture of magnetic and non-magnetic beads in a diluted ferrofluid, is then fed to the channel. These magnetic beads are focused near the centreline of the channel by exploiting positive magnetophoresis and microvortices generated by grooves, whereas the non-magnetic beads are focused along the sidewalls of the channel by negative magnetophoresis and hydrophoresis. These magnetic and non-magnetic beads are separated in a wide range of flow rates (up to 80 µl min^{-1}).

Chapter 8 highlights the major findings and contribution of this thesis, as well as proposing several directions for future work.

2. Literature Review

The rising problem related to lifestyle-related diseases and aging of the population has attracted a lot of researchers' concern. There is a greater demand for a new technique that can perform the immediate point-of-care diagnosis of diseases and be operated by nonprofessional medical staff. The emerging microfluidics provides the possibility to fill this gap. The microfluidic platform enables to integrate several laboratory procedures into a single monolithic chip, which can reduce miscellaneous labour. Since small reagent volume is involved, fast response of microfluidic devices can achieve real-time detection. In this review, the progress of hydrophoretic devices and hybrid techniques in the manipulation of particles was reviewed.

2.1. Hydrophoresis

Hydrophoresis is a sheathless and passive method that utilises rotational flow induced by anisotropic obstacles. The concept of hydrophoresis has been demonstrated to separate micro-particles, blood cells, and adherent cells, and focus cells without sheath flow and external physical field.

2.1.1. Principle of hydrophoresis

Hydrophoresis utilises steric hindrance mechanism and secondary flow to manipulate particles (**Error! Reference source not found.**). The low resistance provided by grooves in the cross section, fluid will fill the grooves and induce a transverse movement within the channel. The pressure of the fluid in the central grooves is higher than that at the sides. This anisotropic structure generates a pressure gradient from the central grooves to the sides which induces helical recirculation [4], where the helical streams rotate like a gear following a sequence of upwards, deviation, downwards, focusing, and then upwards again (**Error! Reference source not found.**b).

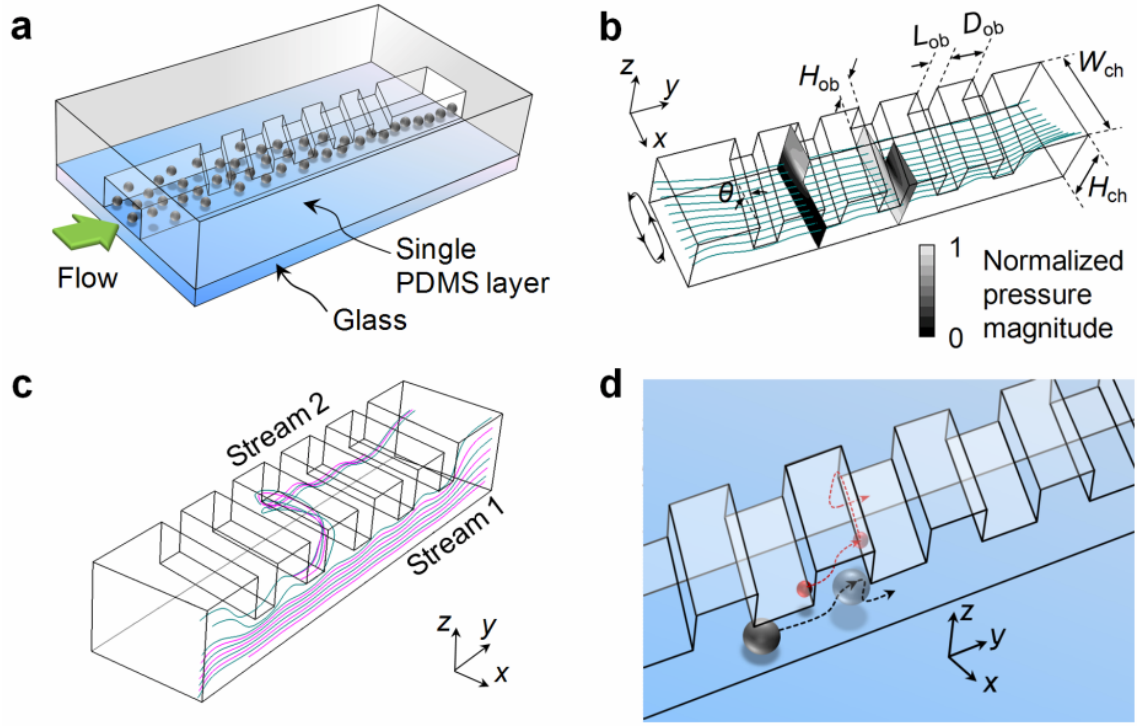

Figure 2-1 Hydrophoretic separation principle. (a) Overview of hydrophoretic device. b) and c) Simulated pressure gradient and streamlines in the device. (d) Different particle ordering according to particle size by steric hindrance mechanism [32].

Particles suspended in the medium have helical motions that follow the flow of the fluid (the stream 2 in **Error! Reference source not found.** c). Particles also experience four stages in each cycle: deviation, downwards, focusing, and upwards. This deviation in the flow brings particles to one side of the channel where the velocity is relatively low in bulk flow. The particles move down in downwards flow and then the focusing flow brings the particles to the other side of the channel. Meanwhile, particles will migrate along the bottom of the channel and then move up following upwards flow. In this way, the particles will move back and forth in the channel.

Hydrophoresis utilises a steric hindrance mechanism to separate or focus particles under a pressure gradient induced by anisotropic flow resistance [26]. The steric effect arises when atoms in a molecule are brought too close together. Atoms are likely to occupy preferred positions rather than overlap each other, a principal that works well in micro-scale physics. As a giving particle (*D* in diameter) reaches the proximity of the sidewall, then rotational flow pushes it upward, driving it to align with the surface of the groove

(the large particles in **Error! Reference source not found.** d). When a particle is comparable in size with the height of the channel ($H_g = H_{ch}-H_{ob}$), steric hindrance prevents a particle following the rotational flow. Thus, particles keep moving near the sidewall instead of migrating back and forth in the channel. This hydrophoretic ordering is largely determined by the height of the channel. Where $D/H_g > 0.5$, the grooves begin to hinder particles following the Dean flow induced by anisotropic microstructures and causes hydrophoretic ordering [26]. In short, the interaction between particle and groove deflects those particles that are almost the same size as the height of channel from their normal trajectories and leads to a new equivalent flow path which is called hydrophoretic ordering.

2.1.2. Size-based hydrophoretic separation

Microfluidic separating and sorting micron-sized particles have significant applications in clinical diagnostics, chemical, and biological analysis, and environment detection [5]. Microfluidic platforms have the potential to be miniaturized and have the advantages of portability, low cost and user-friendliness over the traditional instrument. Further, the use of microchip allows for the integration of multiple technologies into one device for manipulating and probing particles or cells and the mass production of microchips reduce the cost per analysis significantly. In active microfluidic separation such as DEP, magnetic, and optical methods, the force exerting on particles is highly dependent on their volume, dielectric and magnetic properties and refractive index. Unlike active methods, passive methods utilize intrinsic hydrodynamic phenomena, which make it difficult to generate field gradient to drive particles from one side of the channel to the other one. Therefore, special channel structures and sheath flows were introduced to confine particles into a specific position. Hydrophoresis utilised anisotropic obstacles patterned on the top and bottom of the channel to induce pressure gradients, which enabled precise particle separation in the size ranging from 8 to 15 μm [27]. 8-15 μm beads assuming hydrophoretic ordering had their own equivalent positions (**Error! Reference source not found.** a, b). Particles were separated according to their different distributions in the hydrophoretic devices. With such high size-selectivity, the diameters of 10 μm beads with a high coefficient of variance of 8.7% were successfully predicted using a linear fitted curve, compared with a conventional laser diffraction method. Also,

the selectivity can be downscaled into sub-micrometer scale. Even in sub-micro scale, hydrophoretic device still can separate binary mixtures: large particles in focusing mode are sorted from relatively smaller particles in free flow (**Error! Reference source not found.** c) [32]. 99.6% of 0.5 μm particles were collected after separation, while the purity of 1.1 μm particles was enhanced from 27.8% to 41.7%. Besides, the rule for hydrophoretic ordering, $D/H_g > 0.5$ still validate in sub-micro scale (**Error! Reference source not found.** d, e).

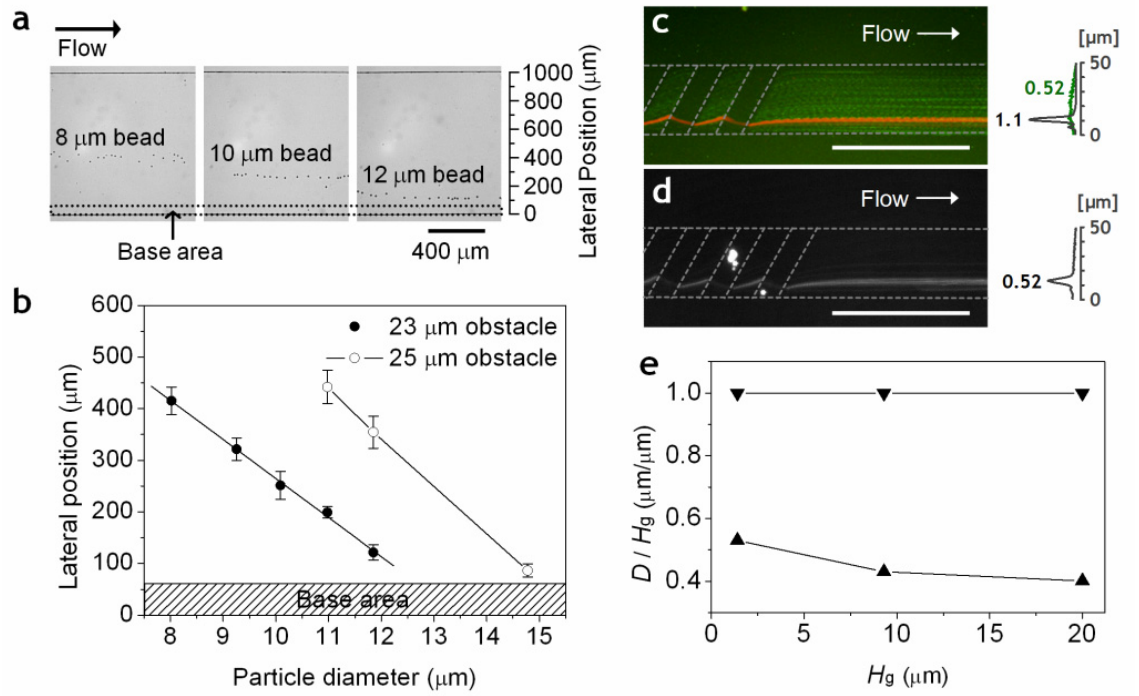

Figure 2-2 Size-dependent hydrophoretic separation. (a) Different lateral positions of particles in the hydrophoretic channel. (b) The particle diameter versus the lateral position [27]. (c) Microscopy image showing the separation of 0.5 and 1.1 μm beads. (f) Particle trajectories of 0.5μm beads. (e) The ratio of particle diameter to channel height H_g versus H_g [32].

2.1.3. Blood cell separation

Human blood including leukocytes or white blood cells (WBCs), erythrocytes or red blood cells, and platelets and plasma [33]. WBCs play a significant role in the immune system, account for 1% of whole blood cells, and range from 7 to 30 μm in size. Red blood cells have a discoid shape and are 7 to 8 μm in size; they are the most common

cells, accounting for 98% of all blood cells [34]. Platelets are 1 to 3 μm in size and are responsible for formatting blood clots [35]. Typically, precise and rapid isolation of blood cells is in demand in clinical diagnosis. To address this requirement, a new hydrophoretic filtration device integrated with slanted obstacles and filtration obstacles was proposed (Figure 2-3) [36]. The WBCs and red blood cells can first be focused in the focusing region as they having a smaller size than the channel height (*H*). In the following step, the channel height (*h*) is set between the diameters of WBCs and red blood cells. Red blood cells smaller than the channel height remain their lateral position, while WBCs would not pass through the filtration region and be driven to filtration pore. After filtration, 210-fold WBCs were enriched from blood in just a single round of separation. The high enrichment was achieved, which is highly dependent of deformation of red blood cells. Later, the effort to isolate platelets from blood was proposed using wide-channel hydrophoresis (Figure 2-4)[35]. The major reason that uses wide channel is to augment throughput capability and reduce the stress shear on the cells. WBCs and red blood cells satisfy the hydrophoretic ordering, thereby staying near sidewall 2. However, the steric hindrance for platelets is negligible so they can move back and forth in the wide-channel hydrophoretic devices. After a single round sorting, the purity of platelets from collection outlet reached 36.7% from their initial purity of 3.1%. The purity of 82.8% was achieved in the second round sorting. Moreover, the simplicity of such kind hydrophoretic devices facilitates parallelization to further increase the throughput.

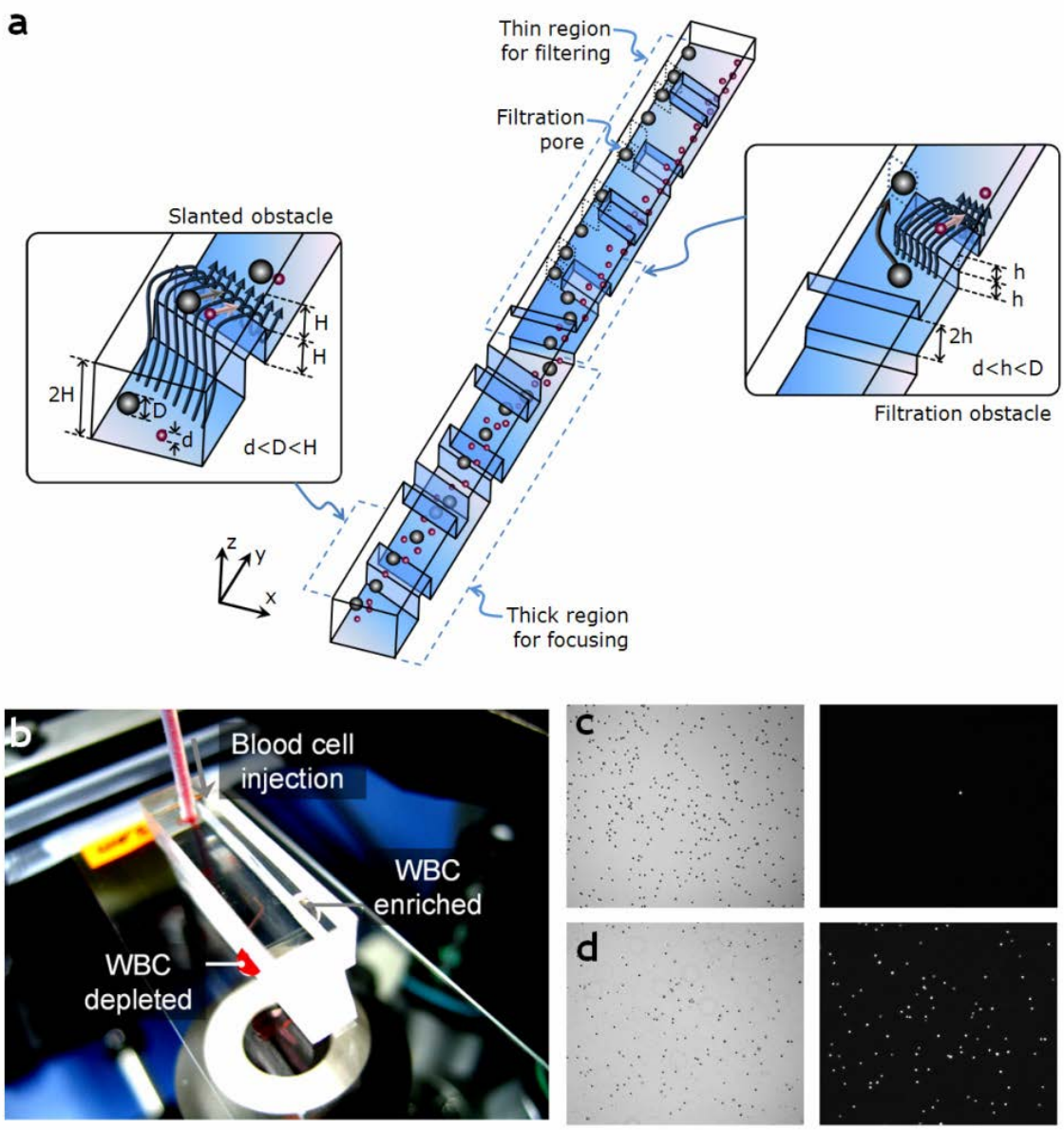

Figure 2-3 Isolating WBCs from blood using hydrophoretic filtration. (a) Overview of hydrophoretic filtration device, consisting of focusing and filtration region. (b) The image of blood separation in hydrophoretic filtration device. Bright-field (left) and fluorescence (right) images showing blood cells before (b) and after (c) separation [36].

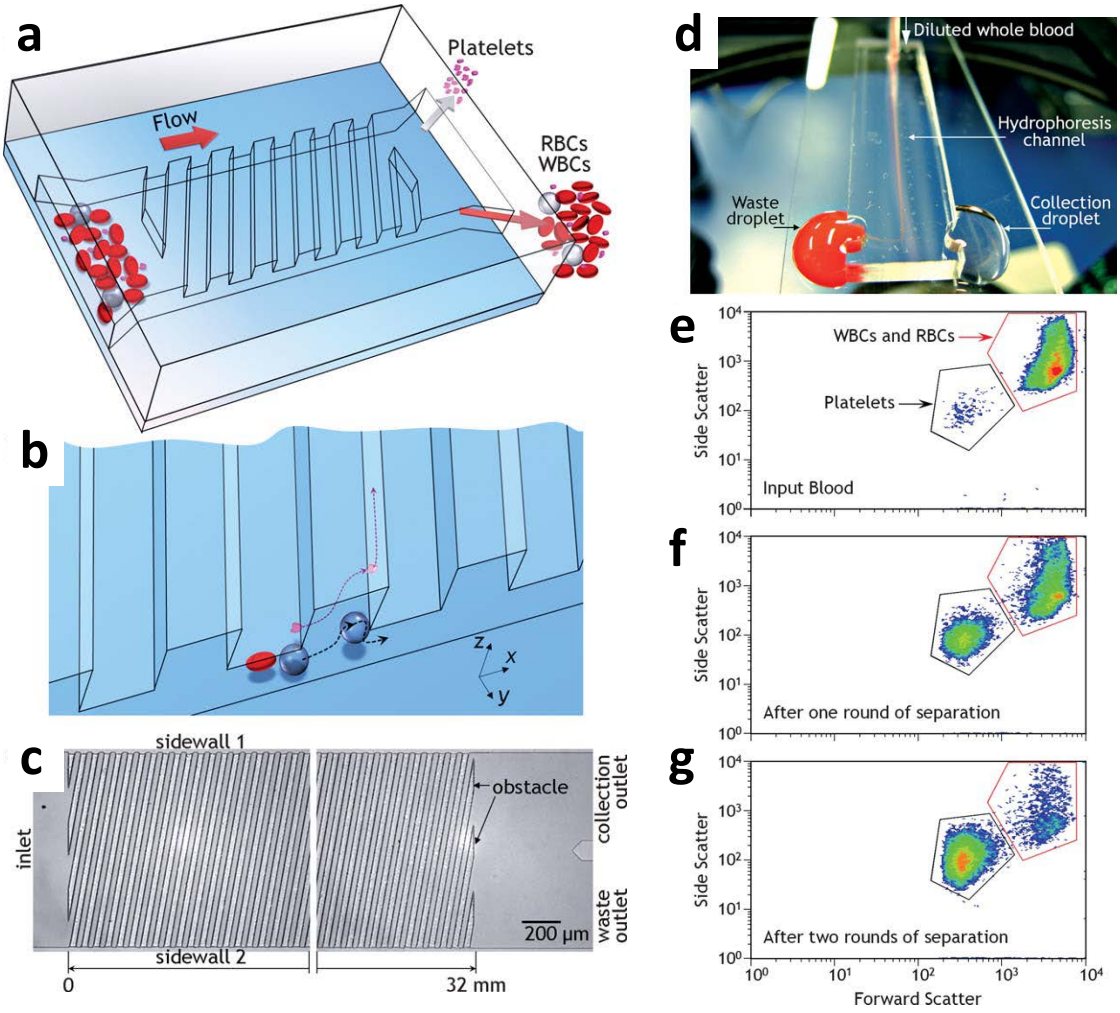

Figure 2-4 (a) Schematic illustrating plasma separation in a wide-channel hydrophoresis channel. (b) WBCs and red blood cells assuming hydrophoretic ordering can stay near the sidewall 2, while platelets remain unfocused, separated from blood. (c) The optical image of hydrophoretic channel with anisotropic obstacles. (d) The image of separation of platelets in the wide-channel hydrophoretic device with a sample inlet and two outlets. (e) Unsorted, diluted blood sample. Separation results from collection outlet after one round (f) and two rounds (g) of hydrophoretic sorting [35].

2.1.4. Cell sorting by cell rolling

Cell-affinity chromatography utilises cell-surface molecular interaction of antibody coated on the substrate to select target cells. Target cells can be captured and recovered by elution in cell-affinity microfluidic device. This method has been extensively demonstrated to be a powerful tool to sort CD34+ cells using CD34 antibody [7] and

circulating tumor cells (CTCs) using epithelial cell adhension molecule (EpCAM, CD326) [11]. The group of Nagrath [37] has proposed a novel CTC-chip for isolation of CTCs from cancer patient blood. The micro-chip comprises a micro-post array, which is chemically coated with EpCAM. Once the blood flows through these micro-posts, the CTCs were trapped on the surface of the column and normal blood cells could freely pass through these micro-posts. The input flow rate is the key parameter for cell capture, which determines formation and dissociation of cell-surface adhesion. Thereby, the relatively low flow rate (1 ml/h) was operated in this muicrofluidic device. The cells that can be trapped highly depend on the column surface coated with affinity molecules that often occupies the major percentage of the expense. Typically, the specific antibody for cell sorting is pretty expensive than micro-chip materials (PDMS). Additional, releasing the captured cells requires the extra elution, which will dilute the cells concentration and complicate the operation process.

Recently, Choi et al. [38] proposed a novel separation process known as “deterministic cell rolling” that combines transient cell-surface molecular interactions to hydrophoresis in a continuous manner without elution step (**Error! Reference source not found.**). The device consists of parallelizable microfluidic channels that work simultaneously to increase the effective contact of cells with affinity surfaces. Meanwhile, parallelisation of sorting channel overcomes the limit of low sample volumes processed in the previous approach. First of all, the device was incubated with P-selectin solution. The cells can be focused by the focusing ridges in the narrow channel. When entering the widened channel, the cell velocity goes down, thereby causing formation and dissociation of cell-surface molecular adhesive bonds at this stage. HL60 as a target cell can roll on the ridges, moving towards the gutter side, while non-target cells (K562) could not roll on the ridges, staying along the focusing side (**Error! Reference source not found.** a). As a negative control (no P-selectin), there were no observable cell-surface rolling and the cells were not sorted. Also, with the increase of the concentration of P-selectin, cell rolling was enhanced and the sorting efficiency was improved. The sorting performance also relied on the flow rate as the cell rolling is a trade-off between formation and dissociation of adhesion. High throughput would deteriorate the sorting efficiency (**Error! Reference source not found.** c). After sorting from a heterogeneous mixture, HL60 cells were collected from Outlet A with the purity of 95.0±2.8%, while the output

at Outlet B comprised 94.3±0.9% of K562 cells (**Error! Reference source not found.** d).

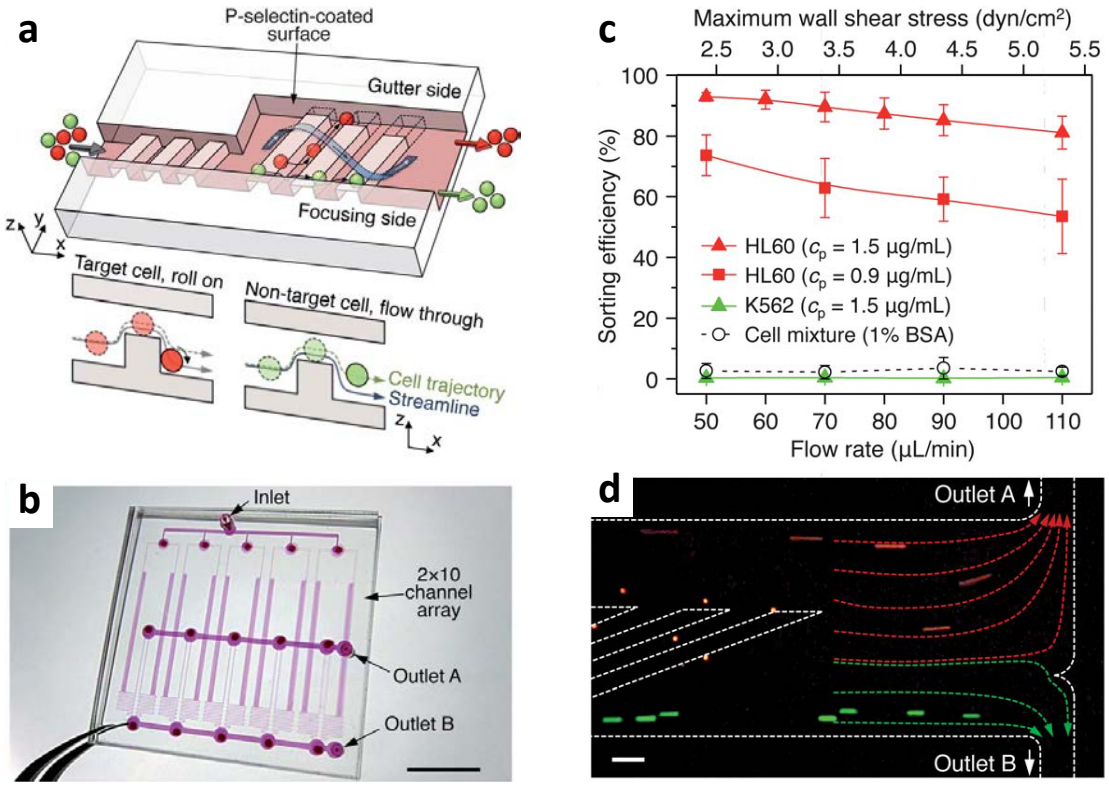

Figure 2-5 Parallelizable sorting device. (a) Schematic of a single channel consisting of narrow focusing ridges and wide sorting ridges (Top). Cross-section views of the wide sorting channel along x-axis, showing cell trajectories of adherent and non-adherent cells, respectively (Bottom). (b) The 2 × 10 channel array in a 3.5 × 3.5 cm square device. (c) Effect of shear stress and P-selectin concentration (c_p) on the sorting efficiency of HL60 and K562 cells. (d) Optical image showing the sorting of HL60 (red) and K562 (Green) at shear stress of 3.4 dyn/cm^2 and c_p=1.5 μg mL^{-1} [38].

2.1.5. Hydrophoretic focusing

Typically, most of the microfluidic techniques have the capability of 2D hydrodynamic focusing, which makes the microflow cytometer possible. However, 3D focusing normally requires at least four inlets to sheathe a sample flow into a specific stream [39]. To overcome the limitations of conventional hydrodynamic focusing methods, active microfluidic sheathless focusing approaches have been developed. Yu *et al*. [40]

utilised elliptic-like micro-channel patterned with interdigitated electrodes on the circumference of the channel to achieve 3D focusing of microparticles by dielectrophoresis (DEP). Shi *et al*. [6] used interdigitated transducers evaporated on a piezoelectric substrate to induce the standing surface acoustic waves for 3D focusing of micro-particles.

However, the focusing performance of these methods largely depends on particle size. The hydrophoretic device holds such shortcoming as well. The slanted obstacles for hydrophoretic device with the channel height of 18 μm were designed, thereby generating rotational flow. 4 μm beads did not form hydrophoretic ordering. They moved back and forth in the micro-channel and occupied the whole channel in both *y* and *z* direction (**Error! Reference source not found.** a, b) [41]. On the contrary, 15 μm beads assumed hydrophoretic ordering and had their equivalent positions by the steric hindrance. Their focusing position was (y, z)=((17.2±3.1), (22.8±0.8) μm) (Figure 2-6 c). Therefore, 3D focusing was achieved in this hydrophoretic channel. Later, the hydrophoretic mechanism was also investigated with a simulation modelling. Especially for 15 μm particle, the collision occurs around the front edge of the groves, which makes it diffuse out of rotational streamline. In contrast, 4 μm particle follows its rotational stream, moving from one sidewall to the other sidewall of the channel (Figure 2-6 d, e).

The focused particles normally migrated along the sidewall of the channel in the channel with slanted obstacles, which made it difficult to detect in the microflow cytometer. The obstacles with V shape were designed to focus the particles in the centre of the channel. Also, the upper layer with obstacles was facing with the lower layer with the same obstacles (Figure 2-7 a, b, c) [4]. The blood cells were injected into the micro-channel under the applied flow rate to verify the cell focusing in the hydrophoretic channel. After passing the channel of 15.4- μm high, around 57% of blood cells had the lateral position ranging from 400 to 600 μm (Figure 2-7 d). Once the channel height was reduced to 7.2 μm, the percentage of blood cells within the position from 400 to 600 μm increased to 72% (Figure 2-7 e).

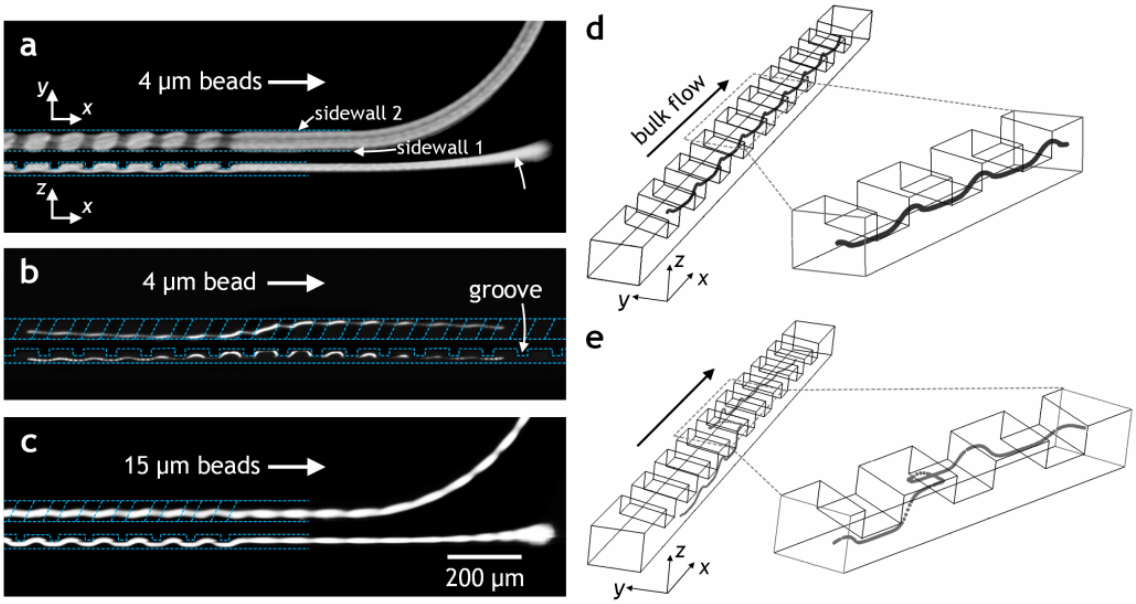

Figure 2-6 3D particle focusing in hydrophoretic device. (a) Fluorescent-field image of 4 μm beads past through the channel. (b) The trajectory of a single 4 μm bead. (c) The tracing of 15 μm beads assuming hydrophoretic ordering. Simulated particle trajectories of 15 (d) and 4 (e) μm beads [41].

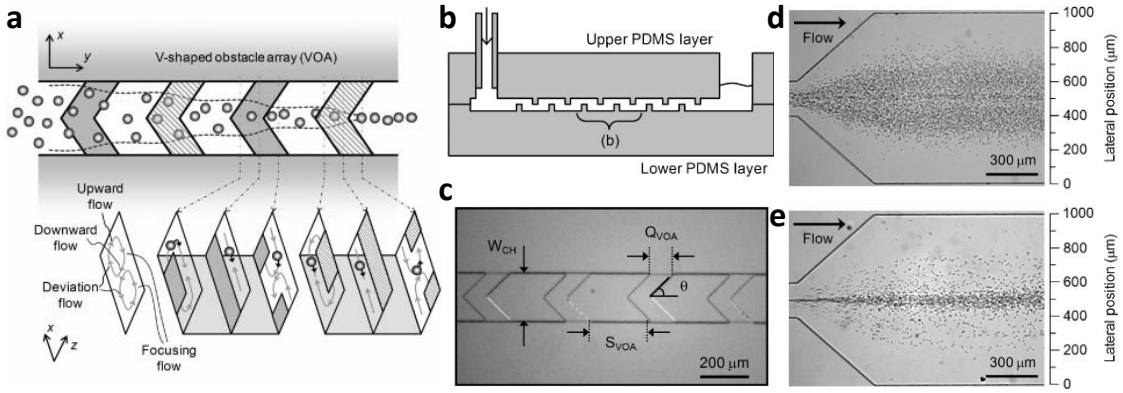

Figure 2-7 (a) Top-view of hydrophoretic device and velocity vectors in the cross sections. (b) Cross-section of the device with upper and lower obstacles. (c) Optical micrograph showing the V-shaped grooves in the focusing channel. Focusing blood cells in the microfluidic channel with channel height of (d) 15.4 and (e) 7.2 μm [4].

However, due to the size-sensitive behaviours of particles, the particle separation is still more effective than particle focusing. To overcome this issue, extended channel with V-shaped obstacles was proposed to increase the focusing efficiency (Figure 2-8 a, b) [42].

With the expansion of the channel, the ratio of the focusing width of the particles to the channel width becomes smaller, thereby the focusing efficiency increases. After several extension steps, the Jurkat cells were focused well in 1 mm-wide channels (Figure 2-8 c, d).

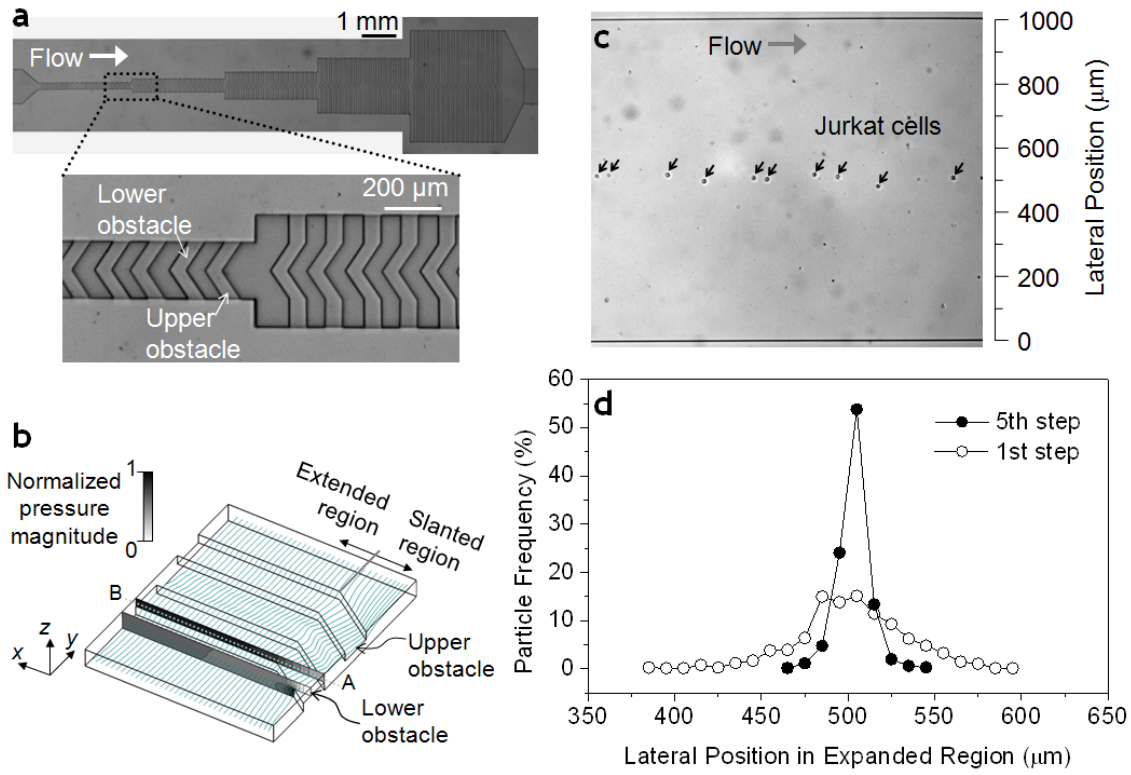

Figure 2-8 Exponential hydrophoretic device for sheathless particle focusing. (a) optical microscopy images of the hydrophoretic device with five step extensions. (b) Numerical pressure gradient and streamlines around obstacles. (c) The focusing stream of Jurkat cells at the outlet. (d) Focusing profiles of Jurkat cells [42].

2.2. Hybrid microfluidics

Based on the physical principles that govern the separation process, hybrid microfluidics is divided into four categories: (i) DEP-assisted, (ii) Magnetophoresis (MP)-assisted, (iii) Acoustophoresis (AP)-assisted, and (iv) Optophoresis (OP)-assisted techniques (Figure 2-9). Within each category the theory behind each physical field, the approaches used to tune particle motion, and advanced hybrid technologies are presented.

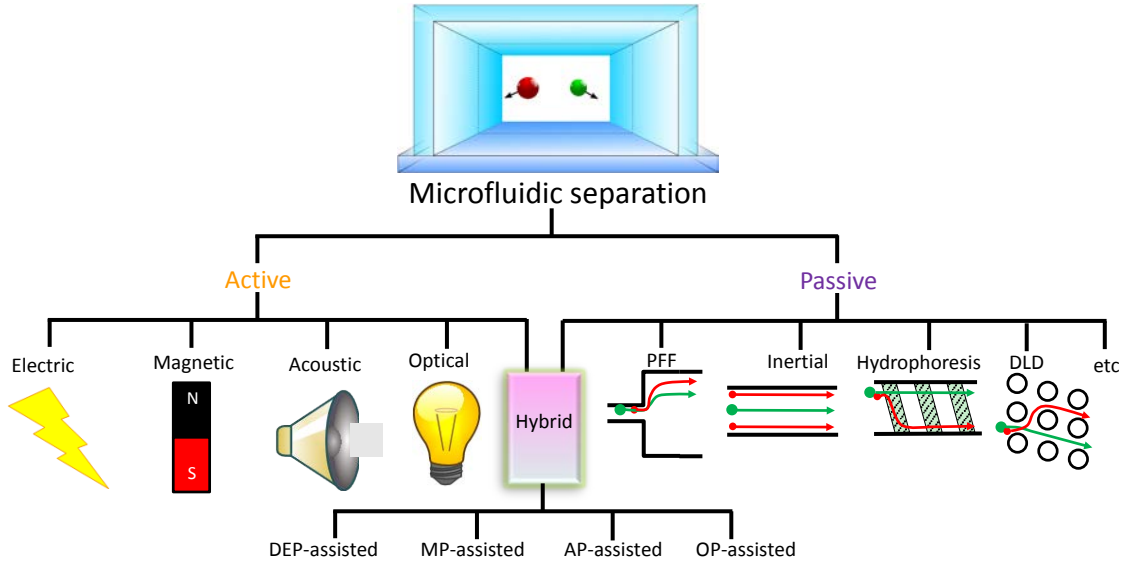

Figure 2-9 Manipulating techniques for microfluidic cellular separation. Hybrid microfluidics combines the advantages of both active and passive methods, which is classified into DEP-assisted, MP-assisted, AP-assisted and OP-assisted technique.

2.2.1. Dielectrophoresis-assisted hybrid techniques

DEP refers to the movement of polarised (neutral) cells in a non-uniform electric field where once exposed, the cells migrate towards or away from the strongest part of the electric field according to the electric permeability and conductivity of the cell and the fluid. In a non-uniform electric field, the polarisable cells suspended in an aquatic medium will experience a time average dielectrophoretic force. The net force F_{DEP} is given by [43]:

$$F_{DEP} = 2\pi\varepsilon_m r^3 \,\mathrm{Re}[K(\omega)]\nabla E_{RMS}{}^2 \qquad 2\text{-}1$$

where ε_m is the absolute permittivity of the suspending medium, r denotes the radius of the cell, $\nabla E_{\mathrm{RMS}}{}^2$ is the gradient of the square of the applied field E_{RMS}, and $K(\omega)$ refers to the Clausius-Mossotti (CM) factor. Re indicates the real part of the factor, $K(\omega)$ depends on the complex permittivities of the cell and the suspending medium, and the frequency of the external electric field, via,

$$K(\omega) = (\varepsilon^*_{cell} - \varepsilon^*_{medium})/(\varepsilon^*_{cell} + 2\varepsilon^*_{medium}) \qquad 2\text{-}2$$

where $\varepsilon^{*}=\varepsilon-i\sigma/\omega$ ($i^2=-1$) is the complex permittivity, σ is the electrical conductivity, and ω is the frequency of the electric field. Since cells have a complex structure of cytoplasm, membrane, and nuclear envelope, a spherical multi-shell model is utilised to measure the Re[$K(\omega)$] [44]. The $K(\omega)$ factor is a dominating role in DEP force that represents the dielectric properties of cells and suspending medium under different frequencies of the electric field applied. If the permittivity of a cell is greater than the suspending medium ($K(\omega)>0$), a positive DEP (p-DEP) is generated in this mode, where the cell migrates to the maxima of the electric field. However, if $K(\omega)<0$, the cell is repelled from the maxima of the electric field which is referred to as a negative DEP (n-DEP).

According to Eq. 2-1, the DEP force is proportional to the square of the applied field, which means it can be tuned by the amplitude of the external signal. To control the movement of particles, altering either the frequency of the electric field or fluid permittivity would be an alternative, although label-free DEP-based devices can separate cells based on their intrinsic characteristics including volume and dielectric properties (*i.e.*, polarisability).

DLD is a passive method proposed by Huang et al. [45] to continuously separate beads with a high resolution down to 20 nm and also separate blood cells and isolate plasma from whole blood [33]. Even though DLD can spatially manipulate cells in a deterministic manner, the new devices lack the flexibility needed when samples are varied. To bridge this gap, DLD was combined with DEP to improve separation efficiency. Chang and Cho [46] replaced the mechanical pillar array with spot electrodes which could generate a virtual DLD array with an n-DEP force generated by an AC electrical field. The range of separable particle sizes was tuned using the frequency and amplitude of the electric field. Beech et al. [31] described a method which combines DEP with DLD, thus taking advantage of the two approaches offered. Here, platinum wires inserted into the inlets and outlets of the DLD devices to serve as electrodes that generate an n-DEP force around the micro-posts. When a DEP force is applied it pushes the beads to the neighbouring lamina while shifting from ‘zigzag’ mode to ‘displacement’ mode. This means the critical size for separating micro-beads

was tuned from 6 μm to 2 μm in a single device by altering the external AC signals (Figure 2-10a).

Hydrophoresis is a newly emerging hydrodynamic approach that utilises the steric effects between particles and grooves [4]. However, the threshold for hydrophoretic cell separation depends almost entirely on the height of the channels, and that requires accurate fabrication for a specific application. Recently, our group [47] proposed a DEP-assisted hydrophoresis device with interdigitated electrodes and hydrophoretic channels, where once the particles experience the n-DEP force generated by the electrodes the will be levitated towards the top wall of the channel where the intensive particle-groove interactions allow the particles to form a hydrophoretic ordering. Although the diameter of bio-particles or cells was less than the critical diameter, they were still focused on the channel due to the DEP force. Since the lateral positions of particles can be tuned by AC signals, particles with distinct sizes were separated based on their different focusing positions in the lateral direction (Figure 2-10b) [48].

Inertial force can lead to the cells migrating across the streamlines in laminar flows. Due to its merits of high throughput, simplicity, robustness, and ease of parallelisation and fabrication, inertial microfluidics has also been investigated for bioengineering and clinical diagnosis, including but not limited to the extraction of blood plasma, [49, 50] separation of particles and cells, [51-55] solution exchange, [56-58] cell enrichment, [59] isolating circulating tumour cells (CTCs),[60-66] detecting the malaria pathogen,[67, 68] cell cycle synchronization, [69] cell encapsulation,[70] and hydrodynamic stretching of single cells.[71, 72] Unfortunately, the only parameter that can be adjusted is the Reynolds number for an inertial microfluidic platform, so most inertial microfluidic devices suffer from a relatively low recovery yield. Increasing the Reynolds number may improve the yield to some extent, but poor purity inevitably follows [73]. Moon et al. [74] proposed a device consisting of a multi-orifice flow fractionation (MOFF) channel and a dielectrophoretic channel for isolating the CTCs from blood (Figure 2-10c). The blood cells were filtrated in a massive and high-throughput manner by inertial separation in a MOFF channel, while the serially connected DEP sorter acted like a precise post-processor to further enhance the separation efficiency and purity. Apart from the hybrid device whose active and passive components worked independently, our group proposed a DEP-inertial microfluidic

platform which coupled the inertial lift force with the DEP force. [75] This hybrid technique can modify the inertial focusing patterns in a serpentine channel by a vertical n-DEP force generated by interdigitated electrodes patterned on the bottom of the microchannel. With help from the DEP force, particles were levitated along the height of the channel, and the three-dimensional focusing pattern of particles can be adjusted in real time.

Dielectrophoretic field-flow-fractionation (DEP-FFF) is another approach which integrates DEP and FFF for particle or cell separation. Cells are balanced by DEP force, sedimentation, and hydrodynamic lift forces at the equilibrium positions. Since the flow field is parabolic along the height direction, cells with a faster speed at their equilibrium positions will reach the outlet in a shorter time, and therefore cells with different density, dielectric, and mechanical properties are separated in time [76, 77]. However, DEP-FFF operates at a batch-mode, which limits its throughput. To improve this throughput, Shim *et al*.[78] developed a continuous flow-based DEP-FFF for cell separation where target cells experiencing a positive DEP were attracted to the bottom of the channel, while non-target cells are pushed to a higher position in the channel due to the negative DEP force. The target cells are isolated by skimming the non-target cells. Since the cells are separated in a vertical direction, the width of the channel had almost no effect on separation efficiency. Therefore, increasing the width of the channel can significantly improve throughput.

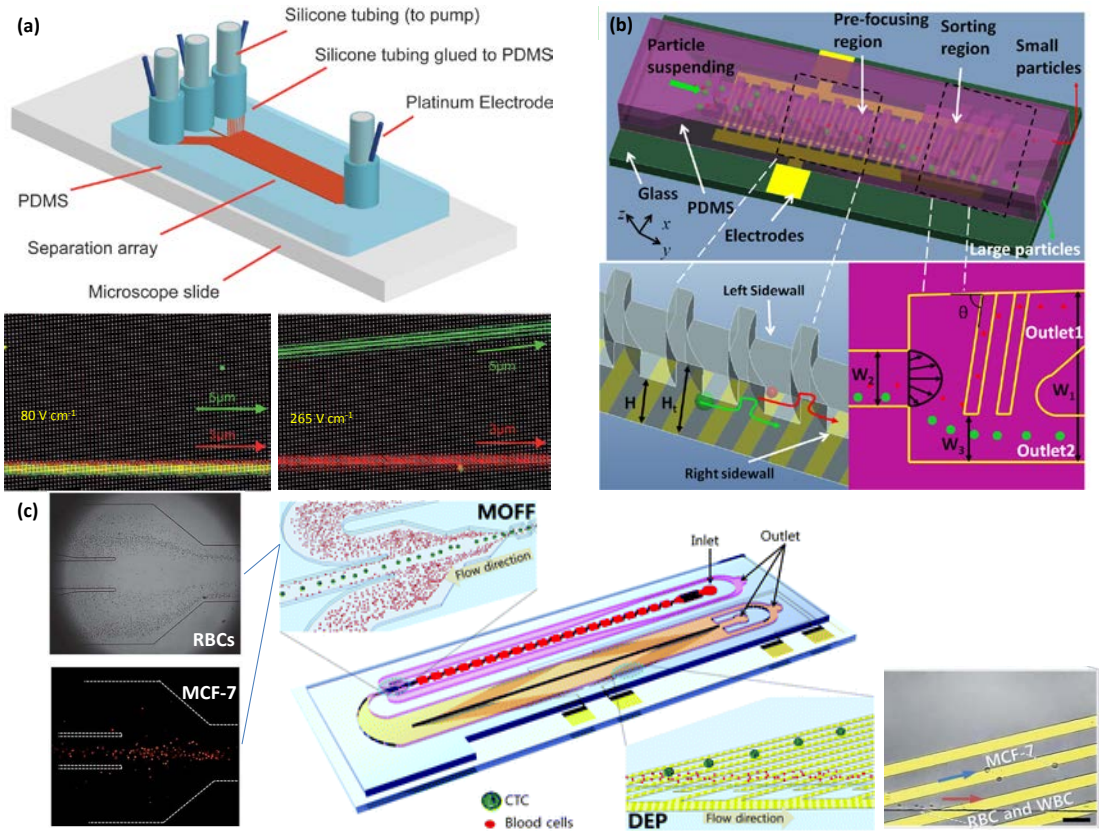

Figure 2-10 (a) Schematic diagram of DLD with DEP; at a low voltage of 80 V cm^{-1} the trajectories of the 3 μm and 5 μm particles are overlaid and there is no obvious separation, but at 265 V cm^{-1}, the critical diameter is tuned and the 5 μm beads are in displacement mode and then separated from 3 μm beads [31]. (b) The layout of the DEP-assisted hydrophoretic sorter. Both large and small particles can be focused onto the sidewall under a certain external electric field in the prefocusing region, whereas particles of different sizes are separated in the sorting region due to distinctions in the lateral positions [48]. (c) An illustration of a microfluidic device for high-throughput separation of MCF-7 from blood cells using MOFF and DEP. The relatively larger MCF-7 cells and a small portion of blood cells enter the centre of the channel, while most blood cells are filtered in the MOFF. Finally, MCF-7 cells are selectively isolated *via* DEP [74].

2.2.2. Magnetophoresis-assisted hybrid techniques

The magnetic force (F_{mag}) exerting on a particle (Eq. 2-3) relies on the difference between the magnetic susceptibility of the particle χ_p and the base fluid χ_m, as well as

the volume of the particle V_p, the magnetic flux density and gradient of the magnetic field $(B\cdot\nabla)B$, and μ_0, the permeability of free space ($4\pi\times10^{-7}$ H m^{-1}) [79]:

$$F_{mag} = \frac{(\chi_p - \chi_m)V_p}{\mu_0}(B\cdot\nabla)B \qquad 2\text{-}3$$

For a magnetic particle ($\chi_p > 0$) dispersed in an aqueous diamagnetic medium ($\chi_m < 0$), a positive magnetophoresis is produced in this mode, where the particle migrates to the maxima of a magnetic field. However, if the particle is diamagnetic ($\chi_p < 0$) and the medium is paramagnetic ($\chi_m > 0$) then the difference between the values becomes negative and the particle is pushed towards an area of field minima.

The above equation indicates that a gradient in the magnetic field and a difference in susceptibility are required to generate a magnetic force on a particle. Therefore, magnetic cell separation is achieved by differences in the magnetic forces, which mainly depend on the size, the difference in magnetic susceptibility, and the field gradient. A magnetic field is typically generated by permanent magnets or electromagnets, and with assistance from the ferromagnetic structure, the magnetic field gradient is enhanced to increase the magnetic force.[80-82] The susceptibility of a mismatch is another significant factor that affects the separation efficiency or throughput of MP-based devices. Since biological cells consist of non-magnetic particles, they can be specifically labelled with particles of high magnetic susceptibility to distinguish them from the sample mixtures. [83, 84] Alternatively, the use of ferrofluids and paramagnetic ions improves the magnetic force by modifying the susceptibility of the medium. [85, 86]

Seo *et al*. [87] proposed a hybrid cell sorter that combined hydrodynamics and MP to improve the efficiency of inertial-based separation. Their device consists of an alignment component with a paramagnetic line and an inertial-based separation component. In the presence of a magnetic field, paramagnetic particles were repelled towards the sidewalls of the channel, and diamagnetic particles were attracted into the centre of the channel, but in the separation segment, the particles were further separated and collected by their sizes. Kirby *et al*. [88] devised a centrifuge-magnetophoretic system to separate magnetic particles of different sizes, as well as magnetic and

diamagnetic particles of the same size. Mizuno *et al*. [89] introduced a simple microfluidic platform that utilised hydrodynamic filtration and MP to sort cells based on their size and magnetic properties (Figure 2-11 a). Initially, immunomagnetic bead-conjugated cells were focused onto the sidewall of the channel by the hydrodynamic effect, and then sorted into individual separation lanes based on their size difference. In the second stage, cells were driven laterally by the magnetic force and then recovered through multiple outlet branches on the basis of their magnetic characteristics.

Researchers from the Toner lab [90] recently described an inertial focusing-enhanced microfluidic CTC isolation platform that combined the advantages of passive microfluidics for rare cell manipulation while integrating the merits of magnetophoretic cell sorting. The proposed platform consists of three modules within a single device: (i) separation of nucleated cells, including WBCs and CTCs, from RBCs and platelets via DLD, (ii) positioning cells in an almost single line using inertial focusing, and (iii) deflection of magnetically tagged CTCs into a collection channel using positive MP (Figure 2-11 b).

Giudice et al. [91] described the deterministic separation of particles by combining MP and viscoelasticity. Their microfluidic device contained two processes; in the first module the magnetic and diamagnetic particles were focused by exploiting fluid viscoelasticity in a straight rectangular channel, and in the second, when the channel was exposed to a magnetic field, the magnetic beads were deflected from the original stream and then separated from the diamagnetic beads.

Our group proposed a novel micro-device that combines negative magnetophoresis and hydrophoresis for rapid particle ordering. [92] The non-magnetic particles in the diluted ferrofluid experiencing negative magnetic forces were pushed close to the grooves where particle-groove interaction enabled hydrophoretic ordering of the particles. By changing the concentration of ferrofluid and external magnetic field, the particle focusing patterns can be tuned.

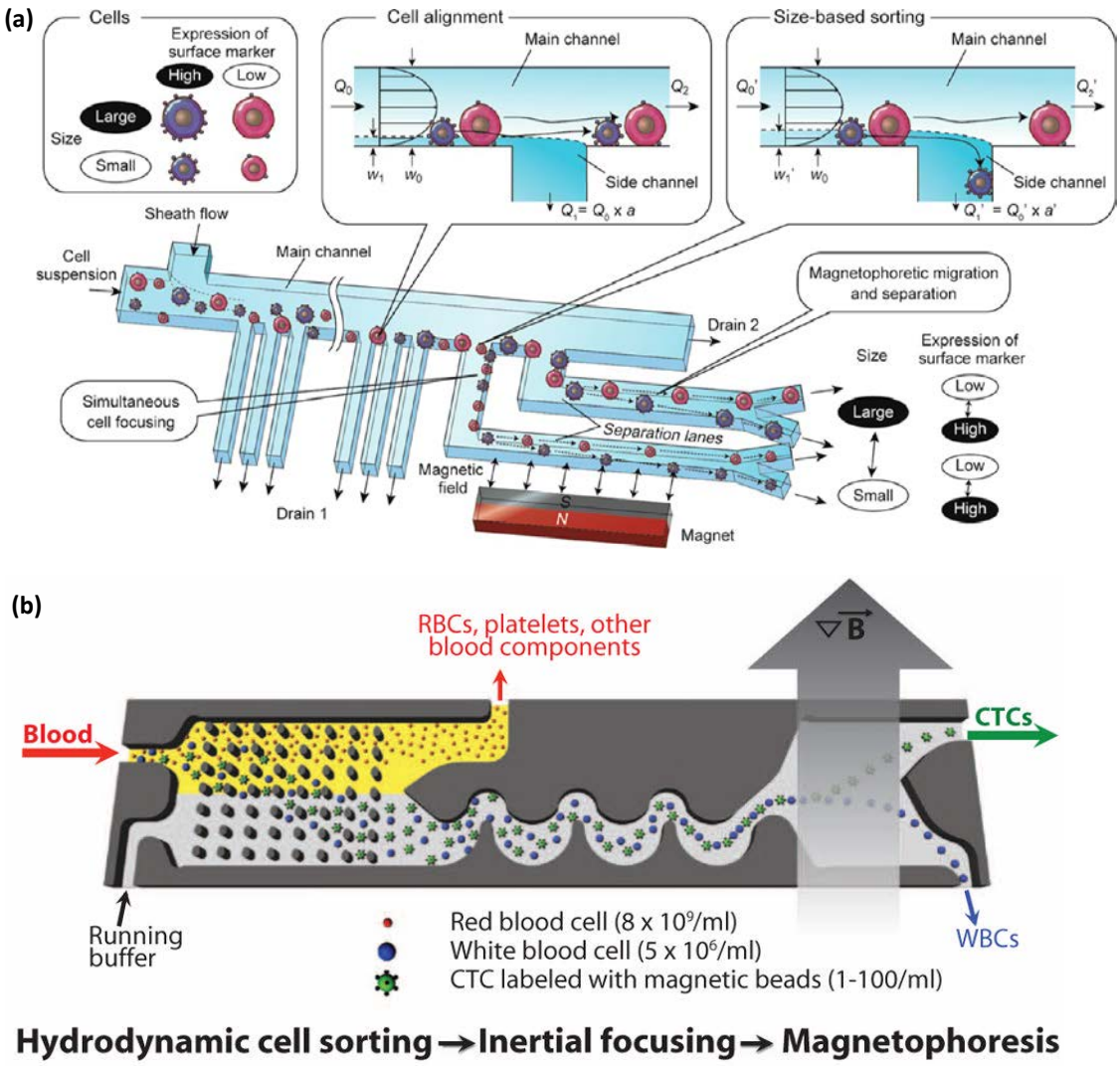

Figure 2-11 (a) A continuous-flow microfluidic channel integrating hydrodynamic filtration and MP for cell sorting. The cells are first sorted into corresponding channels based on their size. In the downstream, the cells conjugated with magnetic beads are separated under a magnetic field [89]. (b) Schematic showing a hybrid microfluidic device which integrates DLD, inertial focusing, and MP to isolate rare CTCs. In the DLD region, magnetically tagged CTCs and white blood cells are washed and separated from the blood, while red blood cells and platelets are removed from the chip. In the second part, CTCs and white blood cells are well focused *via* inertial focusing in an asymmetrical serpentine channel. Finally, CTCs are effectively separated in a magnetic field [90].

2.2.3. Acoustophoresis-assisted hybrid techniques

Acoustic streaming is generated when a microfluidic channel is excited by ultrasound to a resonance mode. Here a suspended particle with a radius *r*, will experience a one-dimensional primary acoustic radiation force which is described by the following equation [93]:

$$F_a = 4\pi r^3 E_{ac} k \sin(2kz)\phi \qquad 2\text{-}4$$

where E_{ac} represents the acoustic energy density, z denotes the distance from the pressure antinode in the wave propagation axis, k is the wavenumber ($2\pi f/c_0$), where f is the frequency of the wave, and c_0 is the speed of sound in the medium, and ϕ is the acoustic contrast factor defined as:

$$\phi = \frac{\rho_p + \frac{2}{3}(\rho_p - \rho_0)}{2\rho_p + \rho_0} - \frac{\rho_0 - c_0^2}{3\rho_0 c_p^2} \qquad 2\text{-}5$$

where c_p is the speed of sound in particle material and ρ_p and ρ_0 is the density of the particle and the medium, respectively. The direction of the acoustic radiation force depends on the sign of the acoustic contrast factor ϕ. If $\phi > 0$, cells will migrate towards the node of an acoustic standing wave, whereas a negative contrast factor means the cells move to an antinode. Typically, as the density of cells is slightly higher than the physiological buffers, most cells show a positive contrast factor under an acoustic field [94].

From Eq. 2-4, the acoustic radiation force is proportional to the cube of the cell radius, so large cells will experience larger forces than small ones. Moreover, cell size is not the only property that can be used for acoustophoretic sorting; cells with a different density ρ_p or speed of sound c_p, can be separated continuously according to Eq. 2-5. Alternatively, cells in a mixture with different contrast factors can be sorted, that is, cells with a positive contrasting factor are driven to the centre of the channel (pressure node) and cells with a negative contrasting factor migrate towards the sidewalls of the channel (pressure antinode) in a half-wavelength resonator.

Collins et al. [95] presented a virtual DLD to sort tunable particles by a combination of acoustophoresis where the virtual DLD system integrated with interdigital transducers (IDTs) which produced acoustic radiation forces at an angle to the direction of flow. Principally, the radiation force on a particle whose diameter is above the critical diameter overcame the drag force and drove particles laterally along the angle of IDTs. Smaller particles were not influenced enough by the force field and thus maintained the original direction of fluid flow without any disturbance. Tunability was enabled by modifying the applied voltages, from which >97% separation of 5.0 μm and 6.6 μm particles and ~87% separation of 300nm from 500nm particles were achieved.

2.2.4. Optophoresis-assisted hybrid techniques

As well as forces from an electric field, magnetic field, and acoustic field, optical forces generated by a highly focused optical beam of light have been rapidly developed for particle sorting over the past decades. [96] Optical methods are considered promising due to the preservation of cell function, precise spatial control in three dimensions, and of the ability to manipulate small targets such as cells and molecules [97]. Typically, a focused laser beam has a Gaussian intensity profile and can manipulate cells using a mismatch in the refractive index between the cells and the medium to produce optical scattering and gradient forces. While scattering forces tend to push cells away from the centre of the beam, gradient forces attract cells towards the beam maxima. Similar to pDEP, objects with a high refractive index travel to the point of highest intensity and are optically trapped; this became known as “optical tweezers” [98]. Moreover, the laser wavelength, power, and trap geometry can be adjusted to sort objects ranging from 100 nm to 100 μm [99].

Optical forces can be used to sort particles in active and passive ways. [100] Cells may be sorted actively by activating lasers when a rare event occurs to push the cell of interest out of the original trajectory into a sorted fraction. [101] Passive sorting has been proposed by MacDonald *et al*. [102]. They used an extended, interlinked, dynamically reconfigurable, three-dimensional optical lattice, similar to DLD, to sort protein microcapsules by size and colloidal particles by the refractive index. When a mixture passes through the lattice, the target particles are deflected from their original positions, while others remain at the same position (Figure 2-12 a). The efficiency of

this method of separation depends largely on how particles respond to their optical potential, because unlike the physical micro-posts in DLD which could suffer from clogging, the virtual posts generated by the optical lattice led to a 45º angular deflection.

Pinched flow fractionation (PFF), reported by Yamada *et al*. [103] was a simple and passive technique for continuously separating particles in a microchannel by utilising the spreading flow. Due to its simple structure, the PFF are easily integrated with other active techniques. To modify the PFF, optically enhanced pinched flow fractionation (OEPFF) has been developed by Lee *et al.* [104], whereby after pinching the particles to one side of the channel by the sheath flow, they then travelled through the channel after being exposed to the laser beam. This optical force moved the particles laterally in the channel, as shown in Figure 2-12 b, and since this lateral displacement is associated with particle volume and laser parameters, the equilibrium positions of different particles at the pinched region will be enhanced. Following this spreading flow at the broadened region, the particles became separated by larger distances but then recovered with greater efficiency. This method could also separate two kinds of leukaemia cells [105].

Apart from an optical tweezer, an optoelectronic tweezer is another technique that requires a photoconductive substrate and a programmable display device that can project the images onto a photoconductive surface to form transient electrodes which can precisely manipulate micro- and nano-particles. [106] Optoelectronic tweezers thus provide a low power approach for cell capture, transportation, and separation without labels; moreover, they not only provide high-resolution manipulation of single particles but also require 100,000 times less optical intensity than optical tweezers [107]. Even though optoelectronic tweezers are simple, flexible, and programmable, integration with other passive components can enable high throughput and complicated processes. [108] Since optoelectrofluidic platforms do not need extra fluidic components such as tubing and pumps, they are difficult to couple with other passive techniques for complex sample processing such as the injection of multiple flows, change of medium buffer, and continuous sample processing. To the best of our knowledge, no publication has reported on the hybrid scheme based on an optoelectronic tweezer.

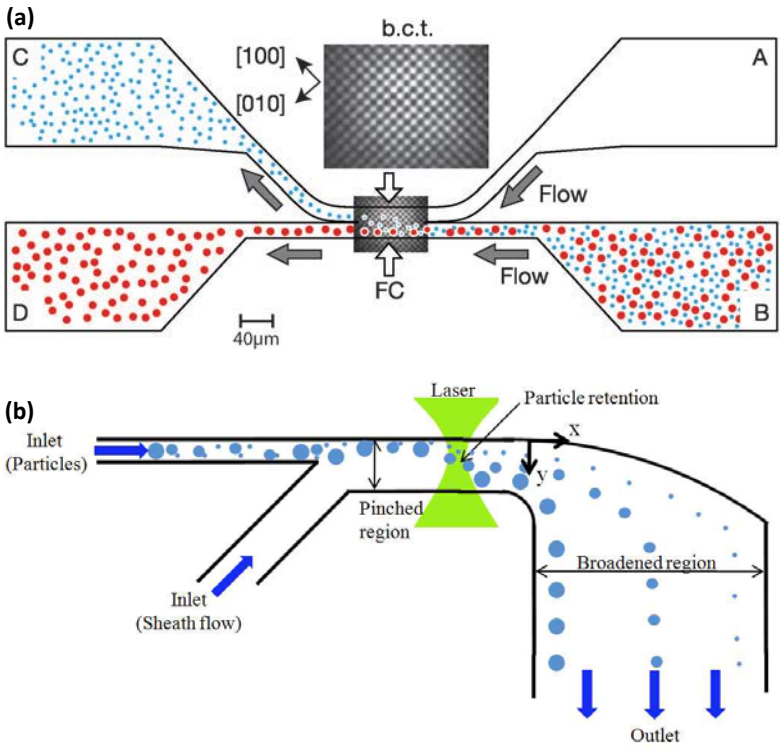

Figure 2-12 (a) Microfluidic sorting in an optical lattice. The virtual DLD is generated by an interlinked, dynamically reconfigurable optical lattice for optical fractionation [102]. (b) Schematic diagram of a microfluidic device based on optically enhanced PFF. In the pinched region, the equilibrium positions of different particles are modulated by an optical scattering force. The differences in particle positions are further amplified in the broadened region along the streamlines [104].

2.2.5. Applications in cell separation based on hybrid microfluidics

The fundamentals of hybrid microfluidics and the various examples used to achieve tunable and continuous cell/particle separation are described above; this section presents applications of hybrid microfluidics in cell sorting to highlight its enormous potential for biological studies.

Blood

Mammalian blood consists of white blood cells, red blood cells, platelets and plasma. [33] White blood cells play a significant role in the immune system, while platelets are responsible for formatting blood clots. [35] Red blood cells are the most common,

accounting for 98% of all blood cells,[34] whilst the remainder consists of plasma, a straw coloured aqueous medium. Sorting or removing cells from blood has been found to be very beneficial for diagnostic purposes such as malaria [109], HIV [110], stroke [111], etc.

A cell separator using an n-DEP virtual pillar array was used to separate red blood cells (5.4 ± 1.3 μm-diameter) from white blood cells (8.1 ± 1.5 μm-diameter) [46]. Despite their large differences in size, red blood cells and white blood cells were successfully separated with a purity of more than 99%, at a voltage of 500 kHz, and with a 10 V_{rms} sinusoidal wave and a flow rate of 0.11 μl min^{-1}.

Our group [112] devised a DEP-assisted hydrophoretic device to separate plasma from whole blood; plasma being the liquid composition of blood that may contain proteins and circulating nucleic acids and viruses that can be used for clinical diagnostics. In our work the large cells (red blood cells and white blood cells) and small cells (platelets) were focused simultaneously at an appropriate flow rate of 10 μl min^{-1} and a voltage of 1MHz, 20 V_{p-p} AC signal, which enabled all the blood cells to separate from the blood and plasma to be extracted with high purity (~94.2%).

Seo *et al*. [87] presented a hybrid method to separate red and white blood cells using MP and inertial microfluidics. The efficiency of separating red blood cells at the main outlet increased from 75.2 to 86.8% when a magnetic field was applied, whilst the classification efficiency of WBCs dropped from 83.8 to 70.9% with the hybrid scheme.

Circulating tumour cells

Cancer metastasis is responsible for approximately 90% of cancer-related deaths caused by CTCs. [113] CTCs and malignant cells originate from primary or second tumour sites and enter the peripheral blood, [114] but because extracting blood from cancer patients is clinically less invasive, CTCs potentially act like a liquid spy for prognosis, evaluation of treatment efficacy, and studying molecular alterations under therapy. [115, 116]

Microfluidic CTC isolation techniques can be classified as either positive or negative method [117] where positive methods typically capture the CTCs and elute

haematological cells using the expression of cell surface antigens. Glynn *et al.* [118] proposed a centrifuge-magnetophoretic system for isolating HL60 cells from whole blood. The cells expressing the HIV/AIDS relevant epitode (CD4) were bound with superparamagnetic microparticles, so all the cells were loaded into a chamber under rotation and bead-conjugated target cells were deflected to a designated reservoir under a magnetic field, and almost 92% of CTCs were separated from the whole blood. Ozkumur *et al*. [90] proposed an innovative CTC-iChip to separate magnetically tagged CTCs from peripheral blood for clinical diagnosis. It should be mentioned that the novel chip could capture CTCs using strategies that are either dependent on or independent of tumour surface makers, and therefore applicable for a wide range of cancers. This chip also benefitted from inertial focusing because it could also isolate CTCs from whole blood in a high-throughput manner (~10^7 cell s^{-1}). In this work, 98.6% of SKBR3 human breast cancer cells were recovered from the whole blood and almost 89.7% of human prostate PC3-9 cancer cells were also captured.

Unlike the positive isolation of tumour cells, negative enrichment is the preferred approach because it does not rely on the biomarker expression on the tumour cells and can keep the cells intact. Moon *et al*. [74] successfully separated human breast cancer cells (MCF-7) from a sample of spiked blood by combining MOFF and DEP techniques. The MOFF component consisted of an alternating series of contraction channels and expansion chambers. Once the blood samples were injected through the inlet, most of the blood cells were focused on the sides of the channel and then extracted through outlet I, while the MCF-7 cells with unseparated blood cells headed toward the DEP separator. The DEP separator commenced with an expansion channel where the flow velocity decreased dramatically (×1/200) to better fit the DEP separation. At the first set of DEP electrodes, all the cells were driven to the sidewalls due to the absence of sheath flow, the MCF-7 cells migrated to the centre of the channel after passing through the second slanted electrodes, while blood cells remained at the same position, while the cancer cells exited through outlet II and the residual blood cells exited through outlet III (Figure 2-10 c). Up to 162-fold enrichment of the MCF-7 cells was achieved and red and white blood cells were removed with separation efficiencies of 99.24% and 94.23%, respectively.

Lau *et al*. [105] devised an integrated optofluidic platform that combines the laser tweezers Roman spectroscopy and PFF for separating leukaemia cells. Here the targeted leukaemia cells were trapped by the laser tweezer and then moved to a neighbouring side channel, and then the cells of interest were sorted from the cell mixture. Sajay *et al*. [119] developed a microfluidic system for negatively isolating CTCs using magnetophoresis and membranes. In the first step, the CD45-positive WBCs were magnetically immune depleted from the whole blood, and step two consisted of a microfabricated filter membrane implemented RBC depletion and target cell isolation. The RBCs and platelets freely passed through the micro slit membrane, whereas the CTCs could not, which meant that 90% CTCs were recovered from the blood sample. Another negative isolation of CTCs is based on the dielectric signature. [78] This technique combines DEP and FFF for separating tumour cells with high throughput (~10 ml h^{-1}). The tumour cells and peripheral blood mononuclear cells (PBMCs) with different dielectric properties were brought to different heights due to a balance between the DEP force, sedimentation, and hydrodynamic lift force, and eventually collected from different outlets. Various CTC types spiked into PBMCs were recovered at an average rate of ~75%.

Other cell types

Hybrid microfluidics is used to sort and isolate a variety of cells, but due to differences in membrane potentials under a non-uniform electric field, viable and non-viable cells were separated using a modified DEP-assisted hydrophoretic device [48] integrated with the focusing and sorting parts, where cells were concentrated in the focusing section and then separated in the sorting region. Based on the distinct dielectric property of viable and non-viable Chinese Hamster Ovary cells at a medium conductivity of 0.03 S m^{-1}, the live cells exerting a larger DEP force focused well and were then separated from the sample cell with a purity of 99.6%. Another approach is to tag target cells with magnetic beads so they can be manipulated with a magnetic field. A magnetophoresis-integrated hydrodynamic filtration system for cell sorting has been reported by Mizuno *et al*. [89]. The JM (human lymphocyte cell line) cells conjugated with anti-CD 4 immunomagnetic beads and unlabelled HeLa cells were separated at a purification ratio higher than 90%.

2.2.6. Challenges and perspectives

This review highlights the recent development of continuous cell sorting in hybrid microfluidic devices. Since making its appearance, hybrid microfluidics has attracted a substantial amount of press and interest, but there are big challenges that must be addressed to make it more practical. Firstly, commercialising hybrid technologies into industry and hospitals will keep this field attractive and dynamic, but most of the microfluidic technologies reviewed here are still in the prototype or proof-of-concept stage; only a few have the capability for clinical usage. Commercial investment from industrial companies or medical centres is one way to satisfy their needs, but in the interim, researchers should fight to determine what can be done for biomedicine using hybrid techniques.

Secondly, while the marriage of active and passive methods combines their strengths, it also includes their weaknesses because positive MP requires pre-incubation to conjugate the cells with magnetic particles, which is time-consuming, whereas negative MP is a label-free method for manipulating diamagnetic cells. Here, the magnetic gradient in the medium can form easily by controlling the concentration of paramagnetic nano-particles or ions such as ferrofluid [120] or paramagnetic salt [82]. However, the biocompatibility of the paramagnetic medium is a huge challenge because while *E.coli* and yeast cells are sorted using a commercial ferrofluid with a continuous-flow fashion, [120] few have demonstrated the capability of processing mammalian cells. Shen *et al*. [82] successfully achieved a label-free separation of U937 cells from RBCs using a paramagnetic salt called Gd-DTPA, but higher concentrations of Gd-DTPA might cause cell apoptosis due to the effect of osmotic pressure. Zhao *et al*. [121] provided a custom-made ferrofluid for label-free and continuous-flow separation of HeLa cells and blood cells, but further work is needed to develop a biocompatible paramagnetic solution for mammalian cells otherwise MP will be pushed to its limit and become unattractive. The appropriate paramagnetic solution should have such feature: (i) The PH value must be maintained around 7, which is the best situation for cell culture, and (ii) The salt concentration, toxicity, and surfactant should cater for the physiological conditions to avoid cell death.

Like the drawbacks existing in MP, a DEP buffer will have a similar issue because DEP-based devices do not work very well with physiological media (conductivities >1 S m^{-1}), where cells become less polarizable than the medium, [122, 123] which is why they usually operate in a low conductive medium. Here, the sucrose solution typically acts as the base of a DEP buffer whose conductivity is adjusted by adding phosphate buffered saline (PBS) to achieve a better separation performance. [124] However, it is difficult to balance the osmotic pressure of a solution which is suitable for cell viability with its conductivity, and therefore an alternative biocompatible DEP buffer should be chosen to meet the requirements of cell polarisation and viability.

In contrast, AP and OP have non-special requirements on the cell medium where typically, cell samples are prepared in a physiological media such as PBS, where cells remain viable due to isosmotic pressure and the cells sorted in PBS can be used for cell fixation, enumeration, and staining. [125] Moreover, the viable cells being processed by AP or OP are valuable for further cell culture [126] and drug screening, [127, 128] but unfortunately AP-assisted and OP-assisted microfluidics is still a blank field that needs further exploitation.

The active and passive components in hybrid microfluidics currently operate in series with independent physics; [74, 90] or in parallel with coupled physics. [31, 47] The main concern is the incompatible throughput between each field of physics. While passive microfluidics can only work at high speed, like inertial microfluidics, the flow rate in active microfluidics is relatively low. The hybrid technique with independent physics has simpler mechanism because each section has a weak connection, but the interface between sections, such as the flow rate or pressure should be balanced carefully, otherwise the downstream section cannot work properly. In contrast, coupled physics is more complicated but versatile for cell manipulation; for instance, hydrodynamic filtration, hydrophoresis and DLD are easy to couple with the active forces because their throughputs are comparable to their active peers and therefore more combinations are possible in this format.

As a newly developed technology, hybrid microfluidics has shown enormous potential at cell separation, but there is still a vast territory urgently waiting to be explored. The practical applications of hybrid microfluidics should be demonstrated further because

this will attract more researchers to this field and more industrial partners to invest in this technology. We believe that hybrid microfluidics remains at the forefront of the next generation of microfluidic devices because it has the capacity to accurately separate complex samples and provide real-time feedback.

3. On-chip high-throughput manipulation of particles in a dielectrophoresis-active hydrophoretic focuser*

3.1. Introduction

Over the past few decades microfluidic platforms have made significant progress due to their reduced consumption of reagents, fast assay preparation, portability, and ease of integration with multiple sample processing [129]. Manipulating particles in microfluidic devices has a variety of applications, such as trapping, focusing, and sorting cells and micro-particles. One application of focusing particles into a narrow stream to enhance the performance of flow cytometry which is then utilised for counting, detecting, and sorting micro-beads [4] has already been developed; this application can be categorised into the active and passive manipulation of particles. Active manipulation utilises external energy such as acoustophoresis [6], magnetophoresis [7] and dielectrophoresis (DEP) [8-19], whereas passive manipulation includes hydrodynamic [20-23], inertial [24], and hydrophoretic [25-29] methodologies that can be used to dominate the trajectory of particles. In general, active techniques are precise methods to control the target particles. DEP has made significant progress over the last decade due to its label-free nature. Dielectrophoretic particle focusing is primarily based on the non-uniform AC electric field induced by microelectrodes inside the channels [9-12] where the particles are pumped by a pressurised flow and then focused to a tight stream by balancing forces [130]. Despite its advantages, increasing the throughput of DEP-based devices when focusing particles remains an ongoing research problem. Some researchers have made progress in improving the flow rate of DEP-based devices. Markx et al [131] used AC DEP to separate viable and non-viable yeast cells at a flow rate of 500 μL min^{-1}. Huang et al [132] introduced DEP forces for field-flow fractionation, and high flow rate of 160 μL min^{-1} was achieved in a 200-μm high by 17-mm wide micro-channel. Park et al. [129] proposed a novel microfluidic platform that combined a separation channel and a concentration channel into a single

* Results of this chapter are published in: Sheng Yan, Jun Zhang, Ming Li, Gursel Alici, Haiping Du, Ronald Sluyter, Weihua Li, On-chip high-throughput manipulation of particles in a dielectrophoresis-active hydrophoretic focuser. ***Scientific Reports***, 4, 5060, 2014.

device. E.coli was focused and separated from human cerebrospinal fluid. 94.3% of E.coli was separated and the flow rates of sheath flow and sample stream were set at 5 μL min^{-1} and 0.5 μL min^{-1}, respectively. Cheng et al. [133] reported a high-throughput continuous particle sorter utilising a 3D travelling-wave DEP. Red blood cells were effectively focused and separated from heterogeneous samples that were filled with debris, with a maximum flow rate of 10 μL min^{-1}. Although direct current (DC) DEP can focus particles [19], high voltages are needed to generate enough DEP force, which may then generate Joule heating and lead to the formation of bubbles. Additionally, DC DEP is a non-pumping method for particle focusing where the particles are driven by electro-osmotic flow [134] and migrate at a relatively low speed. Hydrodynamic focusing based on a passive method is still simple and effective, although focusing depends mainly on the accuracy of flow control, because any unstable pumping will lead to an imperfect confinement of particles and deflect them from their initial positions. Huang et al. [45] proposed a deterministic lateral displacement (DLD) to continuously separate beads with high resolution which demonstrated, successfully separated blood cells and isolated plasma from whole blood [33]. DLD can be combined with DEP to improve the separation efficiency. Beech et al [31] utilised DEP force and steric force to move particles having a diameter close to the critical diameter in the displacement mode. But fabricating an array of posts in a micro-channel may prove to be challenging. A novel approach to focus particles based on hydrophoresis has recently been reported [27].

Hydrophoresis is a sheathless and passive method that utilises a pressure gradient induced by the microstructure and steric effect between the particles and grooves [29]. The concept of hydrophoresis has demonstrated its capability by separating micro-particles and isolating white blood cells (WBCs) from RBCs [27, 36]. This new technique has a promising future in manipulating particles in a micro-channel because of the ease of parallelisation. A hybrid method of cell rolling and hydrophoresis has been proposed by using a parallelised device consisting of 20 channels [135]. Hydrophoretic ordering has been studied experimentally because the particles can be ordered and focussed by hydrophoresis and therefore its diameter should normally be larger than half the height of the channel [26]. However, it does have some limitations because the particles being processed in the hydrophoretic experiment were around 10

μm in diameter, which means the height of the channel was usually less than 20 μm, and the channels were 50 μm wide, which made it difficult to achieve high throughput. As for DNA separation [26], the cost of fabricating a 1.2 μm high channel is very high because of the accurate resolution and high precision needed for photolithography. Meanwhile, narrow channels may lead to higher flow resistance, which means that more energy will be consumed by the syringe pump, and the channels can easily be blocked by dust from the air. Even though hydrophoretic filtration has a high resolution where 11 μm and 12 μm particles can be separated in a micro-channel with slanted obstacles and filtration obstacles [36], hydrophoretic devices still lack flexibility. Once a channel is fabricated, its height is fixed at a certain value so the size of particles which can be focused and separated is determined in advance by the height of the channel.

In this paper we first propose the concept of "DEP-assisted hydrophoretic focusing" which is a combination of DEP and hydrophoresis. The critical limitation of DEP operating at a low flow rate and the specific hydrophoretic device for focusing particles with a given size are overcome in our microfluidic device. Here the particle is levitated by negative AC-DEP and its equilibrium position in a micro-channel relies on the magnitude of the electric field. The stronger the electric field is, the higher the equilibrium position the particles have. This means that interaction between the particle and groove becomes intensive and steric hindrance occurs even though hydrophoretic ordering has not been satisfied and the diameter of the particle is less than half the height of the channel (Figure 3-1 a). Whether the particles can be focused or not is determined by the external electric field. A particle with a diameter that is less than half the height of the channel can still be focused in our channel without redesigning and fabricating a new channel. In this study the anisotropic flow resistance is induced by crescent-shaped grooves to focus the micro-particles and murine erythroleukemia (MEL) cells into sidewalls of the crescent-shaped micro-channel (CSM). Compared to traditional hydrophoretic devices, CSM has a larger cross section which makes it easy to achieve high throughput. The effects of applied voltage, flow rate, and particle diameter on DEP-assisted hydrophoretic focusing were investigated and DEP-assisted hydrophoretic focusing of MEL cells in a CSM has been demonstrated.

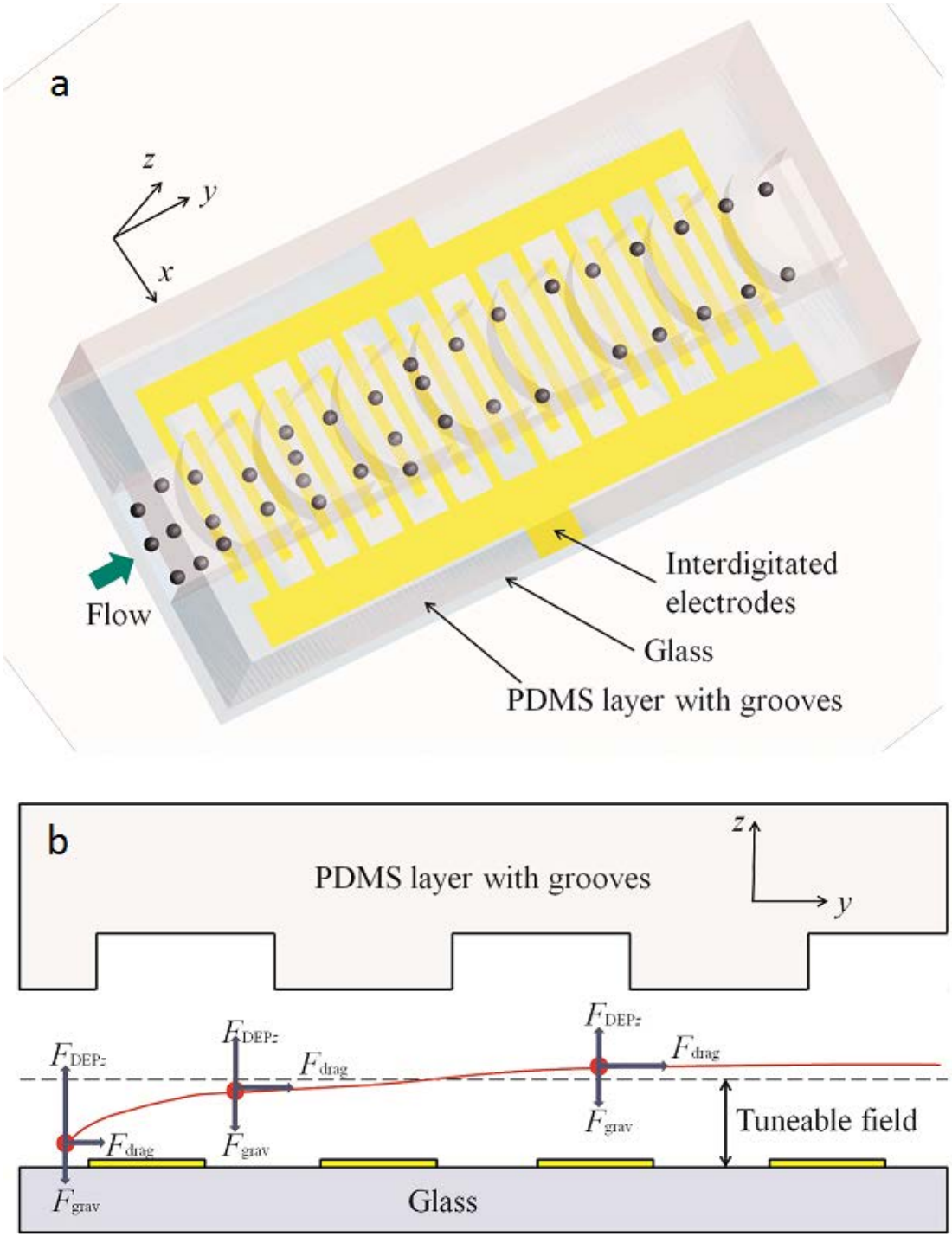

Figure 3-1 DEP-assisted hydrophoretic focusing. (a) Overview of device showing the crescent-shaped channel on top of the interdigitated electrodes. Particles, levitated by negative DEP force in z-direction, will interact with grooves along which a pressure gradient is induced by the anisotropy of flow resistance and reach each side of channel. (b) Schematics of the particle trajectory in cross-section along y-direction. A giving particle has tunable equilibrium height under different electric field.

3.2. Methods

3.2.1. Design and fabrication of microfluidic device

Details of the fabrication were reported in our previous work [136, 137]. Briefly, an electrode layer of 50 nm Ti/ 150 nm Pt was then patterned with a standard lift-off process. The spacing and width of the interdigitated electrodes were both 20 μm. The SU-8 master mould patterned on a silicon wafer, was fabricated by two-step photolithography. The channel consisted of 60 units of identical crescent-shaped grooves, each of which had a small and large curvature of 125 μm (R_1) and 175 μm (R_2), respectively. The width of the channel W was 250 μm, the height was H=45 μm, the height of the grooves was H_g=45 μm, and the pitch between the grooves was S=175 μm.

3.2.2. Preparation of polystyrene microspheres

Fluorescent micro-particles were purchased from Thermo Fisher Scientific., USA. Particles of 8 μm (Product No. 36-3, CV18%), 10 μm (Product No. G1000, CV5%), and 13 μm (Product No. 36-4, CV16%) in diameter were used in our experiments. The final concentration was about 10^6 beads per millilitre after diluting them with deionized water.

MEL cells were kindly supplied by Dr. Sally A. Eaton (University of Sydney, Sydney, Australia). The cell lines were maintained in complete culture medium (RPMI-1640 medium containing 10% fetal serum and 5mM L-glutamine) at 37°C and 95% air/5% CO_2. MEL cells were marked using PKH26 red fluorescent cell linker kit (SIGMA-ALDRICH, Product No. P9691). The detailed procedure refers to technical guidelines provided by SIGMA-ALDRICH.

3.2.3. Experimental setup

The AC electric field was generated by a function generator (33250A, Agilent, USA). The copper wires soldered onto the platinum pads were connected to the function generator to activate the electrodes. Prepared particle suspension was pumped into the channel with a syringe pump (Legato 100, Kd Scientific). The movement of particles through the CSM was monitored by an inverted microscope (CKX41, Olympus, Japan)

and captured by a CCD camera (Rolera Bolt, Q-imaging, Australia). The images were post-processed by the software Q-Capture Pro 7 (Q-imaging, Australia), and images of particle tracing were acquired by overlaying the consecutive images. The fluorescent profiles were taken from the outlet to measure the focusing performance of this device. The focusing width was defined as the distance between two points where the intensity value occupied half of the threshold. The focusing position was measured from the middle of these two points. As for DEP-assisted hydrophoretic focusing of MEL cells, cells flowing through the CSM were recorded in consecutive images (400 frames; 7 frames per second). The cells passing through different positions in the channel were counted manually. Focusing experiments were repeated three times. Electrodes were excited with a 1-MHz sine wave for microspheres and with a 10-MHz sine wave for MEL cells.

3.2.4. Numerical simulation

COMSOL Multi-physics 4.3 (COMSOL, Burlington, MA) finite element software was used to calculate the flow field and electric field in CSM. A laminar steady incompressible flow model was used because the maximum Reynolds number in the experiments was about 30, which is much less than 2300 that is normally considered as the transition number from laminar to turbulent flow [138]. An electric current module was applied to calculate the distribution of electric field in the channel, which will create the DEP force on particles. Another module, particle tracing for fluid flow, can couple laminar flow module and electric field together to simulate particle trajectory in the micro-channel.

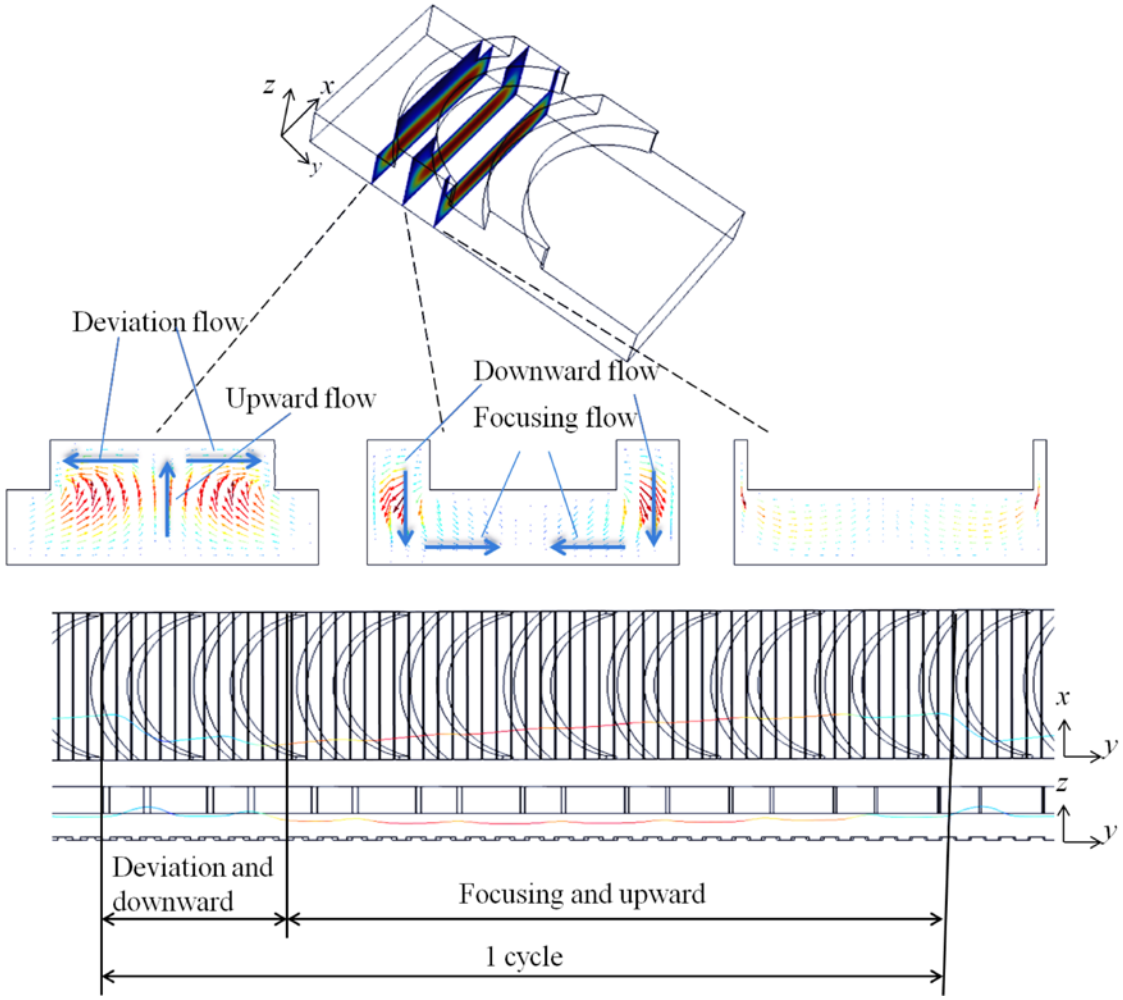

Figure 3-2 Dean flow. (a) The schematic diagrams of the CSM and the simulated results of flow field in the cross-sections. The flow direction is along the y-axis. The anisotropic microstructure induces helical recirculation, including an upwards, deviation, downwards, and focusing flow. (b) Particle trajectory in top view and side view. The particles follow the flow field and experience four stages in each cycle: deviation, downward, focusing, and upward. Blue represents low particle velocity, while red refers to high particle velocity.

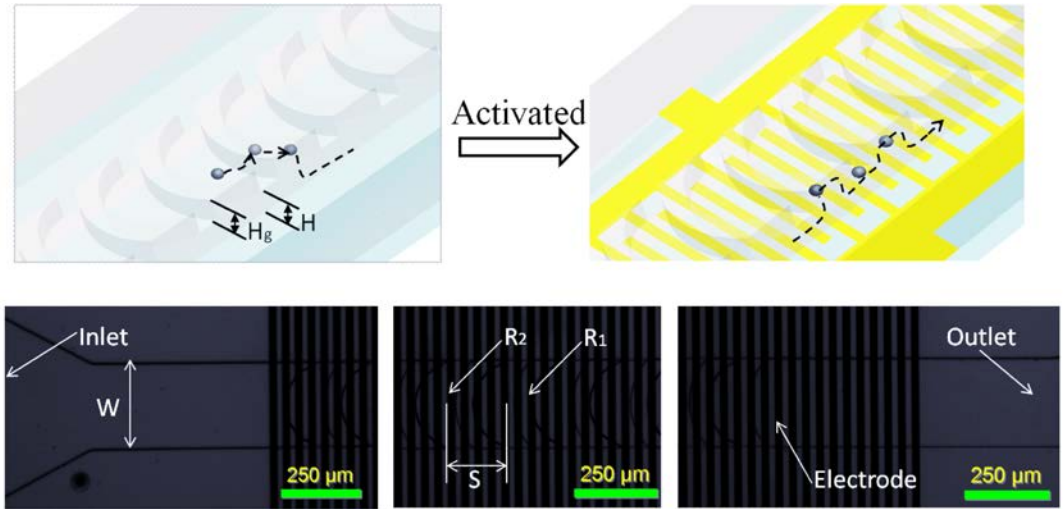

Figure 3-3 Microfluidic device for DEP-assisted hydrophoretic particle focusing. (a) Particles not obeying the hydrophoretic ordering migrate back and forth in the channel (Left), while they can be focused to the sidewalls of channel in the presence of an external electric field at the same conditions(Right). (b) Optical micrographs of the crescent-shaped grooves in the focusing channel with specific geometric parameters of R_1=125 μm, R_2=175 μm, W=250 μm, H=45 μm, H_g=45 μm, and S=175 μm. The crescent-shaped grooves were formed on the top of the channel.

3.3. Results

3.3.1. The motion of particles in a DEP-assisted hydrophoretic device

In a non-uniform electric field, the polarisable particles suspended in an aquatic medium will experience a dieletrophoretic force. The electric field at the surface of the particle is treated to be the same with the original field at the particle center.The net force F_{DEP}, are given by [43]:

$$F_{\mathrm{DEP}} = 2\pi\varepsilon_m r^3 R[K(\omega)]\nabla E_{\mathrm{RMS}}{}^2 \qquad 3\text{-}1$$

where ε_m is the absolute permittivity of the suspending medium, and r donates the particle radius, $\nabla E_{\mathrm{RMS}}{}^2$ is the gradient of the square of the applied field E_{RMS}, Re indicates the real part. $K(\omega)$ refers to the Clausius-Mossotti (CM) factor which depends on the complex permittivities of the particle and the suspending medium, and the frequency of the external electric field as well:

$$K(\omega) = \frac{\varepsilon_p^* - \varepsilon_m^*}{\varepsilon_p^* + 2\varepsilon_m^*} \qquad 3\text{-}2$$

where $\varepsilon^* = \varepsilon - i\sigma/\omega$ ($i = \sqrt{-1}$) is the complex permittivities, σ is the electrical conductivity, and ω is the frequency of the electric field. The subscripts (*p*,*m*) represents the particle and suspending medium, respectively. The $K(\omega)$ factor, a dominating role in DEP force, represents the dielectric properties of particles and suspending medium under different frequencies of the electric field applied. If the permittivity of a particle is greater than that of the suspending medium ($K(\omega)$>0), a positive DEP (p-DEP) is generated in this mode, where the particle migrates to the region of a strong electric field. However, if $K(\omega)$<0, the motion of the particle is repelled from the region of a strong electric field, which is termed negative DEP (n-DEP).

In our focusing experiment, the particles exerting an n-DEP force will be levitated in the suspending medium. Theoretical modelling of the CM factor for different particles types was reported by Park *et al* [129]. The DEP force also relies on the square of the applied field, which implies that the larger the electric field applied, the greater DEP force will act on the particles. The magnitude of the DEP force reduces exponentially with increasing distance above the electrodes, which drives the particles to an equilibrium position by balancing the DEP force and a sedimentation force F_{grav} in the *z*-direction. The equilibrium position of a given particle is tunable by applying a different electric field (Figure 3-1 b).

When fluid passes through a curved channel, the fluid near the centre has a higher inertia than fluid close to the walls and tends to move outwards around a curve that in turn creates a pressure gradient induced by the anisotropy of flow resistance. Because the channel is sealed, fluid near the walls recirculates inwards due to the centrifugal pressure gradient, inducing two symmetric vortices which are called Dean flows [24]. In a curved channel, two dimensionless numbers that characterise the Dean flow are defined as the Dean number $De = \mathrm{Re}(H/2R)^{1/2}$ and curvature ratio $\delta = H/2R$, where R is the radius of the curvature of the channel and H is the width of the channel. The Dean flow velocity scales as $U_D \sim De^2$ [24].

In the CSM (Figure 3-2), due to the low resistance provided by grooves in the cross section, fluid will fill the grooves and induce a transverse movement within the channel. The pressure of the fluid in the central grooves is higher than that at the sides. This anisotropic structure generates a pressure gradient from the central grooves to the sides which induces helical recirculation [4], where the helical streams rotate like a gear following a sequence of upwards, deviation, downwards, focusing, and then upwards again (the insets of Figure 3-2 a).

Particles suspended in the medium have helical motions that follow the flow of the fluid. Particles also experience four stages in each cycle: deviation, downwards, focusing, and upwards (Figure 3-2 b). This deviation in the flow brings particles to the side of the channel where the velocity is relatively low in bulk flow (the blue line in Figure 3-2 b). The particles move down in downwards flow and then the focusing flow brings the particles to the centreline of the channel where the velocity in bulk flow is higher than at the walls. Meanwhile, particles will migrate along the bottom of the channel and then move up following upwards flow. The cycle of focusing and upwards is longer than deviation and downwards (as shown in Figure 3-2 b), mainly because the particle velocity during focusing and upwards is faster than deviation and downwards. In this way, the particles will move back and forth in the channel.

Hydrophoresis utilises a steric hindrance mechanism to separate or focus particles under a pressure gradient induced by anisotropic flow resistance [26]. The steric effect arises when atoms in a molecule are brought too close together. Atoms are likely to occupy preferred positions rather than overlap each other, a principal that works well in micro-scale physics. As a giving particle (D in diameter) reaches the proximity of the sidewall, then Dean flow brings it to the central area of the channel and pushes it upward, driving it to align with the surface of the groove (as shown in Figure 3-2 b and Figure 3-3 a left). When a particle is comparable in size to the height of the channel (H_g), steric hindrance prevents a particle following the Dean flow. Thus, particles keep moving near the sidewall instead of migrating back and forth in the channel. This hydrophoretic ordering is largely determined by the height of the channel. Where $D/H_g \geq 0.5$, the grooves begin to hinder particles following the Dean flow induced by anisotropic microstructures and causes hydrophoretic ordering [26].

In short, the interaction between particle and groove deflects those particles that are almost the same size as the height of channel from their normal trajectories and leads to a new equivalent flow path which is called hydrophoretic ordering. Those particles experiencing a negative DEP force will be levitated in the suspending medium in the presence of the electric field, which leads to more interaction between particles and grooves. Therefore, even though the diameter of the particles is less than half of the channel they still have some possibility for hydrophoretic ordering when they migrate along the equivalent flow paths and remain close to the sidewalls of the channels without deviation after the electrodes have been activated (Figure 3-3 a). The height that particles are levitated relies on the magnitude of the electric field. Assuming that the particles are pushed high enough to lead to hydrophoretic ordering, they will focus on the sidewalls of the channel, but larger particles, exerting a greater DEP force, will be levitated to a higher position in the *z*-direction, which means the interaction between particles and grooves is more intensive and hydrophoretic ordering will arise easily. Therefore, whether the particles can be focused on each side of the channel or not is tunable.

3.3.2. DEP-assisted hydrophoretic focusing

We first tested the effect of applied voltage on DEP-assisted hydrophoretic focusing. Using the device with crescent-shaped grooves and interdigitated electrodes, we observed that beads passing through them showed different patterns. In this experiment 10 μm diameter particles were introduced and the flow rate was 20 μL min^{-1}. The trajectories of the particles in each image were captured at a time interval of 1/7 s and the images were superposed. The particles were smaller than half of the height of the channel in diameter, which did not satisfy hydrophoretic ordering, so they migrated back and forth inside the channel (as shown in Figure 3-2 b) and could not form hydrophoretic focusing (the right of Figure 3-4 a) without an electric field. However, the particles did tend to focus on the sidewalls of the channel when a voltage of 5 V_{p-p} at a frequency of 1 MHz (the right of Figure 3-4 c) was applied. At this frequency beads experienced a negative DEP force and were levitated to a higher position in the channel which resulted in a more intensive steric interaction between particle and groove that led to hydrophoretic ordering. Regardless of their initial positions, beads were focused

onto each side of the channel. As Figure 3-4 e shows, the focused positions were closer to the sidewalls of the channel as the voltages increased, such that the higher the voltages applied, the less focused were the widths.

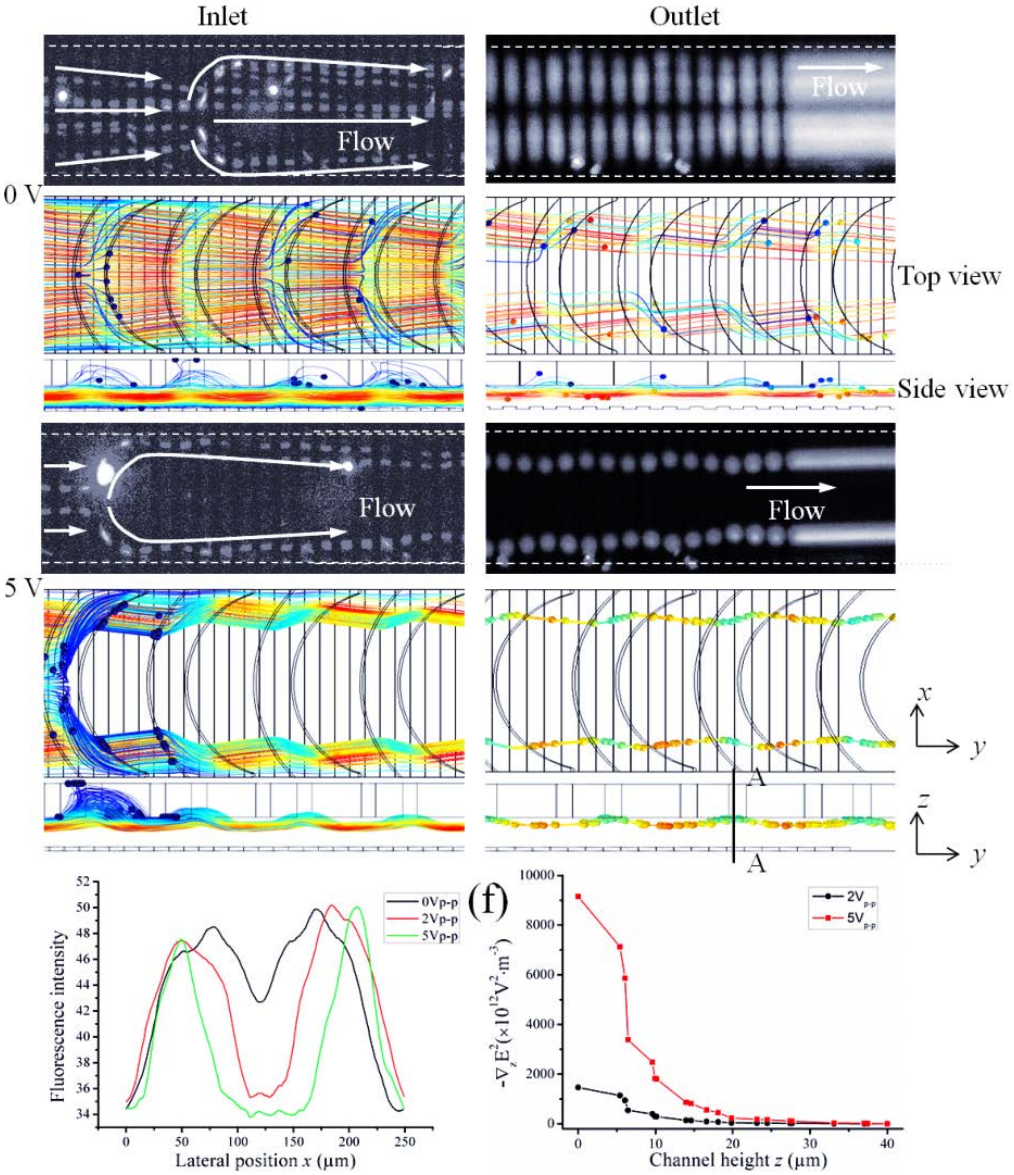

Figure 3-4 Experimentally focused patterns and numerically predicted particle trajectories of 10-μm particles at various voltages. The applied flow rate was 20 μL min^{-1}. The beads were evenly distributed at the inlet. The simulation geometry had the same geometric dimensions with the experimental channel. Optical micrographs showing the voltage-dependent focusing positions of (a) 0 Vp-p and (c) 5 Vp-p. (b) Particle trajectory at both the inlet (Left) and the outlet (Right) without an external voltage. Particles migrated back and forth and were not focused in the channel. (d) Particle

trajectory at both the inlet (Left) and the outlet (Right) at voltages of 5 Vp-p. Particles focused onto the sidewalls of the channel with the effect of steric hindrance. (e) Measured focusing profiles under different applied voltages. (f) Plot of the calculated gradients of the square of the applied field in the z-direction along the line, A-A.

Next, we examined the effect of the flow rate on DEP-assisted hydrophoretic focusing. The influence of the flow rate on the focusing position and width of the particle was investigated in the CSM with voltages of 5 V_{p-p} applied and a flow rate ranging from 10 to 200 μL min^{-1}. Particles of 13 μm were introduced into the CSM. The crescent-shaped grooves in a channel were omitted, and the linear velocities of particles flowing through the 250 μm wide by 45 μm high channel ranged from 1.48 to 29.63 cm s^{-1}. Figure 3-5 showed that the beads were focused on each sidewall of the channel and had two separated peaks from 51.19±7.76 μm and 190.79±7.76 μm to 43.43±6.20 μm and 196.28±6.20 μm, and a flow rate that changed from 10 to 150 μL min^{-1}. Although the flow rate was up to 150 μL min^{-1}, the particles were still focused well into the channel.

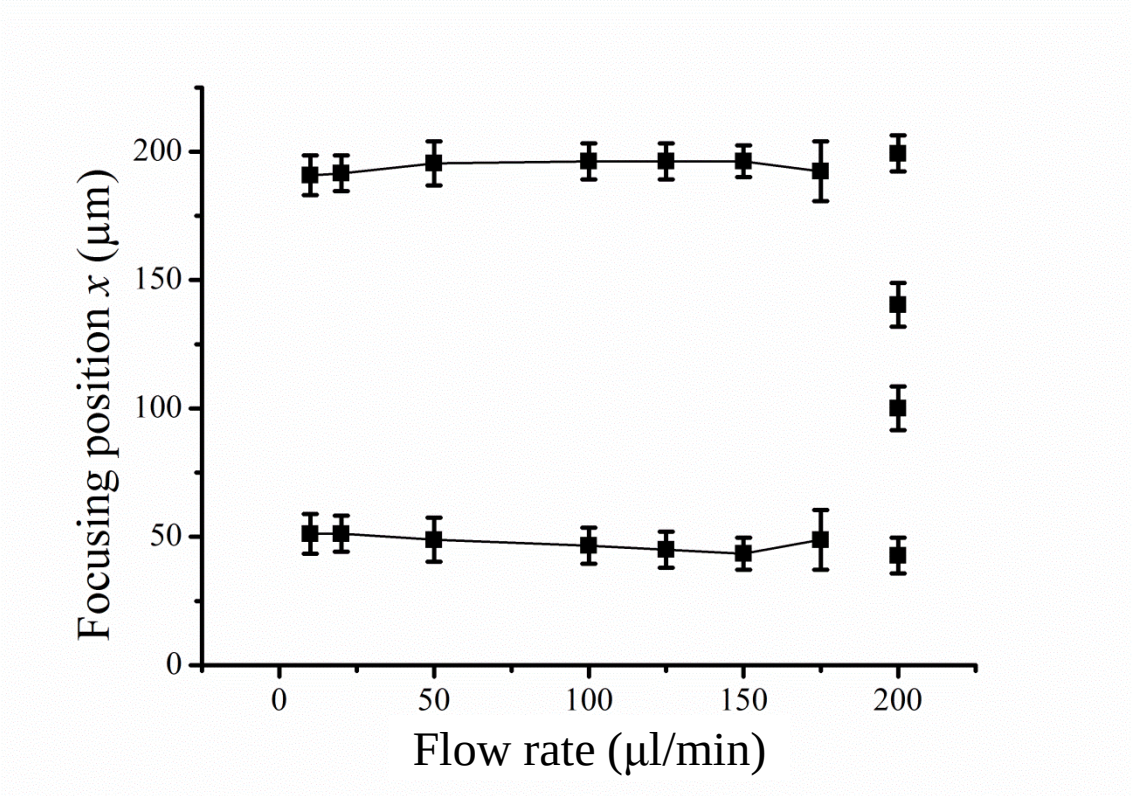

Figure 3-5 Focused positions and widths of the 13 μm particles. The flow rate was changing from 10 to 200 μL min^{-1}. The applied voltage on the electrodes was 5 Vp-p. Each focusing position and width were obtained from measuring the fluorescent profile.

We then investigated the effect of particle diameter on DEP-assisted hydrophoretic focusing. Particles of 8-, 10-, and 13-μm diameter were introduced into the micro-channel at a flow rate of 20 μL min^{-1}. Figure 3-6 a shows the focusing profiles with different particle diameters and without an external electric field. The particles were evenly distributed at the outlet as they were injected from the inlet. Although the 13-μm particles had a tendency to focus on the sides of the channel, some particles moved towards the centre of the channel. Those particles with different diameters had clear focusing profiles at an applied voltage of 8 V_{p-p} (Figure 3-6 b), and the separated peaks were symmetrical about the centreline of the channel. As we increased the voltage from 0 to 8 V_{p-p}, the focusing widths of particles with different diameters decreased rapidly (Figure 3-6 c). The focusing widths fell from 86.65 to 23.81 μm for 8-μm beads. We observed a similar trend with the 10-μm beads, where the focusing widths were 82.46, 38.72, 20.40, and 15.30 μm for 0, 2, 5, and 8 V_{p-p}, respectively. With the 13-μm beads,

the focusing width decreased to 17.05 μm at a voltage of 2 V_{p-p}. Then the focusing width reduced to 13.94 μm when the voltage applied went to 8 $V_{p-p.}$

Most cells in nature are not completely spherical and exhibit distributions in cell size. To verify whether non-spherical particles can be focused in our DEP-assisted hydrophoretic device, MEL cells (12 μm in diameter) were used in our experiment. The cells passed quickly into the channel, which proved difficult to capture with the CCD camera, so a flow rate of 1 μL min^{-1} was selected. In this condition, the trajectories of the cells were recorded in micrographs with stretched lines, as shown in Figure 3-7 a. The inset describes the morphology of MEL cells. The lateral positions of the cells were measured, and then the number of particles that appeared in different positions was counted manually (Figure 3-7 b). After passing the microfluidic device, approximately 44.2% and 50.7% of the MEL cells went through the channel within the lateral range from 25 to 75 μm and from 175 to 225 μm.

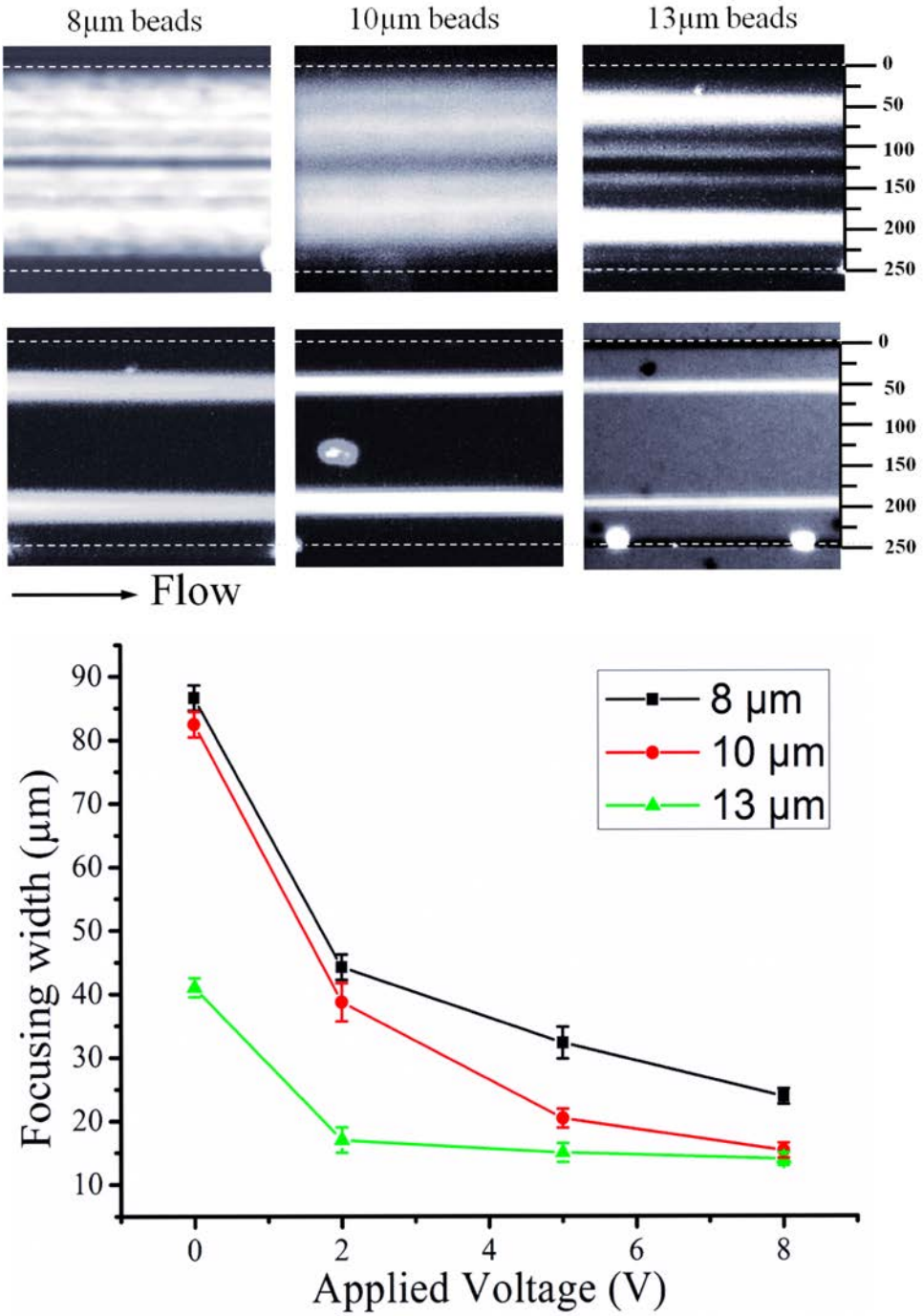

Figure 3-6 Focusing patterns of 8-, 10-, and 13- μm particles. The applied voltage was changing from 0 to 8 V_{p-p}. The applied flow rate was 20 μL min^{-1}. The particles had a uniform distribution at the inlet. (a) Optical microscopy images showing the size-dependent focusing patterns in the absence of applied voltage and (b) at an applied voltage of 8 V_{p-p}. (c) Measured focused widths from the fluorescent profiles. Average value of 3 times of measurement.

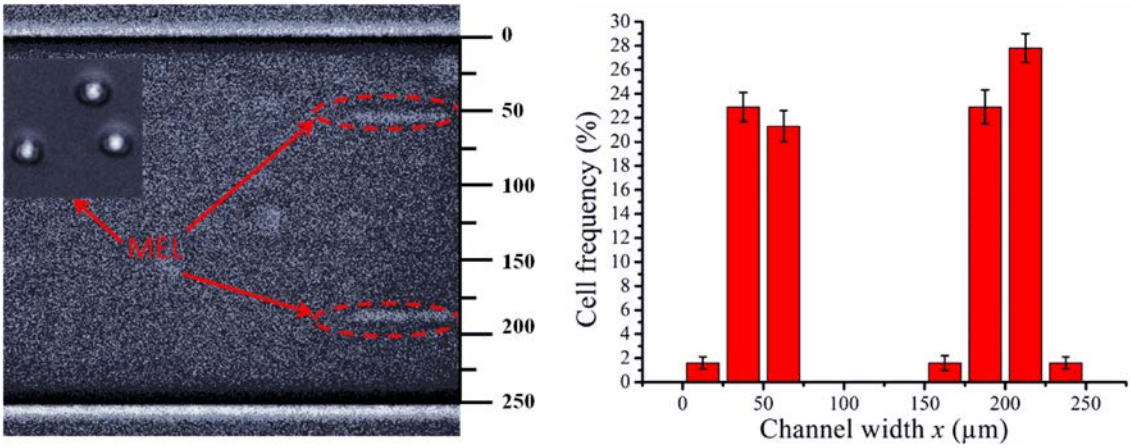

Figure 3-7 Focusing patterns of MEL cells. The applied flow rate was 1 μL min^{-1} and applied voltage was 5 V_{p-p} at a frequency of 10 MHz. The cells were evenly distributed at the inlet. (a) Optical microscopy images showing the focusing patterns of the cells in the microfluidic device. The inset describes the morphology of the cells. (b) Cell frequency at different lateral positions. Average value of 3 times of measurement.

3.4. Discussion

In order to better understand these DEP-assisted hydrophoretic phenomena, a numerical simulation was conducted utilising COMSOL software and the particle trajectories and electric fields were calculated. The particles utilised for this simulation were 10 μm in diameter. A fluid flow was applied along the *y*-axis at a flow rate of 20 μL min^{-1}. The particle trajectories were simulated without an electric field and with an electric field in Figure 3-5 a. This software has some drawbacks; the particles were immobilised when they touched the groove, which is a mismatch to the actual situation, and we also plotted the calculated gradients of the square of the applied field in *z*-direction along the line A-A in Figure 3-4 d to investigate the electric fields at various voltages.

Without an external electric field, particles that were released evenly into the inlet occupied the whole channel in the *z*-direction (the left of Figure 3-4 b), but after the electrodes were excited, the particles were pushed into a narrow space in the channel where the steric interaction between the particles and grooves occurred (Figure 3-4 d). In this way the 10 μm-diameter microspheres remained in their focused position, which perfectly matched the experimental results (Figure 3-4 c). Figure 3-4 f shows the simulated gradients of the square of the field applied in the *z*-axis at 2 and 5 V_{p-p}

voltages where the maximum intensity of the electric field gradient at 5 V_{p-p} was ~5 times as high as that at 2 V_{p-p}. The gradients of the electric field reduced exponentially as the distance above the electrodes increased, which is consistent with the conclusion from Pethig *et al*. [139]. Compared to a voltage of 2 V_{p-p}, the particles located at the lower position (~20 μm or less) exerted a larger DEP force and pushed quickly to higher positions when a voltage of 5 V_{p-p} was applied. Thus, the focusing performance at 5 V_{p-p} was better than that at 2 V_{p-p}

As Figure 3-5 shows, the increasing flow rate had little effect on the focused position, a result that was consistent with the previous work of Park and Choi [27], who reported that the particle position was independent of the flow rate when the flow rate range was less than 5 μL min^{-1}. The maximum flow rate for focusing with good performance in our experiment was ~30 times as high as that reported by Park and Choi [27]. The pressure gradient between the centre and sidewall of the channel increased with the increasing flow rate and forced the particles to move slightly closer to the sidewall of the channel. However, after the flow rate increased to 175 μL min^{-1} the particles focussed very well and the focusing position moved to the centreline of the channel and increased in width. When the flow rate went to 200 μL min^{-1} the particles did not focus any more. Since the particles passed through the channel very quickly, they were exposed to the electric field for a shorter time and could not be levitated high enough to generate a hydrophoretic ordering so the focusing performance deteriorated.

The influence of particle diameter on the focusing width was strong because the larger particles experiencing a higher DEP force had a higher equilibrium position by balancing the DEP force and gravity in the *z*-axis. Therefore, larger particles were pushed into a narrower space where hydrophoretic ordering occurred easily and the particles were focused onto the sidewalls of the channel. Because the magnitude of the electric field gradients reduced exponentially as the distance above the bottom of the channel increased (Figure 3-4 f), they remained almost the same when the height was up to 20 μm or more, and as the applied voltage increased. Once the particles levitated to 20 μm or more high, where the DEP force was less dominant, the focusing performance changed slightly with an increase in the external electric field (Figure 3-6 c). Figure 3-7 b showed the focused positions of MEL cells were symmetrical about the centre of the

channel, which showed a similar focusing movement with the beads. Even though the diameter of the MEL cells was less than half of the channel height, which did not satisfy the condition required for hydrophoretic ordering, they were still focused on the sidewalls of channel at 5 V_{p-p}. Therefore, the DEP-assisted hydrophoretic device can be utilised for biological cells and it will provide a tunable microfluidic system for clinical diagnostics.

3.5. Conclusion

The present work proposed a new concept of DEP-assisted hydrophoretic focusing which was a combination of DEP and hydrophoresis. The critical limitation of DEP operating at a low flow rate and the specific hydrophoretic device for focusing a giving size of particles were overcome in our microfluidic device. The focusing performance was tuneable and relied on the applied electric field. The DEP-assisted hydrophoretic device was utilised for focusing polystyrene fluorescent particles with 8, 10, and 13 μm diameters. The motion of the microparticles was investigated and explained explicitly with numerically simulated particle trajectories and electric field gradients. The simulated particle trajectories perfectly matched to the experimental results. Also, MEL cells were used to demonstrate the effectiveness of the new microfludic device. Compared with the flow rate of the traditional hydrophoretic device (~10 μL min^{-1} or less), high-throughput was achieved in our DEP-assisted hydrophoretic system by increasing the flow rate to 150 μL min^{-1}, in which the focusing performance still kept well. In conclusion, the microfluidic device not only can potentially be applied for particle enrichment, filtration and flow cytometry, it also facilitates the connection with other microfluidic platforms for particle separation and detection.

4. Isolating plasma from blood using a dielectrophoresis-active hydrophoretic device*

4.1. Introduction

Human blood including leukocytes or white blood cells (WBCs), erythrocytes or red blood cells, and platelets and plasma [33]. WBCs play a significant role in the immune system, account for 1% of whole blood cells, and range from 7 to 30 μm in size. Red blood cells have a discoid shape and are 7 to 8 μm in size; they are the most common cells, accounting for 98% of all blood cells [34]. Platelets are 1 to 3 μm in size and are responsible for formatting blood clots [35]. Plasma is a straw coloured aqueous medium free of cells that acts as a host to a myriad of analytes containing metabolites, proteins, circulating nucleic acids (CNAs), and other organisms. An accurate analysis depends on the plasma being totally free of cells, and therefore the contaminants which might otherwise influence the results of any detection must be removed [34].

Two conventional mechanisms – centrifugation and filtration – remain the most common methods of separating blood plasma in the laboratories [140]. While these methods are simple, the procedures are generally labour intensive, time-consuming[34], and sometimes can impair the collection of analytes of interest (e.g. high-speed centrifugation with > 3000 *g*). The recent advance in microfabrication and microfluidics technologies has provided the impetus for developing microfluidic techniques for blood plasma separation. Microfluidic techniques have many advantages over conventional methods such as use of small volume of blood samples (e.g., microlitres instead of millilitres), short analysis time (e.g., seconds to minutes), user-friendliness and capability of automation. Use of microfluidics can lower the analysis cost significantly and miniaturise the analysis device, making it attracting for portable and low-cost analysis of biological samples.

* Results of this chapter are published in: Sheng Yan, Jun Zhang, Gursel Alici, Haiping Du, Yonggang Zhu, Weihua Li, Isolating plasma from blood using a dielectrophoresis-active hydrophoretic device. ***Lab on a Chip***, 14, 2993-3003, 2014.

Microfluidic techniques are usually categorised into an active and passive isolation of plasma from whole blood. Passive separation methods can sort particles by their physical characteristics such as size, shape, and density, using only the shapes of the micro-channels or micro-structures embedded in the micro-channels, the flow, and the hydrodynamic forces. Sedimentation is the oldest method and has been adapted to micro-scale systems for collecting plasma [141]. Although undiluted whole blood can be easily operated in microfluidic sedimentation devices, the separation throughput is relatively low because any increase in the flow rate will cause inefficient separation. Hence, each experiment will last several hours. Microfiltration is another example of taking the macro-scale principle into the micro-scale world for isolating plasma. Membranes and pores have been designed to prevent blood cells from passing through so the plasma can be extracted from blood [142-144]. However, the major bottleneck with these methodologies is the problem of clogging, which affects their performance after the filter becomes saturated. Thus, these techniques can only operate under a given volume and with a diluted sample before the filters become saturated. The deterministic lateral displacement (DLD) was first proposed and verified by Huang *et al*. [45] with micro-pillars within a micro-channel. This method was successfully applied to separate blood cells and isolate plasma [33]. It still suffers from various drawbacks such as the need for an extremely low flow rate, a precise sheath flow, and the high cost of fabrication. Meanwhile, the narrow gaps between the pillars embedded in the micro-channel bring the risk of clogging. Hydrodynamic separation techniques that depend on viscous forces are generally used to separate the plasma from blood. Yang *et al*. [145] designed a novel microfluidic device that used the Zweifach-Fung law where 100% purity (image analysis) was achieved with 25% plasma yield and an extraction rate of 4 μL min^{-1}. In the microchannels, the Reynolds number ($Re = Ud/\nu$, where U is the flow velocity, d is the channel width and ν the kinematic viscosity of the fluids) is very low (i.e., Re <=1), the viscous force dominates and the flow is laminar. Therefore, hydrodynamic separation operates at low Re in most blood extraction processes. Di Carlo[24] and our group [146] demonstrated that the inertial lift forces can actually focus and separate microparticles and cells at higher Reynolds numbers. Di Carlo *et al*. [147] introduced a device using such a principle to separate plasma and bacteria from blood cells. Although a high flow rate was achieved in an inertial microfluidic device,

the small cells (*E.Coli*) cannot be focused well and were not entirely separated from the blood. The plasma was not free of cells, which will influence the results of further analysis. Recently, Choi *et al*. proposed a novel approach to sort and focus micro-particles in micro-channels with slanted grooves, called hydrophoresis [4, 27-29, 32, 42]. Hydrophoresis is a sheathless and passive technique that utilises anisotropic micro-structures to induce a pressure gradient [29]. The concept of hydrophoresis was verified by purifying platelets from blood using a fast method for low stress and high throughput [35]. A hydrophoretic filtration device was also used to isolate the white blood cells (WBCs) from red blood cells [36]. Although hydrophoresis is a powerful and robust sorting mechanism, it still has some limitations. For instance, according to hydrophoretic ordering that has been studied experimentally, only particles with diameters normally larger than half of channel height can be ordered and focused [32]. For separating platelets with a diameter of 1-3 μm in a hydrophoretic device, the maximum height of any gaps should be less than 6 μm, which prevents the passage of WBCs and red blood cells through the micro-channel. Therefore, plasma cannot be effectively isolated in hydrophoretic devices. In the hydrophoretic filtration experiment, the WBCs (D>8 μm) could not flow through the channel easily that was 7.8 μm high and with an obstacle height of 4 μm, which might lead to clogging. Moreover, high throughput is difficult to achieve in such narrow channels. Even though parallelisation strategy can be used to increase the throughput, it is impossible to fabricate channels with different sizes which are required for different biological samples.

Active techniques using external force fields such as acoustic [6], magnetic [7] and dielectric [8-19] can also be used to sort particles or cells. Acoustic forces induced by high-frequency resonators rely on their size, density, and compressibility [96]. Even though the theory of magnetically isolating plasma from whole blood exists, it is impractical because of the need for additives to supply paramagnetic red blood cells [34]. As for isolating plasma electrically, little work has been reported so far. Nakashima *et al*. [148] proposed a system of combining capillary and dielectrophoretic forces for isolating plasma where the cells were attracted to weak electric fields under negative DEP forces while the plasma was collected by capillary forces. However, the plasma yield was very low (6%) under a voltage of 10V at 1MHz. No external mechanical sources such as centrifugal machines and syringe pumps were used in this

experiment at the expense of time. Unlike their passive counterparts, active methods have a low flow rate and required specialised buffers. To the best of the authors' knowledge, the use of hydrophoretic devices to extract plasma has not been reported and very few DEP devices related to plasma isolation at high flow rate have been presented. The flow rate of hydrophoretic devices is relatively high compared to that of DEP devices. The DEP force can be tuned by varying the external voltages to manipulate particles, and has the potential for setting up a tunable system. Combining DEP with hydrophoresis thus benefits the best from the two methods. In a previous work, the concept of "DEP-assisted hydrophoretic focusing" was proposed and it was shown that the focusing patterns of particles (>8 μm in diameter) could be modulated by varying the voltage at a high throughput [149]. However, the separation of both small and large particles has not been demonstrated.

The aim of this paper is to report the new development of the device that can separate both large and small particles with high throughput. Such a development can find applications in a range of applications such as sensor devices, pathology test and so on. The brief outline of the paper is as follows. Section 4.2 will introduce experimental details including methodology, device design, materials and experimental setup. Numerical simulation will be introduced in Section 4.3. The main results will be presented in Section 4.4 which include both numerical and experimental data and an application example of blood plasma separation. The main conclusion will be drawn in Section 4.5.

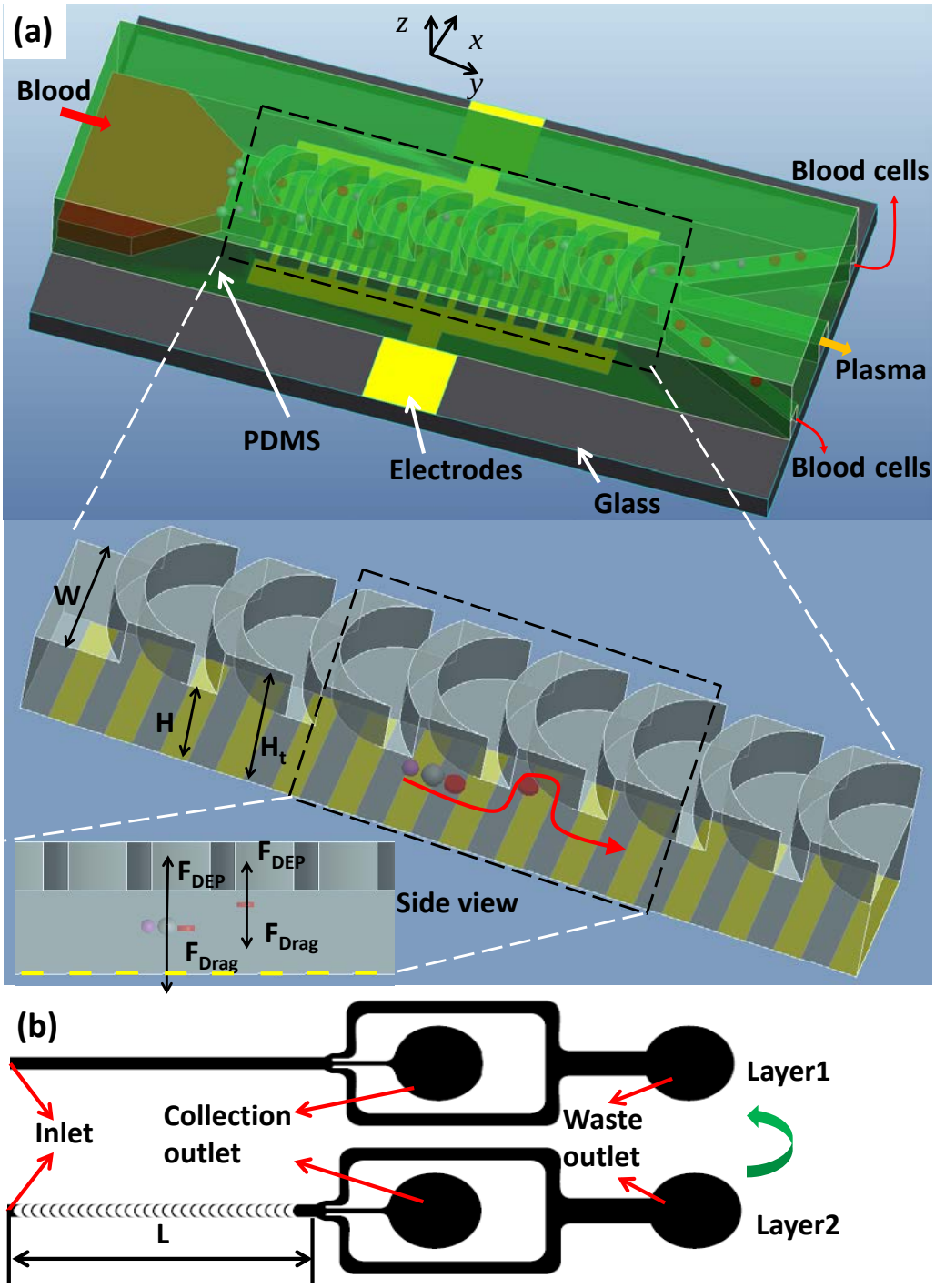

Figure 4-1 Isolation of plasma in a DEP-assisted hydrophoretic device. (a) Overview of microfluidic device showing the isolation of plasma. The insets shows large cells (Red blood cells and WBCs) and small cells (platelets) can be focused onto the sidewall by a steric hindrance mechanism under a certain external electric field, and forces exerted on the cells on different cross sections. (b) Schematic illustrating two-step

photolithography. Layer 2 with 30 grooves was aligned and placed on top of layer 1. Blood plasma is collected from the collection outlet.

4.2. Experimental details

4.2.1. Methodology

To separate both large and small particles, a new design is proposed with optimized flow and DEP conditions. The flow velocity is reduced to allow for the separation of smaller particles. A higher DEP voltage will be used in order to generate larger DEP force to push smaller particles high enough in the channel. To increase the throughput, a larger channel cross section is used.

The mechanism of hydrophoresis has been studied experimentally [35]. The critical diameter to be focused in the channel is defined as half the height of the channel. Normally, particles travel back and forth along the transverse direction following the rotational flow. However, particle-groove interaction diffuses the large particles whose diameters exceed the critical diameter out of their streamlines and lead to equivalent flow paths; this is called hydrophoretic ordering. In our experiments, the particles exerting a negative DEP force will be levitated in the suspending medium. The DEP force also depends on the applied field and the diameter of particles, respectively, which implies larger particles or cells have a higher levitation position and a higher voltage also tends to push particles or cells to a higher level in the channel. Therefore, interdigitated electrodes were patterned onto the bottom of the channel so that particles exerting a negative DEP force were pushed into a narrow space. As a result, the particles have more opportunity to interact with the grooves and induce hydrophoretic ordering by steric hindrance. Hence, large and small particles or cells (3 μm and 10 μm particles, and Red blood cells, WBCs, and platelets) can focus simultaneously in our DEP-assisted hydrophoretic device under the appropriate flow rate and applied voltage even though their diameters are less than the critical diameter, which enables all the blood cells to separate from the blood and obtain plasma with high purity.

Two important factors were used to evaluate how well the blood plasma separated with regards to its purity and yield. The purity of plasma is defined as: $1\text{-}c_p/c_f$, where c_p is the number of red blood cells per milliliter in the collection outlet and c_f is the number of

red blood cells in the inlet fraction. The yield of plasma is the percentage of the volume of collected plasma from the collection outlet over the total volume of blood. Our DEP-assisted hydrophoretic device is a flexible and tunable system that can focus the lateral positions of particles by changing the external voltages without redesigning and fabricating a new channel.

4.2.2. Design and fabrication of a DEP-assisted hydrophoretic device

Figure 4-1 shows a schematic drawing of the microfluidic device. The width of the channel is the key factor that impacts on the focusing positions of different particles. When the channel is wider than 400 μm, particles with different sizes are focused onto the sidewall of the channel with a small deviation known as the focusing mode [29]. A 500 μm wide microfluidic channel is designed so that all the blood cells with distinguishing diameters can work in a focusing mode and will have slightly different focusing positions. The WBCs, red blood cells, and platelets migrating along the sides of the micro-channel are collected from the waste outlet, while the free-cell plasma is extracted from the collection outlet.

Those particles with diameters D that are larger than half of the height of the main channel H assumed hydrophoretic ordering [26]. The steric interaction between grooves and beads deflects particles from the rotational flow and leads a new equivalent flow path. This anisotropic structure generates a pressure gradient from the sides of the channel which induces a rotational flow consisting of upward, focusing, downward, and deviation flow (Figure 4-2) [4]. Such convective vortices drive cells that move in the cross section and follow the rotational flows. When the large cells with diameters larger than half the height of the channel move to the sides of the channel, the steric effect induces the cells to diffuse out of convective vortices and remain near the sidewalls (Figure 4-2 a). When the small cells reach the sides of the channel they go downwards and deviate from the sides by focusing flow. In short, the steric hindrance for small cells is negligible so they can migrate back and forth in the micro-channel without focusing.

The DEP-assisted hydrophoretic device was designed to improve the throughput of this device. The micro-channel height for the two sections are H_t=90 μm and H=45 μm, respectively. The blood cells could not form hydrophoretic ordering in our experiments

because the largest blood cells were approximately 10 μm in diameter. Therefore, micro-electrodes were used to generate the non-uniform electric field where the negative DEP force would levitate the cells into a higher position in the *z*-direction and enhance the cell-groove interaction and generate hydrophoretic ordering. The higher position the cells have, the easier they form hydrophoretic ordering, and therefore the small cells (platelets) could also be focused in the micro-channel after applying a strong electric field (Figure 4-1). The channel W was 500 μm wide and H_t=90 μm high, the main channel was H=45 μm high and its length was L=10 mm. The grooves were crescent shaped with a small curvature of 250 μm and a large curvature of 300 μm (Figure 4-1 b and Figure 4-2).

The double-layer master mould was fabricated on a silicon wafer using two-step photolithographic techniques. The first layer of photolithography was defined as the main channel; the second one with the pattern of grooves was aligned to lie on the top of structures in the first layer. The first layer of photoresist (SU-8 2050, MicroChem Corp., Newton, MA) was spun on a clean silicon wafer by a three-step coating cycle (500 rpm for 20s, 2000 rpm for 20s, and 4000 rpm for 40s). Then, the silicon wafer was baked at 65 °C for 2 minutes and 95 °C for 7 minutess. After exposed to UV light through the first photomask, another two-step hard bake (65 °C for 3 minutess and 95 °C for 7 minutess) was conducted. Afterwards, the SU-8 pattern was developed in SU-8 developer solution for 6 minutess and rinsed with isopropyl alcohol (IPA). In the second-step lithography, the photoresist was spin-coated on the previous mould, which was the same procedure with first-step photolithography. The second photomask was carefully aligned with the previously developed SU-8 patterns and then UV light went through the second photomask to expose the second layer of photoresis. After baking and developing, the double-layer mold was treated by trichlorosilane to deposit a mono-layer of silane on the surface. A PDMS mixture with 10/1 ratio of the curing agent (Dow Corning, Midland, MI) was poured over the silicon master, degassed and baked at 65 °C for 2 h. The devices were peeled off from the silicon master and inlet and outlet holes were punched with a custom needle tip. The PDMS was sealed with glass slides after exposure to oxygen plasma (PDc-002, Harrick Plasma, Ossining, NY) for 3 min. Other details of this fabrication can be found in our previous work [137, 150].

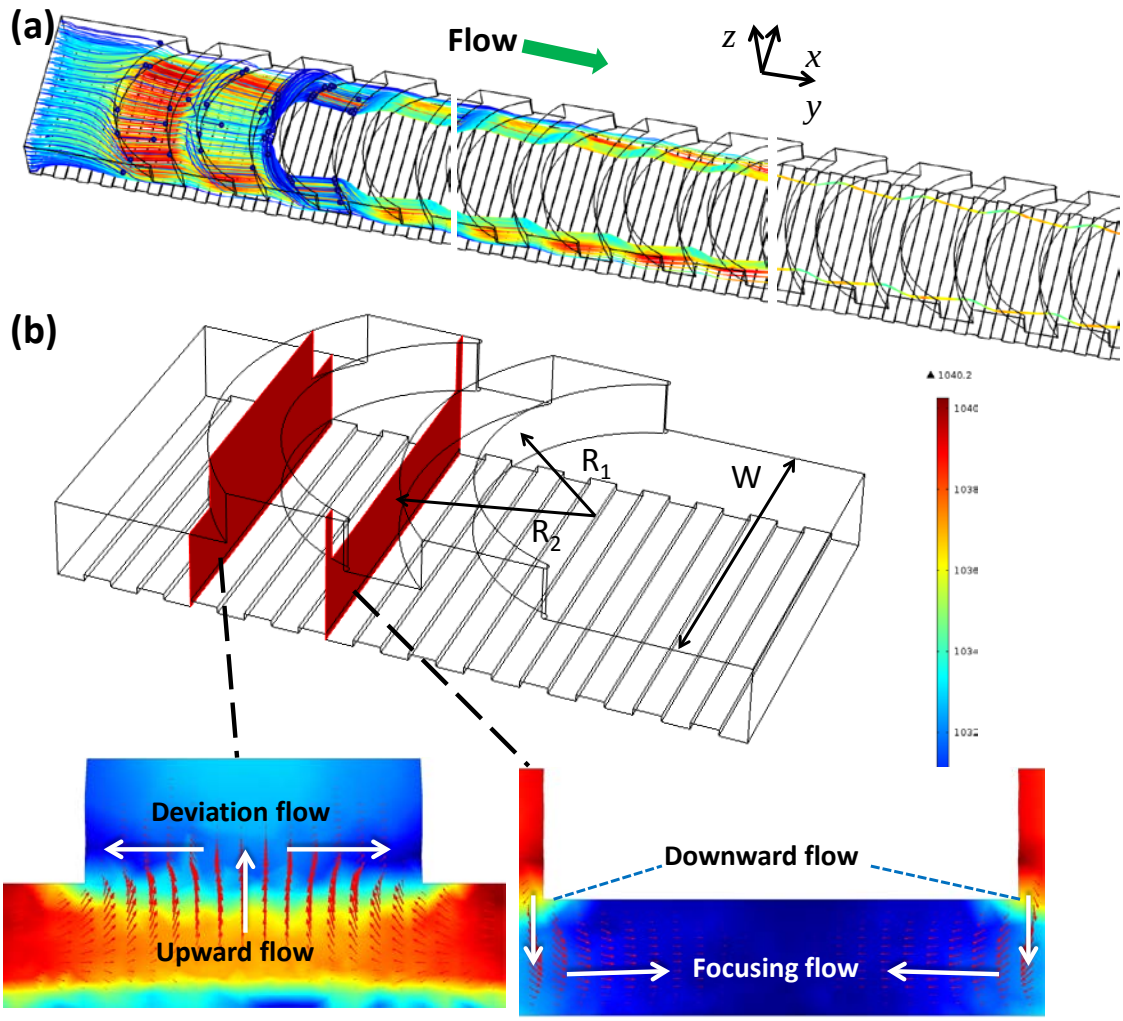

Figure 4-2 (a) Simulated particle trajectories in three sections of the mcirochannel. Left image shows the entrance section of the microchannel, middle image the middle section and right the exit section. The steric effect makes the cells diffuse out of convective vortices and assume hydrophoretic ordering. The color of trajectories denotes particle velocity. The red represents high speed, while blue represents low speed. (b) The schematic diagram of the micro-channel and the simulated results of flow field and pressure in the cross-sections. The flow direction is along the *y*-axis. The anisotropic microstructure induces helical recirculation, composing of an upward, deviation, downward, and focusing flow. The red arrows in the insets are velocity vectors. The background color of the insets denotes pressure field. The scale bar refers to the value of pressure.

4.2.3. Material preparation

Red fluorescent microparticles with a diameter of 3 μm and green fluorescent beads of diameter 10 μm (Thermo Fisher Scientific., USA) were used in our experiments. They were suspended in deionized (DI) water, with Tween 20 (Sigma-Aldrich, Product No. P9416) added to this aqueous medium to impede the beads from sedimentation and aggregation. The human blood samples were extracted from a healthy donor. The samples were diluted 100× (0.45% hct) in an isotonic sucrose buffer before separating the plasma.

4.2.4. Experimental setup

A sinusoidal signal with frequency 1 MHz was generated by a waveform generator (33250A, Agilent, USA) and amplified by an RF power amplifier (TIA-1000-1R8-2, Mini-Circuits, USA). The applied frequency in all experiments was set to 1MHz. The copper wires soldered onto the pads were connected to the power amplifier to activate the electrodes. A syringe pump (Legato 100, Kd Scientific) was used to inject the particle suspension into the micro-channel. The microfluidic device was placed under an inverted microscope (CKX41, Olympus, Japan) and the particle trajectories were captured by a CCD camera (Rolera Bolt, Q-imaging, Australia). An image processing program, Q-Capture Pro 7 (Q-imaging, Australia), was used to measure the focusing positions and the widths of the beads. The concentration of particles or cells collected from different outlets was measured with a hemacytometer.

4.3. Numerical simulation

The particle trajectories and flow characteristics in the DEP-assisted hydrophoretic device were calculated using the finite element software (COMSOL Multi-physics 4.3 COMSOL, Burlington, MA). The geometry for simulation was identical to the experimental channel. The laminar flow module was utilised to solve the fluid flow in the three-dimensional model. For modelling the laminar flow of diluted ferrofluid inside the microchannel, continuity equation and Navier-stokes equation were expressed as: $\rho\nabla \cdot \boldsymbol{u} = 0$ and $\rho(\boldsymbol{u} \cdot \nabla)\boldsymbol{u} = \nabla \cdot [-p\boldsymbol{I} + \mu(\nabla\boldsymbol{u} + (\nabla\boldsymbol{u})^T)]$, where $\boldsymbol{u}$ is velocity vector of fluid, p is fluid pressure, and ρ is fluid density. No-slip boundary condition

was set to the channel walls. The physical property of fluid was set to incompressible flow. The flow rate at the inlet was set to 15 μl min^{-1} and the pressure at the outlet was set to zero. The electric currents module was employed to calculate the non-uniform electric field generated by activated electrodes. The equations to resolve the electrical potential are based charge conservation: $-\nabla \cdot \sigma \nabla V - J_e = 0$, where σ is the electrical conductivity (S m^{-1}), V is the electrical potential (V) and J_e (A m^{-2}) is an externally generated current density. The relation between the electrical potential and the electric field is given: $E = -\nabla V$, where E is the electric field strength (V m^{-1}). 20 V_{p-p} AC signal with a frequency of 1 MHz was applied to the electrodes. A frequency solver was used to compute the electric field. Finally, the particle tracing module can couple DEP force and drag force to simulate the particle trajectories. Also, the equation of DEP force and drag force was already embedded in the COMSOL without secondary development. Therefore, DEP force and drag force were automatically computed accord ing to the electric field and fluid field, respectively. At the inlet, particles were evenly released along with the channel width. The particle density and diameter were set to 1050 kg m^{-3} and 3 μm, respectively. Bulk conductivity and permittivity of the polystyrene beads are 2.4×10^4 S $m^{-1}$and 2.6 ε_0, respectively. The conductivity and permittivity of DI water are 1.5×10^4 S $m^{-1}$and 78 ε_0, respectively. $\varepsilon_0 = 8.85 \times 10^{-12}$ F/m is the vacuum permittivity. The time for beads migrating in the channel was set to 0.5 s and the interval time was set to 10^{-4} s, which provided smooth particle trajectories. In the *z*-axis, a DEP force and drag force were exerted onto particles in the DEP-assisted hydrophoretic device.

The drag force at low Reynolds numbers can be expressed using Stokes law [151]:

$$F_{drag} = -6\pi r \eta v_{mz} \qquad 4\text{-}1$$

where η refers to the viscosity of the medium, v_{mz} is the velocity of the flow.

The DEP and drag forces can be modulated independently. F_{DEP} changes with the applied voltage while F_{drag} varies with the flow rate.

4.4. Results and discussion

4.4.1. Modelling of particle trajectories

Figure 4-2a shows the simulated particle trajectories in the DEP-assisted hydrophoretic device. The flow rate applied along the *y*-axis was set to 15 µl min^{-1}. When released evenly from inlet, particles are pushed by negative DEP induced by an electric field to a high level in *z*-axis, where particles are mainly exposed to deviation flows. Thus, they will rapidly reach the sidewalls of channel following the deviation flow. Steric hindrance then occurs to prevent particles moving back and forth in the *x*-axis and keep them along the sidewalls. After that, the particles are focused gradually.

Figure 4-2b illustrates the schematic diagram of the micro-channel, and the insets are the enlarged view of the simulated velocity vectors and pressure field in two cross-sections around the grooves. The pressure field changes significantly around the grooves. The maximum pressure appears near the sidewalls and the pressure is smallest near the centre of the channel. The velocity vectors are identical with the pressure field, which drives the vortices consisting of upward, deviation, downward, focusing flows. Due to the anisotropic structure of the channel, the drag force in the cross-section varies periodically through the channel. The DEP forces, however, keep the constant value in the same height in the channel, which will push particles higher or lower to balance the drag forces. Therefore, the trajectories of particles are not ideally straight in the channel with grooves, instead of helical motion with a small radius (the inset of Figure 4-1 a).

4.4.2. Movements of 3 µm particle

Since the small beads are not easily focused in the microfluidic channel, the conditions for focusing 3 µm beads are first studied. The effect of voltage and flow rate on the focusing performance of 3 µm fluorescent beads are shown in Figure 4-3. The 3 µm micro-particles were injected into the device and distributed themselves evenly at the inlet as the flow rate was changed from 5 to 20 µL min^{-1} and the voltages varied from 10 to 30 V_{p-p}. Figure 4-3 a shows trajectories of particles along the whole channel, which agree reasonably well with the simulation result shown in Figure 4-2 a. Beads following the deviation flows are driven to the sidewalls of the channel. The steric effect occurs to remain the beads moving along the sidewalls. Finally, the particles are

focused into lines at the outlet. Figure 4-3 b shows the optical micrographs of particle trajectories of 3 μm beads passing the DEP-assisted hydrophoretic device. The time interval of each image was 1/7 s and the images were superposed.

Figure 4-3 c shows the focusing positions with different flow rates. The focusing positions of the 3 μm beads were symmetrical about the centre of the channel. As the flow rate is increased from 5 to 20 μL min^{-1} at an applied voltage of 10 V_{p-p}, the focusing positions of the 3 μm beads deviated from the sidewalls, changing from 70.6 and 424.3 μm, to 88.4 and 406.4 μm. Since the higher lateral pressure gradient was induced by the high flow rate from the sides to the centre of the channel, the beads were exposed to a higher transverse flow which deflected them away from the sidewalls of the channel. Therefore, the particles moved inwards as the flow rate was increased. Although similar behaviour was observed at voltages of 20 and 30 V_{p-p}, the variation of focusing positions with flow rate is much less pronounced when compared to that at 10 V_{p-p}. This variation is reduced even more at a higher applied DEP voltage. For example, at a DEP voltage of 30 V_{p-p}, the particles migrated closer to the sidewalls and remained so along the whole channel. The small variation of focusing position along the channel can be regarded as a stable condition in our experiment. With the increase of voltages, the focusing positions of the particles allow the focusing width to be estimated (Figure 4-3 d). A voltage of 10 V_{p-p} The focusing width increased significantly with the increasing flow rate in the range studied, i.e., from 5 to 20 μL min^{-1}. The beads were not levitated high enough to form hydrophoretic ordering because a low electric field was generated and a high flow rate was applied. The beads were not focused along the sidewalls of the channel anymore. Instead, the beads were migrating back and forth from the sides to the centre of the channel. In contrast, at the applied voltage of 20 and 30 V_{p-p}, the effect of flow rate on the focusing width is almost negligible. There is only a slight increase of the focusing width with the flow rate at 20 V_{p-p}.

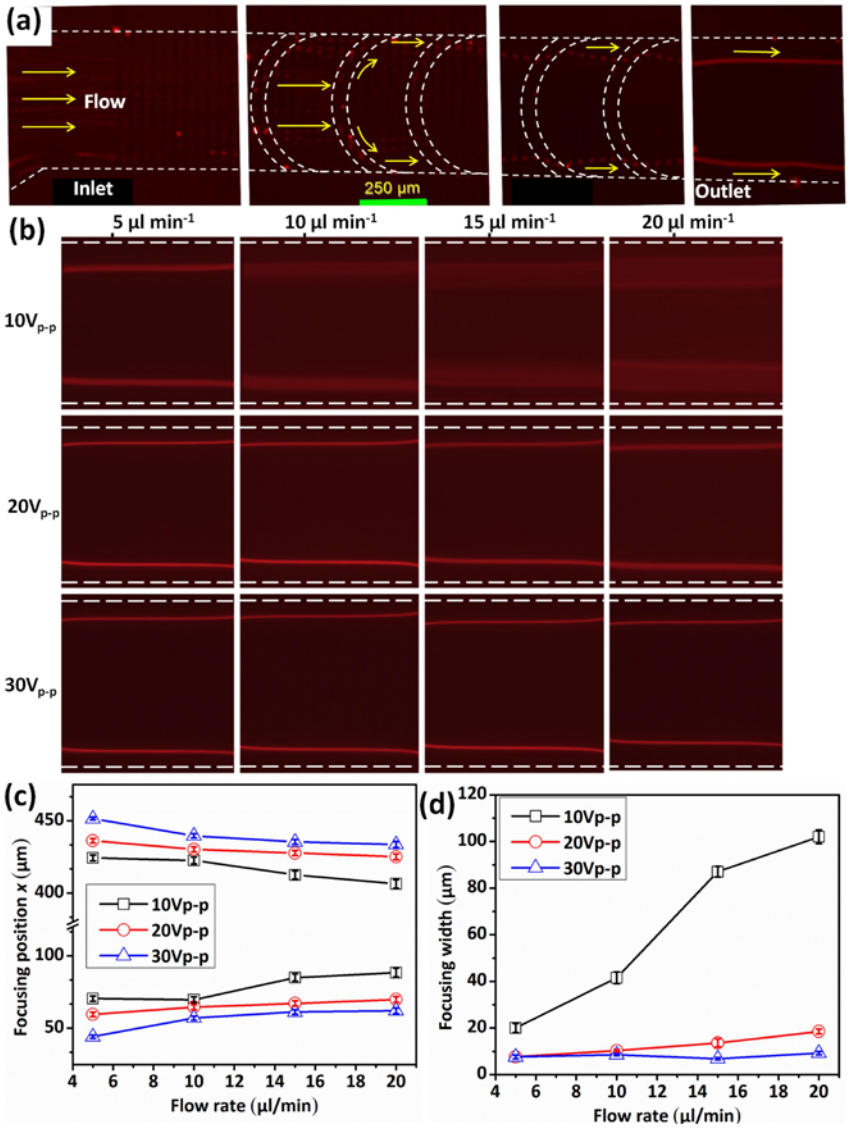

Figure 4-3 Focusing patterns of 3-μm particles. The applied voltage was changing from 10 to 20 Vp-p. The applied flow rate ranged from 5 to 20 μL min^{-1}. The particles had a uniform distribution at the inlet. Optical microscopy images showing the trajectories of particles along the whole channel (a) and the focusing patterns of particles at the outlet (b). (c) Measured focused positions and (d) focused widths from the fluorescent profiles. The average value of 3 times the measurement.

4.4.3. Movements of 10 μm particle

In order to investigate the ability of the device for simultaneously separating beads with different sizes, the particle trajectories of 10 μm beads were studied under the same conditions as 3 μm beads (Figure 4-4). The optical micrographs in Figure 4-4 a show

that the particles assumed a hydrophoretic ordering and focused themselves onto the sides of the channel under all conditions studied, which differs from the observations of the 3 μm beads. Since the DEP force on the particle is proportional to the cube of their diameter, the 10 μm beads experiencing higher DEP forces are levitated to a higher equilibrium position in the *z*-direction, and the interaction between particle and groove was relatively intensive and the steric effect occurred easily. Therefore, 10 μm beads can be focused quite well in the DEP-assisted hydrophoretic device under the same conditions applied to the 3 μm beads.

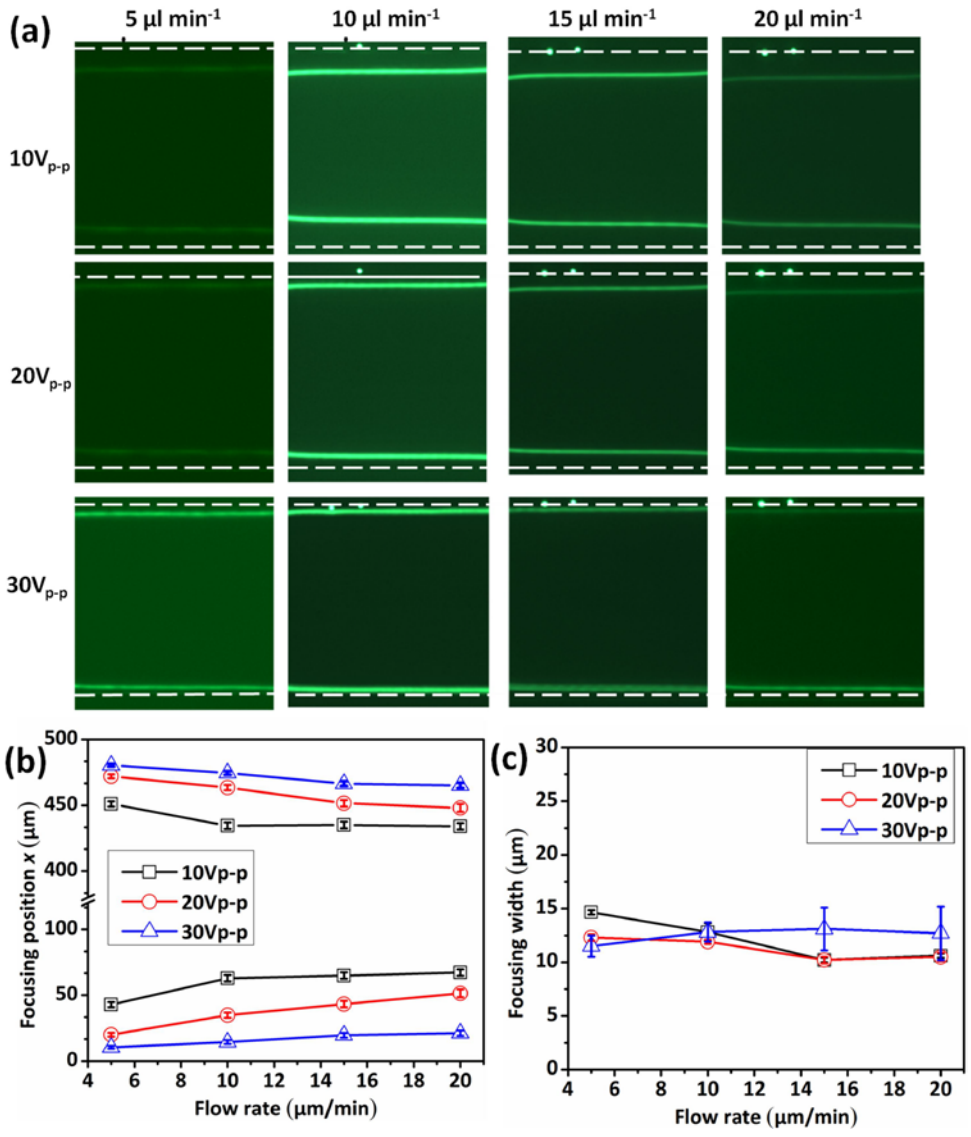

Figure 4-4 Focusing patterns of 10-μm particles. The applied voltage was changing from 10 to 20 Vp-p. The applied flow rate ranged from 5 to 20 μL min^{-1}. The particles had a uniform distribution at the inlet. (a) Optical microscopy images showing the

focusing patterns of particles in the microfluidic channel. (b) Measured focused positions and (c) focused widths from the fluorescent profiles. The average value of 3 times the measurement.

Figure 4-4 b and Figure 4-4 c show the focusing positions and widths of the 10 μm beads at different flow rates, respectively. The focusing positions changed as the flow rate increased in a similar way as those observed for the 3 μm beads. The beads were deflected from the sides of the channel by a higher transverse flow as the flow rate increased, and the beads tended to move closer to the sidewalls as the voltages increased. Choi and Park [27] had a similar result when they found that the lateral positions of the beads decreased when the height of the channel was lowered. Actually, applying a higher voltage can be the equivalent of lowering the height of the channel because the particles are pushed into a narrower space and can only migrate in the restricted area. Fig. 4c revealed that the focusing width of the 10 μm particles remained almost constant and was independent of the flow rate and voltage. The focusing width is very close to the diameter of the particles, indicating that their trajectories overlapped together and focused well. Because the particles were located in narrow ranges on the *z*-axis by the negative DEP forces induced by the interdigitated electrodes, they were exposed to the same flow pressure. This indicates they had a uniform lateral position and a minor change in their focusing width.

4.4.4. DEP-assisted hydrophoretic filtration of micro-particles

Filtration was first tested with 3 μm diameter (red) and 10 μm diameter (green) fluorescent particles whose sizes were comparable to the platelets, Red blood cells, and WBCs. Figure 4-5 a shows the trajectories of the 3 μm and 10 μm particles captured at a flow rate of 15 μl min^{-1} and a voltage of 20 V_{p-p}. The average linear velocity of particles flowing through the 500×45 μm channel is estimated to be 1.11 cm s^{-1}. Similar patterns were obtained from different particles, except for the focusing positions. The 3 μm and 10 μm particles migrated along the sidewalls of the channel and were finally collected at the waste outlet. As a result, the fluid through the collection channel contains no or only a few micro-particles. The current experiment showed that, after filtration, 99.4% of 3 μm beads and 99.8% of 10 μm beads were removed from initial particle-laden fluid solution (Figure 4-5 b). Although the 3 μm and 10 μm beads did not satisfy the

hydrophoretic ordering, focusing patterns were still observed under an external applied voltage, which generated negative DEP and pushed the particles into a narrow space in the *z*-axis. The large particles (10 μm diameter) and small particles (3 μm diameter) were focused simultaneously in the DEP-assisted hydrophoretic channel, which enabled small cells (platelets) and large cells (red blood cells and WBCs) to focus in our microfluidic device. Therefore, plasma can be extracted from the collection outlet.

Particles migrating through the micro-channels also experienced inertial lift forces such as the shear gradient and wall-induced lift forces under a high flow rate. The particle Reynolds number R_p is the ratio of particle inertia to the viscous force [32], i.e. $R_p = (\rho D^2 U)/(\mu D_h)$, where ρ represents the fluid density, D is the particle diameter, μ is the dynamic fluid viscosity and D_h is the hydraulic diameter defined as $D_h = 2WH/(W+H)$. For $R_p>1$, particle inertia was dominant and the equivalent paths of particles under hydrophoretic ordering were affected by inertial lift forces. The particle Reynolds numbers were 0.02 and 0.0018 for 10 μm and 3 μm beads at a flow rate of 15 μl min^{-1}, respectively. Therefore, the particle inertial effect can be neglected in our experiments.

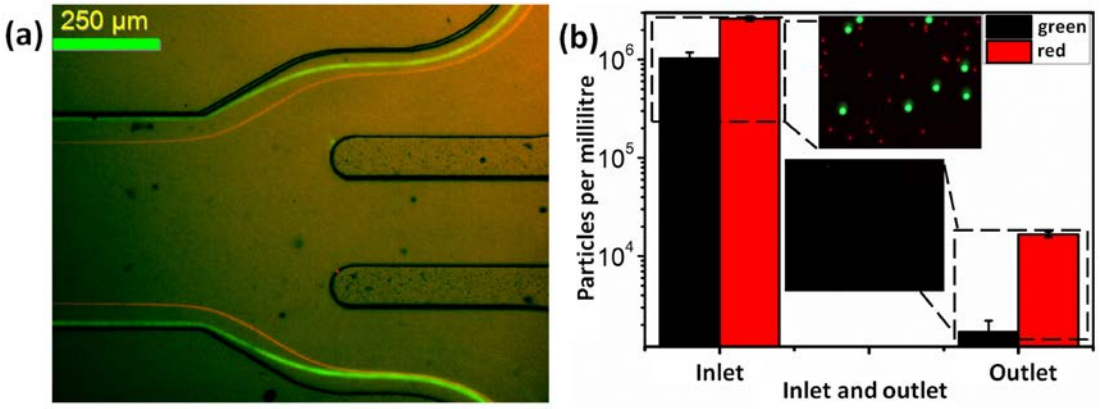

Figure 4-5 Filtration of 3 μm and 10 μm beads. The applied flow rate was 15 μl min^{-1} and external voltage was 20 Vp-p. The beads were evenly injected into the micro-channel. (a) Optical microscopy images showing the trajectories of 3 μm and 10 μm particles. (b) Particle concentration measured from both inlet and collection outlet. Insets illustrate the particles before and after filtration. The average value of 3 times the measurement.

4.4.5. Isolating plasma from diluted whole blood

The DEP-assisted hydrophoretic method was also used for isolating plasma from diluted whole blood. The flow rate applied for isolating plasma was 10 µl min^{-1} and the external voltage was 20 V_{p-p}. Choi et.al [4] found when the hematocrit of blood was higher than 1%, cell-cell interaction wouldn't be negligible. That is, blood cells will flow adjacent to each other and their cell-cell interaction may influence the focusing result of blood cells. Hence, the whole blood cells should be diluted to avoid the cell-cell interaction. Therefore, diluted blood (0.45% hct) is prepared to improve the focusing performance of blood cells. The optical micrographs in Figure 4-6 a show the focusing patterns of blood cells. Those blood cells which formed hydrophoretic ordering then focused into the sidewalls of the channel and were then collected from the waste outlet, while plasma was being extracted from the collection outlet. The blood cells had similar trajectories to the fluorescent particles, which show how effectively the biological cells were isolated in the DEP-assisted hydrophoretic channel. Although Red blood cells have a discoid shape and a diameter of 6.2-7.9 µm and a thickness of 1.7-2.6 µm [36], they formed hydrophoretic ordering and migrated along the sides of the channel because they had a hydrodynamic diameter of 7.7 µm [152]. When the diluted blood (0.45% hct) was injected into the channel, the blood cells were still focused onto the sidewalls of the microchannel and plasma was collected from the collection outlet. The throughput capability to process blood cells is 7,600 cells s^{-1}, which is higher than the conventional hydrophoretic techniques. The throughput of hydrophoretic sorter that was used to enrich WBCs from RBCs is 4,000 cells s^{-1} [36]. Figure 4-6 b and c show the blood cells before isolation (b) and after isolation (c). After DEP-assisted hydrophoretic isolation, the plasma reached a purity of up to 94.2 ± 3.6% (n=3) from the diluted whole blood. The yield of plasma extracted from diluted whole blood was 15.6 ± 2.5% (n=3).

Isolating plasma is clinically important because it may contain viruses and their biomarkers[34]. The blood cells (platelets, Red blood cells, and WBCs) should be removed in advance otherwise plasma containing contaminants may affect the final analytical result. The DEP-assisted hydrophoretic device is a tunable microfluidic system that may become a powerful tool to separate plasma from whole blood. It could potentially be a critical component in the advanced lab on a chip bioanalysis devices.

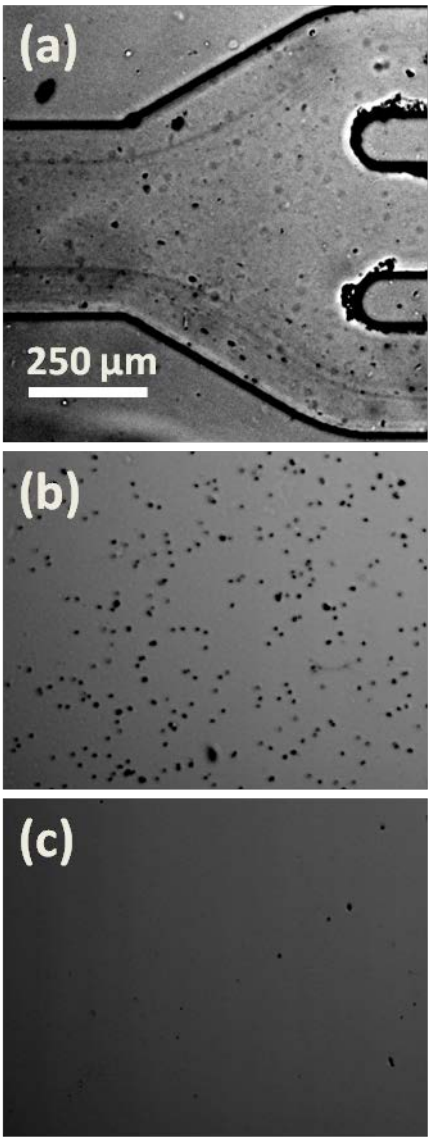

Figure 4-6 Isolation of plasma from diluted whole blood. The applied flow rate was 10 µl min^{-1} and external voltage was 20 Vp-p. The blood cells were evenly injected into the micro-channel. (a) Optical micrographs showing the trajectories of blood cells. Blood cells (b) before isolation and (c) after isolation are shown in bright-field images. These images were acquired with 40× magnification.

4.5. Conclusion

A DEP-assisted hydrophoretic device has been developed in this study. The device has been demonstrated to separate micro particles with different sizes and to extract plasma from diluted whole blood. The lateral positions of particles can be controlled by varying

external electric field. Not only did the large cells (red blood cells and WBCs) form a hydrophoretic ordering, the small cells (platelets) focused simultaneously in our microfluidic device. The high throughput was achieved by increasing the height of the channel (up to 90 μm) compared with the conventional hydrophoretic channel with the channel height less than twofold particle diameter. The size limit, i.e., the smallest diameter to be focused, was enlarged by exerting negative DEP force on particles in the *z*-axis generated by interdigitised electrodes. After filtration, 99.4% of 3 μm beads and 99.8% of 10 μm beads were removed from initial particle suspending. This technique offers a new method for filtrating blood cells from whole blood and extracting plasma with a purity of 94.2% and a yield of 16.5% in a high throughput manner. Moreover, this work solved the bottle-neck issue of low throughput of DEP based devices. The DEP-assisted hydrophoresis also provides a tunable microfluidic system that could potentially be used in advanced lab-on-a-chip bioanalysis devices.

5. A hybrid dielectrophoretic and hydrophoretic microchip for particle sorting using integrated pre-focusing and sorting steps[*]

5.1. Introduction

Microfluidic separating and sorting micron-sized particles have significant applications in clinical diagnostics, chemical, and biological analysis, and environment detection [99]. Microfluidic platforms have the potential to be miniaturized and have the advantages of portability, low cost and user-friendliness over the traditional instrument. Further, the use of microchip allows for the integration of multiple technologies into one device for manipulating and probing particles or cells and the mass production of microchips reduce the cost per analysis significantly.

Microfluidic techniques were divided into active and passive approaches. Active methods involve external field and generally a better performance can be achieved. For example, Li *et al.* [153] proposed a direct current (DC) dielectrophoretic separation channel that combined obstacle and curvature to generate the electric gradient. A mixture of 10 μm and 15μm particles was separately robustly with a separating efficiency of above 95%. Although DC dielectrophoresis (DEP) is a pumpless method to focus or separate particles, the high voltages involved in the experiment will generate Joule heating and may damage the cells. Han *et al*. [154] utilised a piecewise curved planar interdigitated electrode array to separate 3, 5, and 10 μm particles under AC electric field. This technique also demonstrated the capability to separate red blood cells and white blood cells in a highly conductive medium [155]. Adams and Soh [156] proposed an acoustic band-pass particle sorter to sort cells and particles according to the size. The tunable acoustophoretic separation was capable of sorting particles with diameter between 3 μm and 10 μm with high efficiency. Magnetophoresis is also an

[*] Results of this chapter are published in: (1) Sheng Yan, Jun Zhang, Yuan Yuan, George Lovrecz, Gursel Alici, Haiping Du, Yonggang Zhu, Weihua Li, A hybrid dielectrophoretic and hydrophoretic microchip for particle sorting using integrated prefocusing and sorting steps. ***Electrophoresis***, 36, 284-291, 2015; and (2) Sheng Yan, Jun Zhang, Chao Pan, Dan Yuan, Gursel Alici, Haiping Du, Yonggang Zhu, Weihua Li, An integrated dielectrophoresis-active hydrophoretic microchip for continuous particle filtration and separation. ***Journal of Micromechanics and Microengineering,*** 25, 084010, 2015.

effective way to separate magnetic and nonmagnetic particles using magnetic field [157]. Although magnetically labeled cells can be separated from human blood [158], it is impractical to supply paramagnetic cells as most of the cells are nonmagnetic. However, these active methods suffer from low sample throughput.

Unlike active methods, passive methods utilize intrinsic hydrodynamic phenomena, which make it difficult to generate field gradient to drive particles from one side of the channel to the other one. Therefore, special channel structures and sheath flows were introduced to confine particles into a specific position. Yamada *et al*. [103] used pinched flow fractionation to continuously separate particles with different size. In particular, the fractionation quality is highly dependent on the width of the the pinched region and an accurate flow control between sheath and sample flows. Deterministic lateral displacement was first proposed and demonstrated by Huang et al. [45] to separate sub-micron particles with high resolution. This method was then employed to separate blood cells and isolate plasma from blood [33]. However, micro-pillars within a micro-channel bring the risk of clogging. Inertial microfluidics is a high-throughput technique to sort particles without external physical field [64, 147, 159]. There still exists a challenge for sorting cells because high shear stress on the cells may make them non-viable by damaging cell wall or membrane[35]. Typically, mammalian cells are very shear sensitive. Hydrophoresis is a sheathless approach that utilized slanted grooves to induce pressure gradient to push particles from one sidewall of a channel to another one [160]. Hydrophoretic filtration was proposed and demonstrated to separate particles and cells with a high separation efficiency [36]. This hydrophoretic channel consisted of the thick region for focusing and thin region for filtration. In the filtration stage, small particles went through the filtration gaps, while large particles were pushed to pass through the filtration pores. This technique was still in the risk of blockage because the maximum height in the filtration segment is 8 μm through which the white blood cells with a diameter larger than 8 μm were not able to pass. Additionally, different thickness existing simultaneously in a channel requires complex fabrication processes. Also, channel height is a key parameter for the hydrophoretic separation, which determines the operational range of particles to be separated. To get satisfied experimental results, standard photolithography is normally required to repeat several times to get the specific thickness of the SU-8 mold.

DEP and hydrophoresis exist different advantages. Hydrophoresis has been verified to be a versatile tool for size-based separation, while DEP forces can, by modulating amplitude and frequency, be tuned to manipulate particles according to the physical characteristics such as volume and dielectric property. Tunability could be used in a real-time feedback system, where for example the running parameters are adjusted according to the evaluation of separation performance in order to reach the expected outcomes. Combining DEP with hydrophoresis thus benefits the best from the two methods. The concept of DEP-assisted hydrophoresis was reported previously by our group [47]. This tunable device relaxed the strict prerequisite of designing and fabricating devices with accurate heights for a given sample. Based on focusing simultaneously small and large cells in the micro-channel, this technique was then employed to isolate plasma from human blood [112]. Even though different particles had different distributions in the previous channel, particle trajectories were such close that we could not collect them from our microfluidic device.

The main objective of the current study is to develop an integrated microfluidic device composed of pre-focusing and sorting region for particle separation. In this work, the application of our DEP-assisted hydrophoresis has extended from simply focusing particles or cells to separating binary mixtures with high separation efficiency. The brief outline of the paper is as follows. Section 5.2 will introduce material and methods including design and analysis, modelling, materials and experimental setup. The main results will be presented in Section 5.3 which include particle sorting based on their sizes, an application example of viable Chinese Hamster Ovary (CHO) cell sorting according to their dielectric property, and a dual-mode DEP-assisted hydrophoresis. The main conclusion will be drawn in Section 5.4.

5.2. Materials and methods

5.2.1. Design and analysis

The mechanism of hydrophoresis is studied both numerically and experimentally. The critical diameter to be ordered and focused in the channel has been defined as half the height of the channel [35, 135], while the grooves patterned on top of the channel induce anisotropic fluidic resistance which generates rotational flow [161]. However,

this particle-groove interaction diffused the large particles out of their streamlines because their diameters exceeded the critical diameter and lead to equivalent flow paths; this is called hydrophoretic ordering [32].

The DEP-assisted hydrophoretic sorter consists of pre-focusing region and sorting region (Figure 5-1). In the pre-focusing region, interdigitated electrodes were patterned onto the bottom of the channel so that particles exerting a negative DEP force were pushed into a narrow space (left inset of Figure 5-1). As a result, the particles have more opportunity to interact with the grooves and induce hydrophoretic ordering by steric hindrance. Hence, large and small particles can focus simultaneously in our DEP-assisted hydrophoretic device under an appropriate flow rate and applied voltage even though their diameters are less than the critical diameter. However, those particles with different diameters were not separated because their trajectories were too close to each other, so the sorting region was introduced to separation particles. The sorting region has two functions. First of all, the sorting region had a larger width than that of pre-focusing region, which was used to expand the relative distance between the different particles. Because the flow profile at the junction of the pre-focusing and sorting region spread, the slight difference in the positions of the particles in the pre-focusing region can be amplified quite substantially in the sorting region (right inset of Figure 5-1). Secondly, the separation grooves having the reverse direction as pre-focusing grooves were patterned on the sorting region, starting from the middle of two particles trajectories to left sidewall. In this way, small particles are forced to push towards left sidewall following the fluid field induced by sorting grooves, while large particles still remain its previous position migrating along right sidewall (Figure 5-1). This means that particles can be separated completely and collected easily using the DEP-assisted hydrophoretic channel. Moreover, both pre-focusing and sorting region have the same height, which therefore reduces the complexity of fabricating devices.

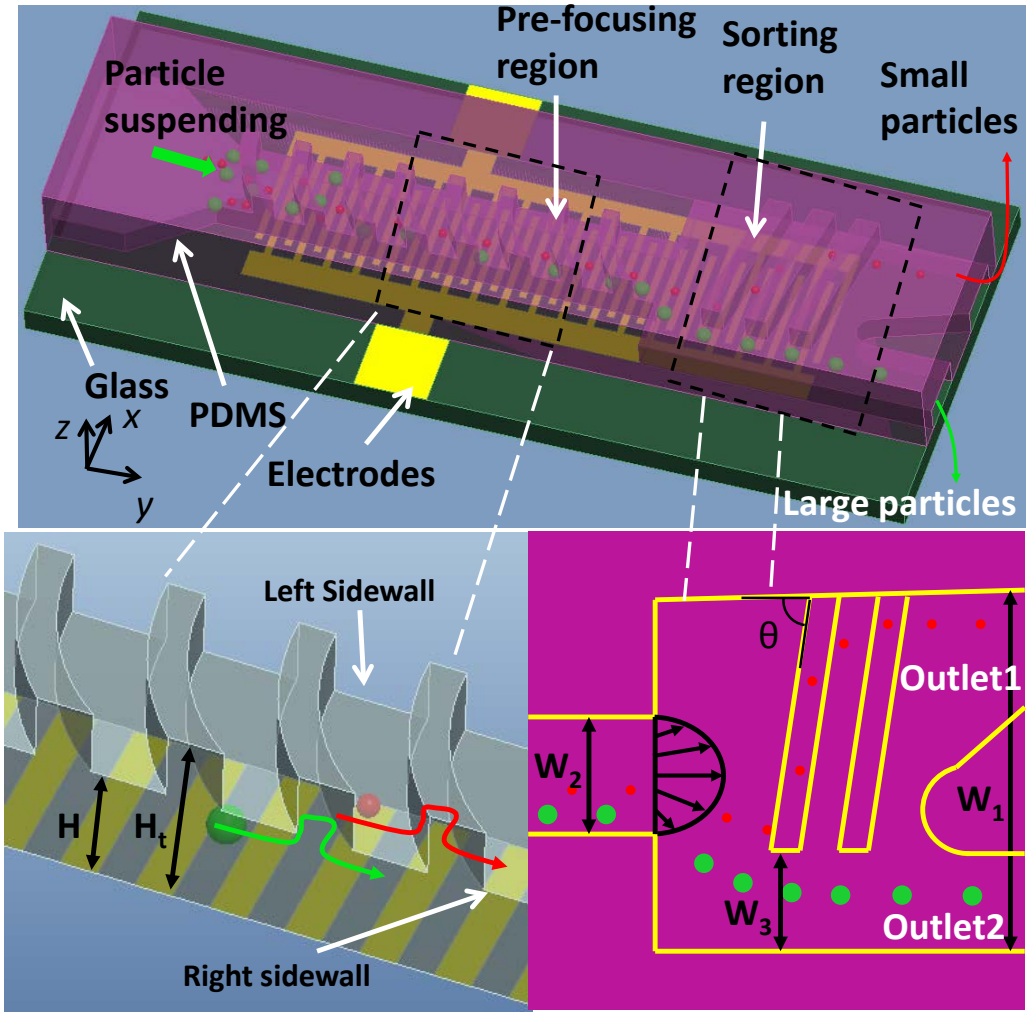

Figure 5-1 Overview of DEP-assisted hydrophoretic sorter. The device consists of pre-focusing and sorting region. The left inset shows large and small particles can be focused onto the sidewall by a steric hindrance mechanism under a certain external electric field in the pre-focusing region. Sorting region with grooves is involved to lead small particles to left sidewall by transverse flow, while large particles keep their positions along the right sidewall (right inset).

The spacing and the width of the electrodes were both 20 μm. The pre-focusing region consisted of a series of grooves with a small curvature of 600 μm and a large curvature of 650 μm (Figure 5-2 b). The separation grooves were 50 μm in both width and spacing with θ = 80°. The height of the micro-channel for the two regions was H_t = 70 μm and H = 35 μm, respectively. The width of the sorting region W_1 was 800 μm, while the width of the pre-focusing region W_2 was 200 μm wide and its length was L=10 mm.

The gap between the tip of the separation grooves and right sidewall of the channel W_3 was 150 μm.

5.2.2. Modelling

In order to better understand the DEP-assisted hydrophoretic mechanism, a commercial multiphysics modeling software package COMSOL was used to calculate the particle trajectories and velocity vectors (Figure 5-2). The modeling details for this simulation can be found in section 4.3 [112]. In the current modeling, the particles were assumed to be injected into the channel at a flow rate of 4 μl min^{-1}. Figure 5-2 a shows the movements of particles in the pre-focusing region and the sorting region. The velocity vectors around the grooves were investigated (Figure 5-2 b).

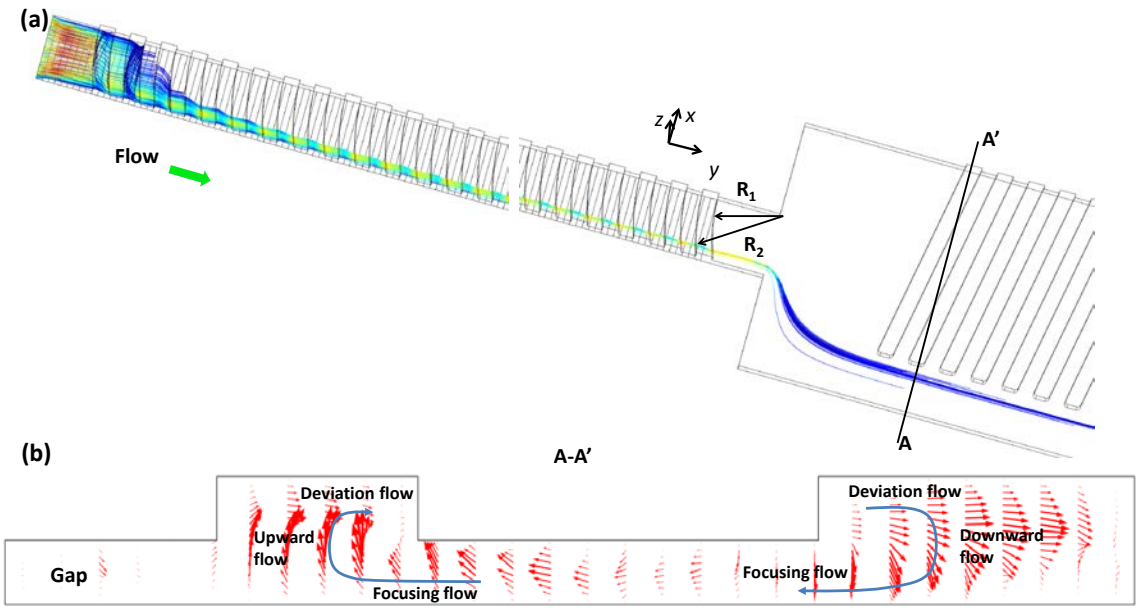

Figure 5-2 (a) Simulated particle trajectories in two sections of the micro-channel. The left image shows the entrance section of the micro-channel and right the exit section. The steric effect makes the particles diffuse out of convective vortices and assume hydrophoretic ordering. The colour of the trajectories denotes particle velocity. Red means high speed and blue means low speed. The flow direction is along the *y*-axis. (b) The calculated results of the flow field in the cross section along the line, A-A'. The anisotropic microstructure induces helical recirculation that consists of an upward, deviation, downward, and focusing flow. The red arrows represent the velocity vector.

In the pre-focusing region, a secondary flow was generated because the anisotropic microstructure patterned on the channel forced the fluid to rotate in the cross section in a sequence of focusing, upward flows, deviation flow, and downward flow. When the particles were injected into the channel, they gradually levitated due to the negative DEP force induced by electrodes embedded at the bottom of the channel. The particles were mainly exposed to deviations in the flow at the higher levels of the channel and then driven to right sidewall. The movement of particles was also determined by a mechanism called steric hindrance [162] which occurred when the particles collided with the grooves. Steric hindrance diffused the particles out of the rotational stream such that they were eventually focused and moved along the right sidewall. Particles will flow into the sorting region following the spreading flow profile. The focusing width of particle trajectories would be wider in the sorting region because their sudden expansion can amplify the slight difference in the positions of the particles. However, particles have been pre-focused in the pre-focusing region, so they can still be focused quite well in the sorting region. Since no transverse flow existed in the gap between the right sidewall and grooves in the sorting region, particles can keep their lateral positions without the influence of rotational flow.

5.2.3. Microfabrication

To experimentally investigate the sorting behavior, a hybrid device was fabricated using a two-step photolithography technique. Detailed information for this fabrication technique can be found in our previous work [112, 137, 150]. Here a brief introduction is given. The first layer of photoresist (SU-8 2025, MicroChem Co., Newton, MA) was spun on the silicon wafer. After exposure and baking, the second layer with the pattern of grooves was fabricated using the same procedure and the pattern was aligned with the structures in the first layer. After the double-layer mold was developed, it was then treated by trichlorosilane to deposit a mono-layer of silane on the surface for the ease of PDMS release.

5.2.4. Material preparation

Fluorescent micro-particles with diameters of 3, 5, 10 μm (Thermo Fisher Scientific., product number R0300, G0500, G1000 and coefficient of variation 5%, 5%, and 5%,

separately) were used in our experiments. They were prepared in deionized (DI) water, with 0.1% Tween 20 (Sigma-Aldrich, Product No. P9416) added to this particle suspension to stop the beads from sedimentation. The final concentration of beads was in the order of 10^5 beads per millilitre.

CHO cells were cultured in-house in CSIRO Tissue Culture Facility at Manufacturing Flagship, Clayton, Melbourne, Australia. The CHO cells were washed and resuspended in low electrical conductivity buffer (LEC, 8.5% w/v sucrose and 0.3% w/v dextrose) to yield a cell concentration of 1.8×10^6 cells ml^{-1}. The original suspension with 18% nonviable and 82% viable cells was measured using 2% (w/v) trypan blue (Invitrogen). The electrical conductivity of LEC was modulated by adding appropriate amounts of phosphate buffer solution (PBS, Sigma-Aldrich). The average radius of viable and nonviable CHO cells were 6.5 and 5.53 μm, respectively [163].

5.2.5. Experimental setup

The particle experiments were conducted in the microfluidic laboratories at the school of Mechanical, Materials and Mechatronic Engineering, University of Wollongong. More details can be found in a previous publication [112].

The cell experiments were carried out in the Microfluidic Laboratory at CSIRO Manufacturing Flagship, Clayton VIC 3169, Australia. An inverted Nikon microscope (Eclipse TE2000-U) was utilised to image the movements of CHO cells. One side port of the microscope was linked to a high-speed camera (MotionPro X3, Redlake). A neMESYS pump system (Cetoni, Germany) was used to inject the cell samples into the microfluidic channel. AC fields with a frequency of 30 kHz for cell experiments were generated by a waveform generator (33250A, Agilent, USA)

5.3. Results and discussion

5.3.1. Effect of voltage on particle trajectories

To optimize the sorting performance, the voltage-dependent particle trajectories were first investigated (Figure 5-3). The applied flow rate was 4 μl min^{-1} and the external voltage was adjusted from 21 to 33 $V_{p\text{-}p}$. 3 μm beads were evenly distributed at the inlet

and focused well in the pre-focusing region at the voltage of 30 V_{p-p}. After entering the sorting region, particles were deflected to left sidewall due to rotational flow induced by grooves as shown in Figure 5-3 a. Though 3 μm beads were not focused well at relatively low voltage (i.e. 21 and 24 V_{p-p}), they could still be driven to left sidewall by the grooves in the sorting region. With the increase of voltages, a small portion of 3 μm beads were able to be deflected at the first groove and moved along the left sidewall. The main reason is that particles were pushed higher in the micro-channel where the particle-groove interaction was intensive to induce hydrophoretic ordering. Since the 10 μm beads moved very close to the right sidewall, a significant amplification was observed to separate the 10 μm particle trajectories into the two branches at the junction of the pre-focusing and sorting region. At the voltage of 30 V_{p-p}, all 10 μm particles could pass through the gap between grooves and a right sidewall. However, the 10 μm particles unable to successfully pass through the gap at relatively low voltage. At such circumstances, they were driven to left sidewall by the grooves. At 27 V_{p-p}, particles could pass through the gap at the beginning. At a later stage, once they touched the grooves, the grooves would lead them to left sidewall.

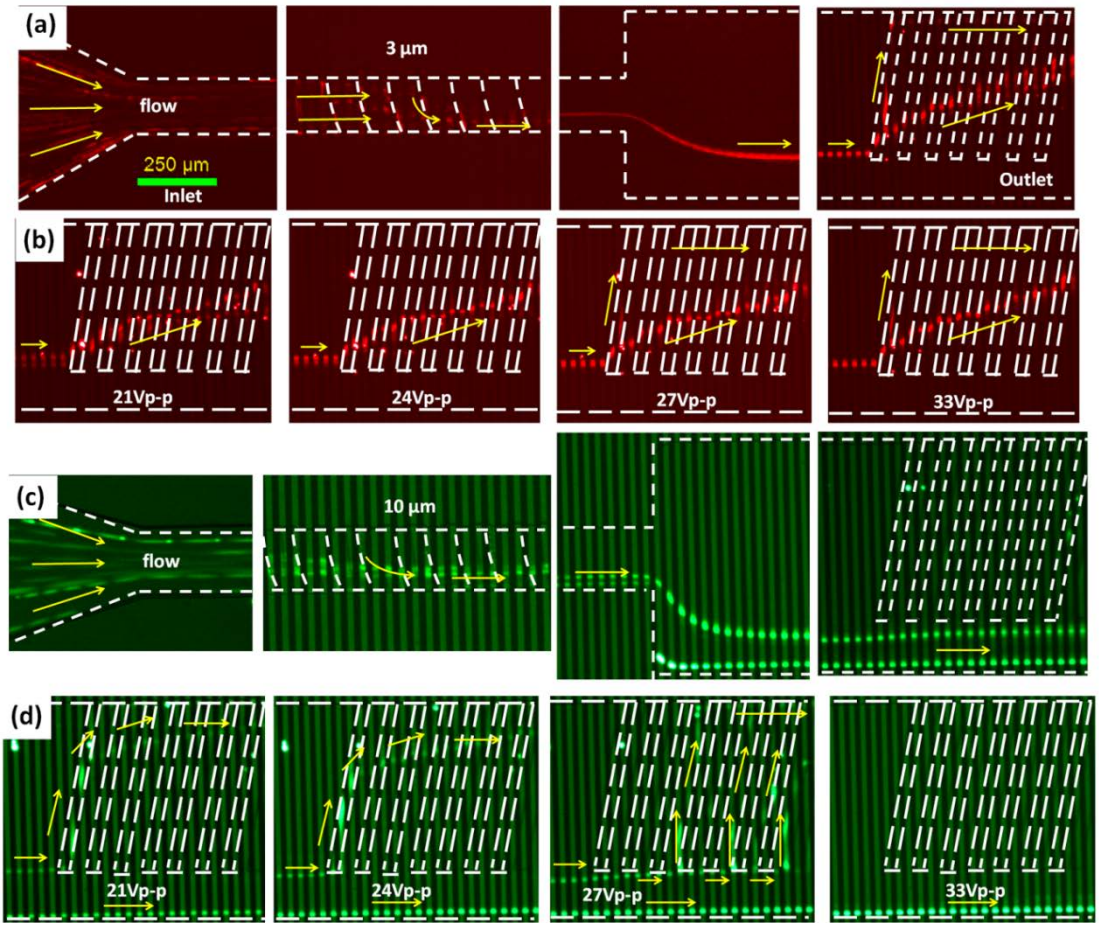

Figure 5-3 (a) and (c) Optical micrograph showing the trajectories of 3 and 10 µm beads in the whole channel. The applied voltage was 30 Vp-p and the applied flow rate was 4 µL min^{-1}. (b) and (d) Fluorescence images showing the trajectories of 3and 10 µm beads in the sorting region with voltages of 21, 24, 27, 33 Vp-p, separately.

5.3.2. Size-based DEP-assisted hydrophoretic sorting

After studying the particle trajectories of 3 and 10 µm micro-particles in the integrated pre-focusing and sorting channel, the DEP-assisted hydrophoretic sorting was investigated and the results are shown in Figure 5-4. The particle mixture was introduced into the microfluidic device with a flow rate of 2 µl min^{-1} and a voltage of 30 V_{p-p}. The original concentration of bead mixture was ~4×10^5 particles ml^{-1} and the initial concentration ratio of 3 µm particles to 10 µm particles was 2:1. As shown in Figure 5-4 a, the two size particles were completely separated. To quantify the separation performance, particle purity (collected target particle number/collected total number [164]) and separation efficiency (collected target particle number/input target

particle number [165]) were measured. After sorting, the 10 μm beads were collected from Outlet 2 with a separation efficiency of 96.6 ± 0.4% and a purity of 93.4 ± 1.0%, whereas for the 3 μm particles, a separation efficiency of 95.7 ± 0.7 % and a purity of 97.8 ± 0.3% were recovered from Outlet 1.

Particle-particle interaction and non-specific agglomeration of particles tend to influence the separation purity. Therefore, a microfluidic separation technique typically needs multiple rounds of separation to achieve high purity [166]. However, for the current DEP-assisted hydrophoretic separation, the separation purity of >90% was successfully achieved in a single round of separation. The main reason was that the 3 and 10 μm beads were separated completely when entering the sorting region and the 3 μm beads were then driven to left sidewall of the channel by the separation grooves. Their crossing did not disturb the focusing position of the 10 μm beads.

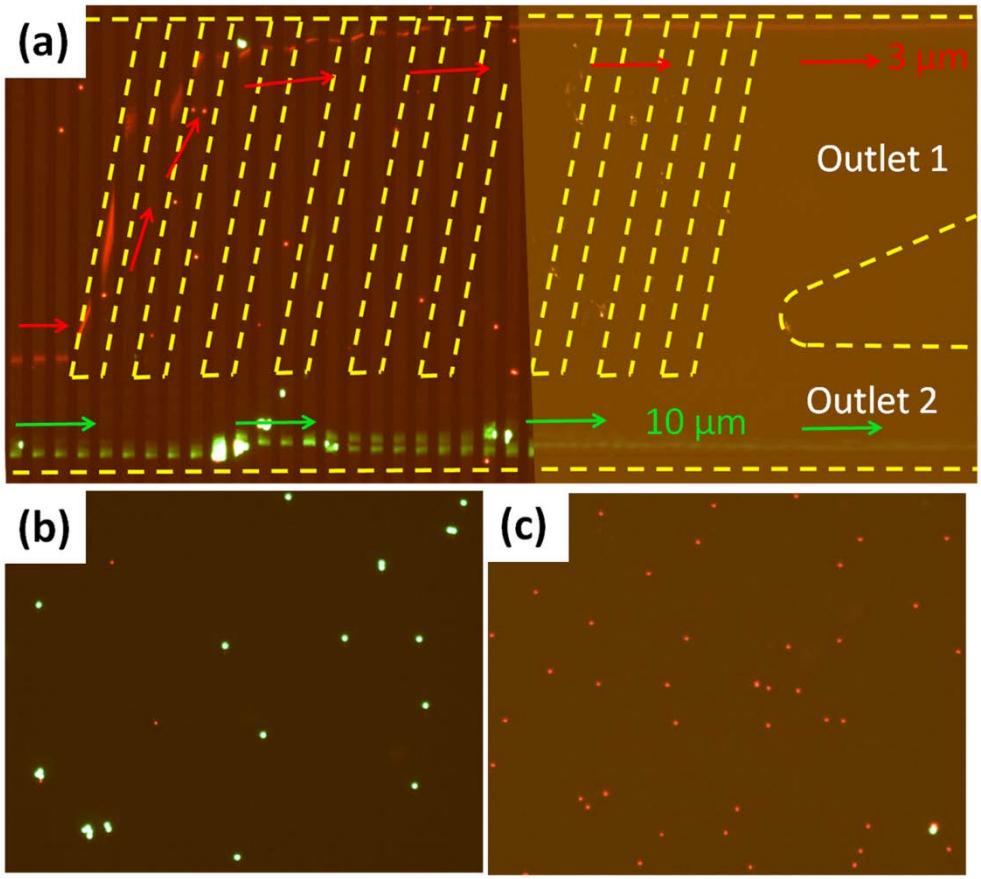

Figure 5-4 (a) Optical micrograph showing the trajectories of 3 and 10 μm beads after entering the sorting region. The applied voltage was 30 Vp-p and the applied flow rate

was 2 μL min^{-1}. Beads collected from outlet 2 (b) and outlet 1 (c) were shown in fluorescence images. These images were captured with 50× magnification.

5.3.3. DEP-assisted hydrophoretic sorting based on dielectric property

The DEP-assisted hydrophoresis can not only take advantage of hydrophoresis that separates particles according to their sizes, but also dielectrophoresis that can sort cells based on their complex permittivity. This is demonstrated by the separation of CHO cells. The viable CHO cells exerting strong negative DEP force can be pushed to the higher level where particles interact with grooves to form hydrophoretic ordering. The viable cells can be focused well in the pre-focusing region and keep migrating along the right sidewall of the sorting region. Finally, viable cells were sorted from cell sample and collected from Outlet 2 (red arrows in Figure 5-5 a). On the contrary, nonviable CHO cells experiencing weak negative DEP cannot induce hydrophoretic ordering. They travelled back and forth within groove area after entering the sorting region due to the rotational flow induced by grooves patterned on the top of the channel. Therefore, nonviable CHO cells flowed to Outlet 1 (indicated by the green arrows in Figure 5-5 a).

According to Eq. 3-1, the Clausius-Mossotti (CM) factor f_{CM} depends on the complex permittivity of the cells and the suspending medium, and the frequency of the external electric field. Considering that CHO cells have a complex structure of cytoplasm, membrane, and nuclear envelope, the spherical multishell model was utilised to measure the Re[f_{CM}] [44]. The geometrical and dielectric properties of both viable and nonviable CHO cells were given by Brassch *et al*. [163]. Figure 5-5 b showed the Re[f_{CM}] spectra of viable and nonviable CHO cells at the medium conductivity ranging from 0.001 to 0.1 S/m. Positive DEP response for both viable and non-viable CHO cells exists at the medium conductivity of 0.001 S/m. Alternatively, at $0.01 \leq \sigma_{medium} \leq 0.1$ S/m, the viable cells exhibit a negative DEP at low frequencies, while the nonviable CHO cells exist a negative DEP response at low frequencies at the conductivity from 0.03 to 0.1 S/m. It should be mentioned that Re[f_{CM}] of viable and nonviable CHO cells are -0.46 and -0.19, respectively, at the medium conductivity of 0.03S/m and low frequencies. Even though a negative DEP effect was observed, the DEP force of viable cells was 2.4 times larger than that of nonviable cells, which provided a circumstance that viable cells were pushed high enough to form hydrophoretic ordering while nonviable cells were not.

In order to keep the viability of CHO cells, high voltages were avoided and the external voltage was 20 V_{p-p}. Since the cells were transparent, the applied flow rate decreased to 0.2 µl min^{-1} for better observation. The initial concentration of CHO cells was ~ 1.8 × 10^6 cell ml^{-1} and viable cells occupied 82% of the total cells. By the sorting process, the viable CHO cells were sorted and collected from outlet 2 with a purity of 99.6 ± 0.2 %. Nonviable CHO cells were isolated from Outlet 1 with a purity of 42.4 ± 1.3%. Up to 98.6 ± 0.6% of nonviable cells were recovered from their original concentration. Only large and viable can pass through the gap between grooves and right sidewall in the sorting region, hence, highly pure viable cells were obtained from Outlet 2. It should be mentioned that the culture collected from Outlet 2 had higher viability, which was more suitable for further culturing or experimenting purposes. As for Outlet 1, although nonviable cells were separated with high separation efficiency, the separation purity was low. The main reason was that small and viable cells could not reach the gap and were driven to another side of the channel (left sidewall). After sorting, cell samples from inlet and outlets were mixed with 2% (w/v) trypan blue to identify their viability (Figure 5-5 c).

Conventional dielectrophoretic separation of viable and nonviable cells was based on the dielectric property. Typically, the live cells were trapped via positive DEP while the dead cells could pass through the trapping area. The live cells were then washed by the buffer flow after releasing the electric field [167, 168]. However, the main drawback of this technique was discontinuity. DEP-field-flow fractionation (FFF) was utilised to separate viable and nonviable CHO cells according to a different time to reach the channel outlet. Therefore, longer channel and process time were required for DEP-FFF experiments. Continuous separation based on the dielectric property was achieved in our DEP-assisted hydrophoretic channel, which improved the size-dependent hydrophoretic separation. The DEP-assisted hydrophoretic device is a tunable system that may become a versatile tool to separate particles or biological cells based on their volume and dielectric property.

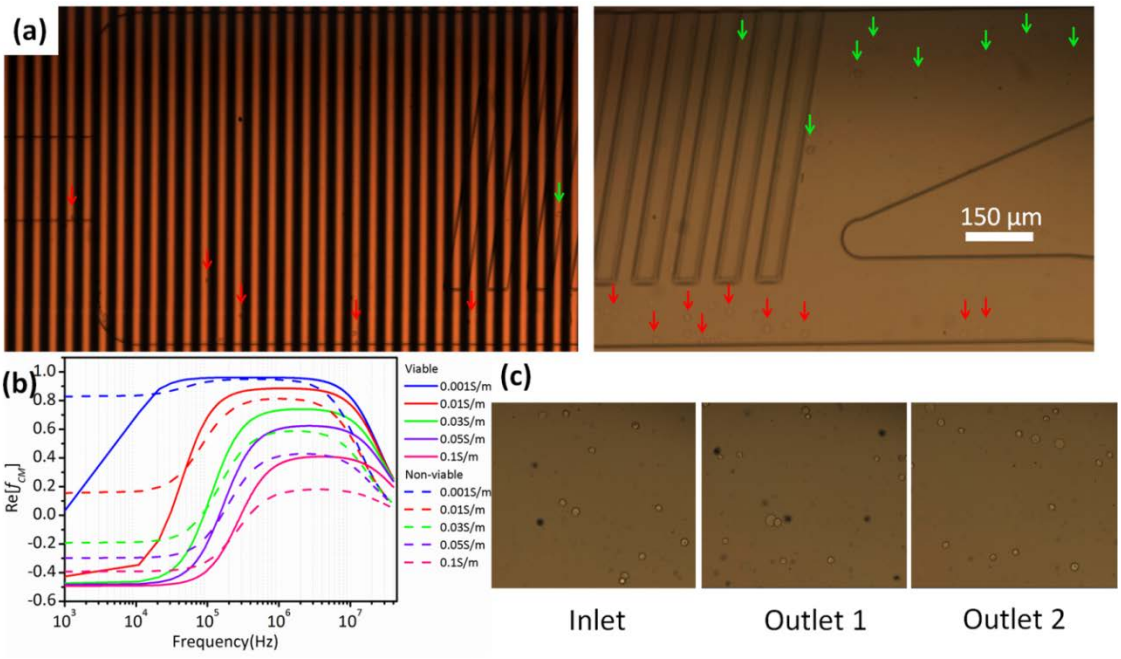

Figure 5-5 (a) Optical micrograph showing the trajectories of CHO cells after entering the sorting region. The red arrows represented the viable CHO cells, while green arrows denote nonviable CHO cells. (b) The Re[f_{CM}] spectra of viable and nonviable CHO cells at the medium conductivity ranging from 0.001 to 0.1 S/m. (c) cell samples from inlet and outlets dyed with 2% (w/v) trypan blue were shown in bright-field images. These images were captured with 200× magnification.

5.3.4. Dual mode of DEP-assisted hydrophoresis for particle filtration and separation

By modifying the structures in the sorting region, a dual function (*i.e.* filtration and separation) can be achieved in a single chip. The reverse grooves in the sorting region were replaced by an array of microposts. Once entering the latter section of the channel, the large particles with 10 μm in diameter will go through the gap between micro-posts and the right sidewall at the relatively high voltage (36 $V_{p\text{-}p}$), whereas they will not at the relatively low voltage (24 $V_{p\text{-}p}$). For 3 μm beads, they are unable to pass through the gap under any voltage applied in this experiment. Therefore, there are two different working modes based on different voltages. The first mode, called filtration mode, is that both 3 μm and 10 μm particles cannot pass through the gap under the low voltage and therefore purified water can be collected from the Outlet 2 (Figure 5-6a). In another

mode named separation mode, 3 μm and 10 μm particles can be separated by the microposts embedded in the micro-channel at the high voltage. Finally, 3 μm and 10 μm particles are collected from the different outlets (Figure 5-6b). The series of microposts serve as pressure shunts to balance the pressure between Outlet 1 and Outlet 2. Additionally, 10 μm particles are larger than the minimum space between neighbouring microposts (8 μm), indicating that large particles will not pass the microposts, which improves the separation efficiency.

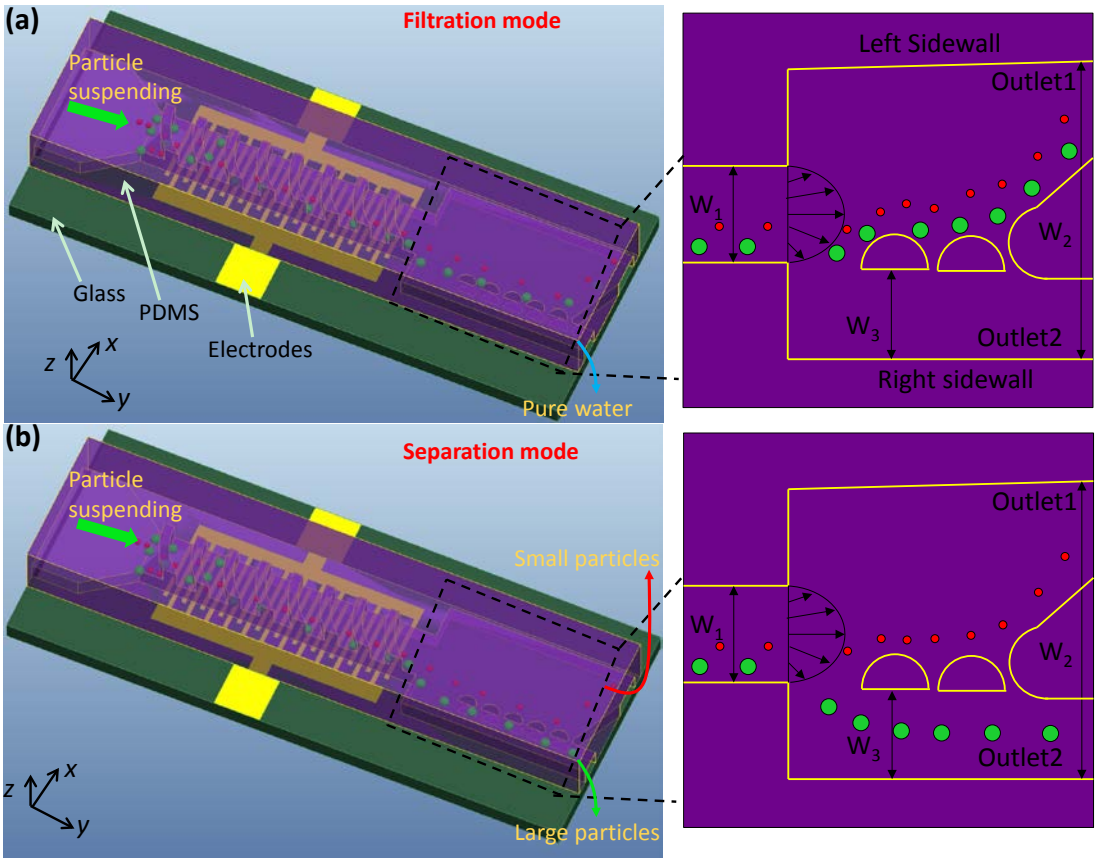

Figure 5-6 (a) The schematic of a DEP-assisted hydrophoretic device for particle filtration. Both large and small particles can be focused onto the sidewall by steric hindrance mechanism under a certain external electric field in the front section of the channel. All beads cannot pass through the gap between micro-posts and right sidewall under the low voltage and therefore purified water can be collected from the Outlet 2 (right inset). (b) An overview of the DEP-assisted hydrophoretic device for particle separation. Small and large particles can be separated by the microposts embedded in

the micro-channel at the high voltage. 3 µm and 10 µm particles are collected from the different outlets (right inset).

Filtration was conducted with 3 µm diameter (red) and 10 µm diameter (green) fluorescent particles. The mixture of 3 µm and 10 µm particles was introduced into the micro-channel with a voltage of 24 V_{p-p}. Similar patterns were obtained from different particles, except for the focusing positions. 3 µm and 10 µm particles could not pass through the gap between micro-posts and right sidewall and were collected from Outlet 1 (Figure 5-7a). As a result, the fluid through the Outlet 2 contains very little micro-particles. Figure 5-7b and c show the fluorescent images of beads collected from inlet and Outlet 2. The current experiment showed that, after filtration, 99.0% ±0.3% (n=3) of 3 µm beads and 100% (n=3) of 10 µm beads were filtered from the initial particle-laden fluid solution.

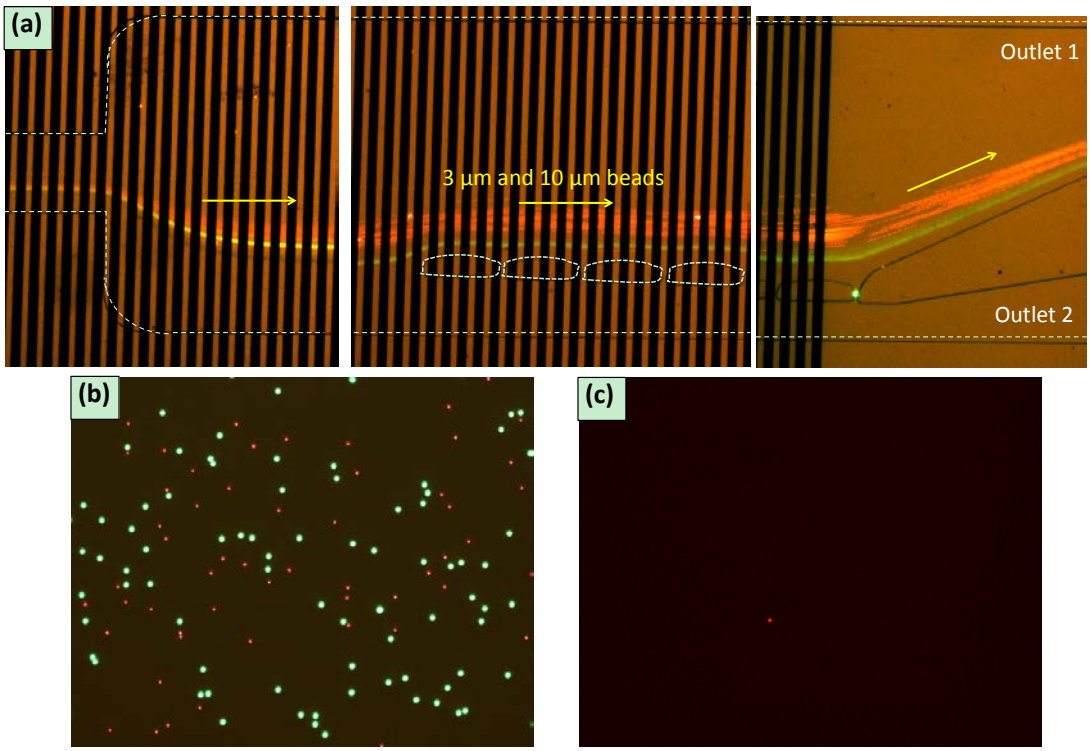

Figure 5-7 Filtration of 3 µm and 10 µm beads. The applied flow rate was 5 µl min^{-1} and external voltage was 24 Vp-p. The beads were evenly injected into the micro-channel. (a) Optical microscopy images showing the trajectories of 3 µm and 10 µm particles. The particles before (b) and after (c) filtration were illustrated in fluorescent images. These images were capture with 50× magnification.

With the increase of voltages, 10 μm beads pass through the gap between the microposts and right sidewall of the channel whereas 3 μm beads cannot. As a result, a fluid containing 3 μm beads was collected from Outlet 1, while 10 μm beads go through the Outlet 2. The separation experiment was conducted at a voltage of 36 V_{p-p} and the results are shown in Figure 5-8 a, b and c. As shown in Figure 5-8a, the two size particles were completely separated. To quantify the separation performance, particle purity (collected target particle number/collected total number [164]) and separation efficiency (collected target particle number/input target particle number [165]) were measured. Figure 5-8b and c show the fluorescent images of beads collected from Outlet 1 and Outlet 2, respectively. After sorting, the 10 μm beads were collected from Outlet 2 with a separation efficiency of 100% and a purity of 98.6 ± 0.8%, whereas for the 3 μm particles, a separation efficiency of 99.4 ± 0.2 % and a purity of 100% were recovered from Outlet 1. To demonstrate the capability of our device that can separate other particle sizes, a mixture of 5 and 10 μm particles was introduced into the microchannel at a voltage of 39 V_{p-p} (Figure 5-8d). Figure 5-8e and f show the separated beads collected from Outlet 1 and Outlet 2, respectively. By the separation process, 5 μm particles were separated at the Outlet 1 with a purity of 96.6% ± 1.2%. The separation efficiency for 5 μm was 98.5 ± 0.5%. A particle population was collected from the Outlet 2 that held 90.9 ± 2.3% 10 μm particles. Up to 86.2 ± 3.0% of 10 μm particles were separated from their initial particle suspending.

High separation performance was achieved because polystyrene particles with different size were pre-separated when entering the latter section of the channel. Then, the microposts served as a re-purifying unit to remove the unseparated small particles from Outlet 2 [169]. Due to the special design, the hydrodynamic resistance of Outlet 1 is higher than that of Outlet 2. To balance the pressure between Outlet 1 and Outlet 2, a small amount of liquid was withdrawn from Outlet 2 to Outlet 1 through the spaces between microposts, which brought a small amount of the unseparated small particles into the Outlet 1. Therefore, the particles were separated with high separation efficiency and purity.

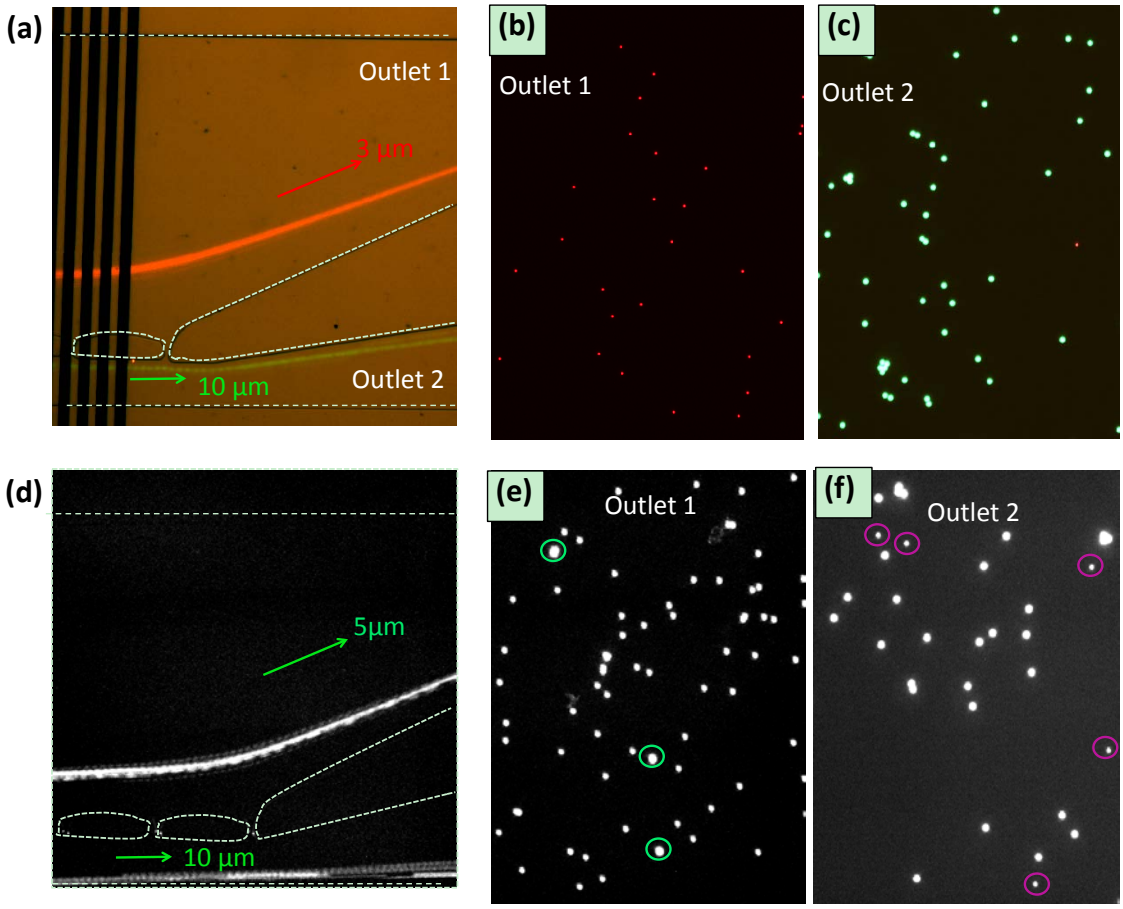

Figure 5-8 (a) Separation of 3 µm and 10 µm beads. The applied flow rate was 5 µl min^{-1} and external voltage was 36 Vp-p. The beads were evenly injected into the micro-channel. Optical micrographs showing the trajectories of 3 and 10 µm beads after entering the latter section. Beads collected from outlet 1 (b) and outlet 2 (c) were shown in fluorescence images. (d) Micro-image showing the separation of 5 µm and 10 µm beads. The applied flow rate was 5 µl min^{-1} and external voltage was 39 Vp-p. Beads collected from outlet 1 (e) and outlet 2 (f) were shown in fluorescence images. These images were capture with 50× magnification.

5.4. Conclusion

A new microfluidic DEP-assisted hydrophoretic sorter was proposed in this study for particle sorting. The device consists of pre-focusing and sorting regions. A mixture of 3 and 10 μm polystyrene particles and CHO cells are used to test the performance of these devices. The small particles were driven by the separation grooves to left sidewall, while the large particles could pass through the gap between separation grooves and right sidewall. After separation, the 10 μm beads were collected from Outlet 2 with a separation efficiency of 96.6 ± 0.4% and a purity of 93.4 ± 1.0%, while 95.7 ± 0.7 % of 3 μm particles were recovered from Outlet 1 with a purity of 97.8 ± 0.3%. The combination of DEP and hydrophoresis provides a sorting method based not only on size but also on complex permittivity of the particles or cells of interest without any labelling. According to the different Re[f_{CM}] of live and dead CHO cells at the medium conductivity of 0.03 S/m, the viable CHO cells were focused well and passed along the right sidewall. 99.6 ± 0.2 % viable CHO cells were sorted from cell sample and collected from outlet 2. It should be possible to sort particles of equal volume according to the difference in Re[f_{CM}]. Further, with a change in sorting section, two modes, *i.e.*, filtration and separation modes, were achieved in a single chip and can be switched by changing the voltages. In filtration mode, 99.0% ±0.3% of 3 μm beads and 100% of 10 μm beads were filtered from the initial particle-laden fluid solution. In separation mode, the 10 μm beads were collected from Outlet 2 with a separation efficiency of 100% and a purity of 98.6 ± 0.8%, whereas for the 3 μm particles, a separation efficiency of 99.4 ± 0.2 % and a purity of 100% were recovered from Outlet 1. A mixture of 5 and 10 μm particles was well separated in this integrated device, which proved that the relatively small size difference of the particles can be separated readily. The DEP-assisted hydrophoretic separation device has other advantages such as avoiding the possibility of blockage and tuning the external voltages for different assays. It could potentially be a critical component in advanced lab-on-a-chip bioanalysis devices.

6. Development of a novel magnetophoresis-assisted hydrophoresis microdevice for rapid particle ordering[*]

6.1. Introduction

In the last few decades, there is a trend towards miniaturization and integration of chemical or biological laboratories into a microfluidic chip, which has several promising advantages, such as low costs, portability, precise manipulation of fluid and particles, lower volume reagents and rapid analysis. It is a routine procedure to accurately handle the specific micro- or nanoparticles conjugated with biological or chemical species of interest for characterization and measurement purposes [170, 171]. Particles or cells are typically focused into an identical streamline by flow cytometry for a more accurate analysis [172]. The problem with this approach is that it is bulky, expensive and requires sheath flows to focus particles. It is crucial to develop novel approaches enabling the devices cheap, accessible and portable.

Groove-based microfluidic focusing is one such method. Ligler's group [173-176] proposed microflow cytometers using groove-generated sheath flow for cell assay and bacteria detection. However, the focusing performance highly depends on the accurate control of flow rate. Hydrophoresis is a sheathless method, an emerging passive approach that utilizes the steric effects between particles and grooves [4]. The hydrophoretic devices have so far been demonstrated for many biological applications, *i.e*. blood cell separation [35, 36], cell cycle synchronization [177], focusing on mammalian cell lines [4] and cell removal [178]. However, the hydrophoresis method is limited by its fixed operation range. The devices are designed and fabricated with appropriate dimensions for specific assays. Once the target particles are changed to new sets, the hydrophoretic channel has to be redesigned and refabricated to satisfy the new requirements. Choi and Park [28] previously reported a tunable hydrophoretic device fabricated in poly-(dimethylsiloxane) (PDMS) where the channel height was reduced by

[*] Results of this chapter are published in: Sheng Yan, Jun Zhang, Huaying Chen, Dan Yuan, Gursel Alici, Haiping Du, Yonggang Zhu, Weihua Li, Development of a novel magnetophoresis-assisted hydrophoresis microdevice for rapid particle ordering. ***Biomedical Microdevices***, 18, 1-9, 2016.

applying compressive stress to the device. Another approach to tune hydrophoresis was implemented by our group [47, 48, 112, 179] using a dielectrophoresis (DEP)-assisted hydrophortic device where interdigitated electrodes were embedded on the bottom of the channel, generating negative DEP to assist particles in forming hydrophoretic ordering. Alternatively, replacing micro-electrodes with a diaphragm could tune the critical diameter of hydrophoretic devices via the applied pressure on the diaphragm [123]. Tunable devices are demanding in a live feedback system, where the parameters of microchannel can be adjusted on real-time to retrieve the expected results without fabricating new devices.

Magnetophoresis, a motion of particles under the effects of magnetic fields, is a simple manipulation technique that has gained considerable attention in the last decade. Due to its non-contact nature and independent of solution pH, ionic concentration, surface charge and temperature, a number of techniques using megnetophoresis have been reported in many biological studies [82]. To manipulate cells that are non-magnetic in nature, functionalized magnetic beads were conjugated with cells of interest through either enbocytosis or ligand-receptor interaction at their surface [180]. Plouffe *et al*. [181] presented an optimised magnetophoretic device for isolating a magnetic-particle-tagged cell population from a homogeneous suspension. Forbes *et al*. [182] introduced a magnetophoretic separation of immunomagnetically labelled rare mammalian cells using an angled magnet. As positive magnetophoresis involves in cell-bead conjugation for specific manipulation, the whole assay lasts longer due to several hours' incubation. Besides, multiple washing steps are labour-intensive and may cause cell loss [84, 180]. In positive magnetophoresis, microparticles will be attracted towards the maximum magnetic strength, however, in negative magnetophoresis, they will be repelled to the opposite direction: the minimum magnetic strength. Negative magnetophoresis is a label-free manipulative technique, which can address the above-mentioned issues [183]. In this case, the diamagnetic particles or cells are dispersed in a magnetic fluid such as a paramagnetic salt medium [82, 184]or a ferrofluid [86, 185]. In magnetophoretic devices, magnetic forces should overcome drag forces to precisely control the particle movements. Particles of interest laterally migrate at a larger distance to distinguish from their mixtures [186].

In this work, we propose a magnetophoresis-assisted hydrophoretice device, which takes the advantages of the both methods. Unlike other magnetophoresis-based techniques that drive the particles to move a long distance in the lateral direction, the proposed method utilizes megnetophoretic force to push particles downwards in the height direction, which then couples with hydrophoretic effect to form particle ordering. Magnetophoresis as an active method can relax the restriction of the height dimension of hydrophoretic devices. The outline of this paper is as follows: Materials and methods section will introduce the methodology, fabrication, material preparation, experimental setup and numerical simulation. The main results will be presented in Results and discussion, including the effects of flow rate, particle diameter, ferrofluidic concentration and number of magnets on the focusing efficiency. The main conclusion will be drawn in Conclusion section.

6.2. Materials and methods

6.2.1. Methodology

Hydrophoresis employs anisotropic grooves to generate helical flow patterns in the microfluidic channel. Typically, particles travel back and forth along the transverse direction following the vortexes (Figure 6-1a). However, particle-groove interaction plays a dominant role once the diameter of the particles exceeds the half of the channel height. The particle-groove interaction diffuses the particles out of their streamlines and leads to a new equilibrium position; this is called hydrophoretic ordering and the critical diameter to be focused in the hydrophoretic channel is defined as the half of the channel height [112].

To overcome the lack of flexibility in focusing small particle whose diameter is less than the critical diameter, megnetophoresis is involved in extending the operational range of hydrophoretic device. The magnetic force exerting on a magnetised body in a suspending fluid under a non-uniform magnetic field is expressed as [79]:

$$F_{mag} = \mu_0 V_p[(M_p - M_f) \cdot \nabla]H \qquad 6\text{-}1$$

where μ_0 is the permeability of free space ($4\pi\times10^{-7}$ H m^{-1}), V_p is the volume of the particle, $\mathbf{M_p}$ is the magnetization of the magnetized particle, $\mathbf{M_f}$ is the magnetization of

the fluid, and **H** is the magnetic field at the center of the particle. Eq. 6-1 states that particles of different size, V_p, and/or magnetizations, $\mathbf{M_p}=\chi_p\mathbf{H}$ with χ_p being the dimensionless magnetic susceptibility of the particle, experience different magnetophoretic forces in the same suspending fluid ($\mathbf{M_f}=\chi_f\mathbf{H}$ with χ_f being the magnetic susceptibility of the fluid). Eq.6-1 can be expressed in another form:

$$F_{mag} = \mu_0(\chi_p - \chi_m)V_p(H \cdot \nabla)H \qquad 6\text{-}2$$

For a magnetic particle ($\chi_p > 0$) dispersed in an aqueous diamagnetic medium ($\chi_m < 0$), a positive magnetophoresis is generated in this mode, where the particle migrates to the region of a strong magnetic field. On the contrary, if the particle is diamagnetic ($\chi_p < 0$) and the medium is paramagnetic ($\chi_m > 0$) then the difference between the values becomes negative and the particle is repelled from the magnetic field towards an area of field minima.

In our experiments, the diamagnetic particles were experienced two significant forces: magnetic repulsion force and drag force. The drag force in the *z*-axis is expressed as: $F_{dz}=-6\pi R\eta(v_{mz}-v_{pz})$, where R is the radius of the particle, η is the viscosity of the medium, v_{mz} and v_{pz} are the *z*-velocity of the flow and the particle [187]. Typically, magnetic repulsion force should be larger than the z-component of the drag force, which can be expressed as: $|F_{dz}|<|F_{mag}|$. Therefore, a dimensionless parameter in our magnetophoresis-assisted hydrophoretic system can be defined as:

$$1 < \frac{|F_{mag}|}{|F_{dz}|} = \frac{2}{9\mu_0\eta} \cdot \frac{|\chi_p - \chi_m|}{|v_{mz} - v_{pz}|} \cdot (\mathbf{B} \cdot \nabla)\mathbf{B} \cdot R^2 \qquad 6\text{-}3$$

This term encompasses all the relevant variables into a single dimensionless parameter. At a lower flow rate, the magnetic force can easily overcome the drag force and push particles downwards to the lower level of the channel, where the intensive particle-groove interactions enable the particles to form hydrophoretic ordering (Figure 6-1b). Also, the particle with a larger radius can be easily focused. Besides, increasing the magnetic field and susceptibility mismatch of the particle and the fluid would be alternatives in focusing particles.

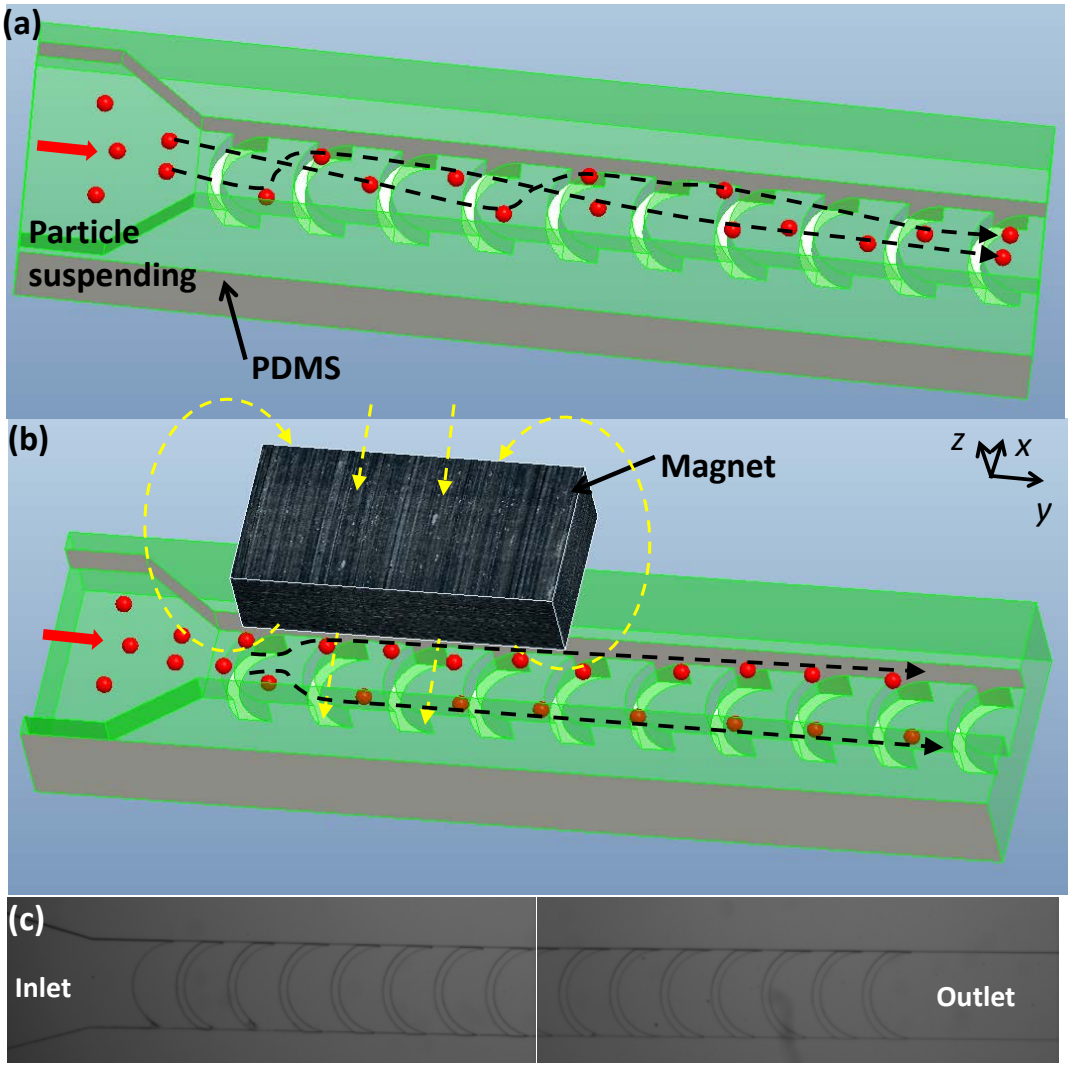

Figure 6-1 Microfluidic device for hydrophoretic particle ordering. (a) Overview of the hydrophoretic device operation and structure. In the absence of magnetic field, randomly distributed particles migrate back and forth in the channel. (b) With the magnetic field, the particles were pushed downwards by the magnetic repulsion force, which enhances the particle-groove interactions. The particles satisfying the hydrophoretic ordering can be focused along the sidewalls of the channel. (c) Optical micrograph images of the hydrophoretic channel.

6.2.2. Fabrication

Figure 6-1c shows the optical images of hydrophoretic channel. The hydrophoretic channel consisted of a series of grooves with a small curvature of 600 μm and a large

curvature of 650 μm. Both channel height and groove height were 40 μm. The channel was 600 μm wide and 20 mm long.

Figure 6-2a shows a schematic diagram of the overall procedures for fabrication of the microfluidic platform with L-shaped interconnections. Sylgard 184 elastomer base and curing agent (Dow Corning Corporation, Midland, USA) were completely mixed at a weight ratio of 10:1 and degassed under vacuum. Subsequently, a small portion of the PDMS mixture was cast against the mold that was fabricated by standard photolithography [19, 48]. The thickness of the first PDMS casting was remained to be approximately 1 mm (Figure 6-2a I). Such thin layer was convenient for removing the residual PDMS fragments after punching the vertical holes. Afterwards, the PDMS mixture on the mold was baked in an oven at 65 ºC for 45 min and then taken out from the oven before complete curing. The modified syringe needles were placed on the corresponding inlet and outlet. To obtain the modification of syringe needles, syringe needles (25 G, Terumo needle, Terumo Corporation) were sawed at the neck in order to get rid of the plastic inlet. The sticky surface of PDMS can prevent the modified needles from rolling when implementing second PDMS casting. To avoid the penetration of PDMS by the cutting tips (Harris Uni-Core Punch; Ted Pella, Redding, CA, USA), the second PDMS layer was controlled to be around 3mm in depth (Figure 6-2a II). The step (II) can be repeated multiple times to fabricate the three dimension (3D) microfluidic ports. The cured PDMS replica was peeled off from the mold, with pulling off the needles from PDMS using a pair of tweezers. The vertical holes for inlet and outlet ports were punched to the lateral holes, rather than cutting through the whole PDMS slab, using a cutting tip (Ø 0.75 mm). The residual PDMS fragments produced by the cutting tips were carefully removed by tweezers (Figure 6-2a III). Both the PDMS replica and a glass slide were then treated using a plasma cleaner (PDc-002, Harrick Plasma, Ossining, NY) for 3 min, before they were brought into conformal contact (Figure 6-2a IV). The L-shaped interconnections were then connected to Tygon tubing (Ø 0.7 mm, Tygon R-AAQ04103; Saint-Gobain Performance Plastics, Akron, OH, USA) using 21-gauge flat-ended needles.

Conventionally in a through-hole type interconnection for particle injection, the flat-ended needles are used to penetrate the chip and connected through inlet and outlet

holes that are vertical to the flow direction (Figure 6-2b). Once the chip is flipped, the flat-ended needles with Tygon tubing are unable to keep the chip stable on the travelling stage of the microscope. Furthermore, the flat-ended needles increase the distance between micro-chip and the objective lens, which may cause the captured images out of focus. In the current study, the L-shaped interconnection is proposed as a remedy for the above issues (Figure 6-2c). The micro-chip can be easily flipped without any unstable and out-of-focus issues. A schematic drawing of the whole device is shown in Figure 6-2d.

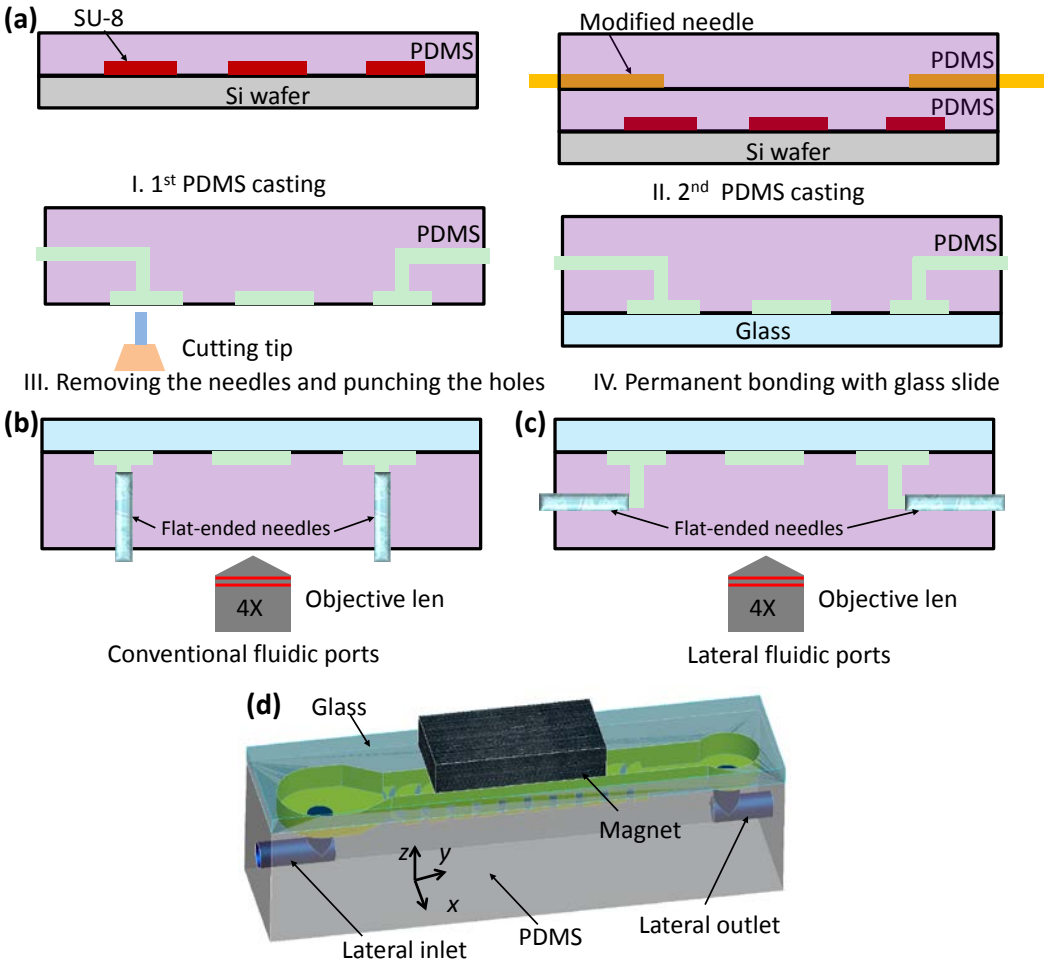

Figure 6-2 (a) Schematic view of fabrication process flow. A schematic cross-sectional drawing of (b) the conventional fluidic ports and (c) the novel lateral fluidics ports. (d) Three dimensional animated model showing the overview of the device.

6.2.3. Material preparation

A commercial water-based magnetite ferrofluid (EMG 408, Ferrotec Co., NH) was used in our experiments. The volume ratio of the magnetite particles for this ferrofluid is 1.1%. The mean diameter of nanoparticles is 10.2 nm. The initial magnetic susceptibility is measured to be 0.26; the saturation magnetization (μ_0M) is 60 Gauss; the dynamic viscosity is 1.2×10^{-3} kg (m s)$^{-1}$ [185]. The fluorescent microparticles with diameters of 5, 8, 10, 13 μm (Coefficient of variation 5%, 18%, 5%, 16%) were purchased from Thermo Fisher Scientific Corporation. The microbeads were re-suspended in ×0.02 EMG 408 ferrofluid to a final concentration of 10^6 particles per millilitre. To optimise the focusing performance of the 5 μm beads, the beads were re-suspended in ×0.05 and ×0.1 ferrofluids. To prevent the beads from sedimentation and aggregation, 0.1% (in volume) Tween 20 (Sigma-Aldrich, product no. P9416) surfactant was added to this aqueous medium.

Prior to each experiment, the device was rinsed with DI water at 20 μl min^{-1} for 20 min using a syringe pump. To prevent immediate particle adhesion to the PDMS surface, 0.1% Tween 20 in DI water was injected into the microchannel and incubated at 37 ºC for 30 min to coat the PDMS surface.

6.2.4. Experimental setup

A non-uniform magnetic field was generated by a stack of three NdFeB permanent magnets. Each magnet is 2 mm in width, 2 mm in length, and 2 mm in thickness. The magnets stack was placed on the top of the glass as indicated in Figure 6-2d. The magnetic flux density at the center of the magnets' pole surface was measured to be 300 mT by a Gauss meter (Model 5180, Pacific Scientific OECO). The magnetization direction of these magnets is perpendicular to the hydrophoretic channel. A syringe pump (Legato 100, Kd Scientific) was used to inject the particle suspension into the micro-channel. All images were captured through an inverted microscope (CKX41, Olympus, Japan) with a CCD camera (Rolera Bolt, Q-imaging, Australia) and an image processing program (Q-Capture Pro 7, Q-imaging, Australia).

6.2.5. Numerical simulation

The particle trajectories in microchannel were numerically modelled using finite element software (COMSOL Multi-physics 5.0 COMSOL, Burlington, MA). The 3D modelling for simulation was identical to the experimental channel. With magnetic fields, the particle trajectories were simulated by coupling Laminar Flow module, Magnetic Fields module and Particle Tracing module. First, the Laminar Flow module was utilised to investigate the fluid flow inside the 3D channel. For modelling the laminar flow of diluted ferrofluid inside the microchannel, continuity equation and Navier-stokes equation were expressed as: $\rho\nabla \cdot \boldsymbol{u} = 0$ and $\rho(\boldsymbol{u} \cdot \nabla)\boldsymbol{u} = \nabla \cdot [-p\boldsymbol{I} + \mu(\nabla\boldsymbol{u} + (\nabla\boldsymbol{u})^T)]$, where $\boldsymbol{u}$ is velocity vector of fluid, p is fluid pressure, and ρ is fluid density. No-slip boundary conditions were set to the channel walls. The flow was assumed to be incompressible. The flow rate released at the inlet was 20 µl min^{-1} and the pressure at the outlet was zero. The Magnetic Fields module was employed to calculate the non-uniform magnetic fields generated by the permanent magnets. The governing equations were $\boldsymbol{H} = -\nabla V_m$ and $\nabla \cdot \boldsymbol{B} = 0$, where V_m is magnetic scalar potential, $\boldsymbol{B}$ is magnetic flux density, and $\boldsymbol{H}$ is magnetic field. A Faraday cage was also built to contain the hydrophoretic channel and magnet to exclude electrostatic and electromagnetic influences (Figure 6-3a). The Zero Magnetic Scalar Potential was chosen from one of the Faraday cage's corners. A stationary solver was used to compute the magnetic field (Figure 6-3b). Finally, the Particle Tracing module was used to couple the magnetophoretic force and the hydrodynamic drag force to predict the particle trajectories. The equations of the magnetophoretic force and drag force embedded in the COMSOL software were used without modifications. At the inlet, particles were evenly released along with the channel width. The particle density and diameter were set to 1050 kg m^{-3} and 13 µm, respectively. Permanent magnet relative permeability is 1.05, air and PDMS relative permeability is 1, particles relative permeability is 1, and ferrofluid relative permeability is 1.026. The time for beads migrating in the channel was set to 5 s and the time interval for each step was set to 0.001 s, which provided smooth particle trajectories. The Free Tetrahedral was used in the model mesh.

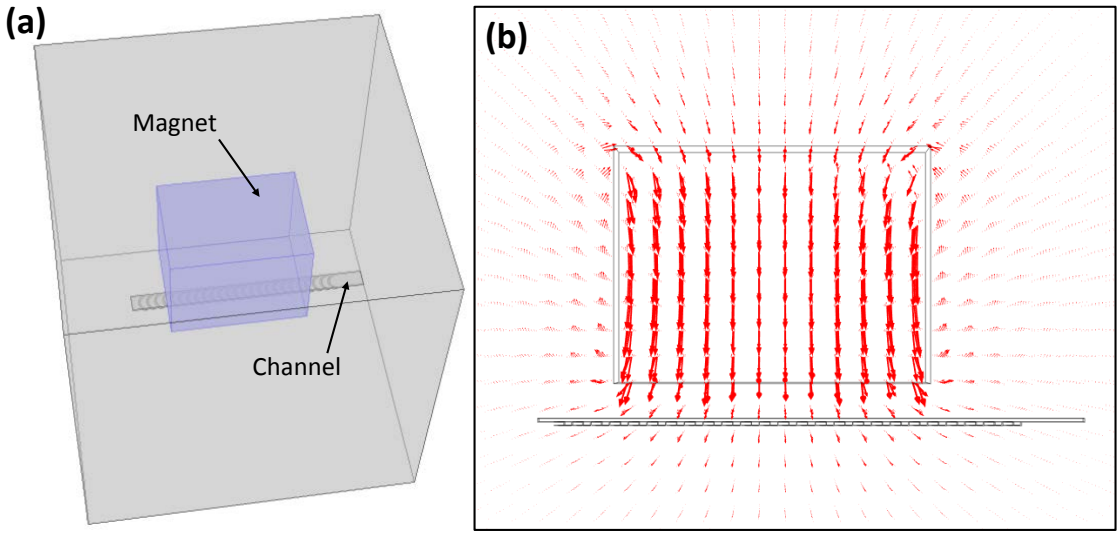

Figure 6-3 (a) The 3D full model considered; (b) The distribution of magnetic field generated by the magnet in the 3D model. The red arrows represent the vectors of the magnetic field.

6.3. Results and discussion

6.3.1. Magnetophoresis-assisted hydrophoretic ordering

First, the effect of negative magnetophoresis to assist the hydrophoretic ordering was investigated. Using the device with hydrophoretic channel, ferrofluid, and magnets, the different patterns were observed when beads passed through the channel. Figure 6-4a and b show the simulated and experimental particle trajectories in the magnetophoresis-assisted hydrophoretic device without a magnetic field. The flow rate applied in the numerical model and experiment was 20 µl min^{-1} and the beads injected into the channel were 13 µm. Since the particle diameters were smaller than half of the channel height, they could not meet the requirement of hydrophoretic ordering and thus migrated back and forth inside the channel. After applying the magnetic field, the particles released evenly from the inlet were pushed by the magnetic repulsion force towards to the lower level of the channel, where the particle-groove interactions diffused particles out of helical motion and drove particles to a new equilibrium position (Figure 6-4c). Figure 6-4d shows the optical micrographs of particle trajectories of 13 µm beads passing through the magnetophoreisis-assisted hydrophoretic device. The measured trajectories agree reasonably well with the simulation result shown in Figure

6-4c. Regardless of the initial positions, all the beads were focused onto the sidewalls of the channel.

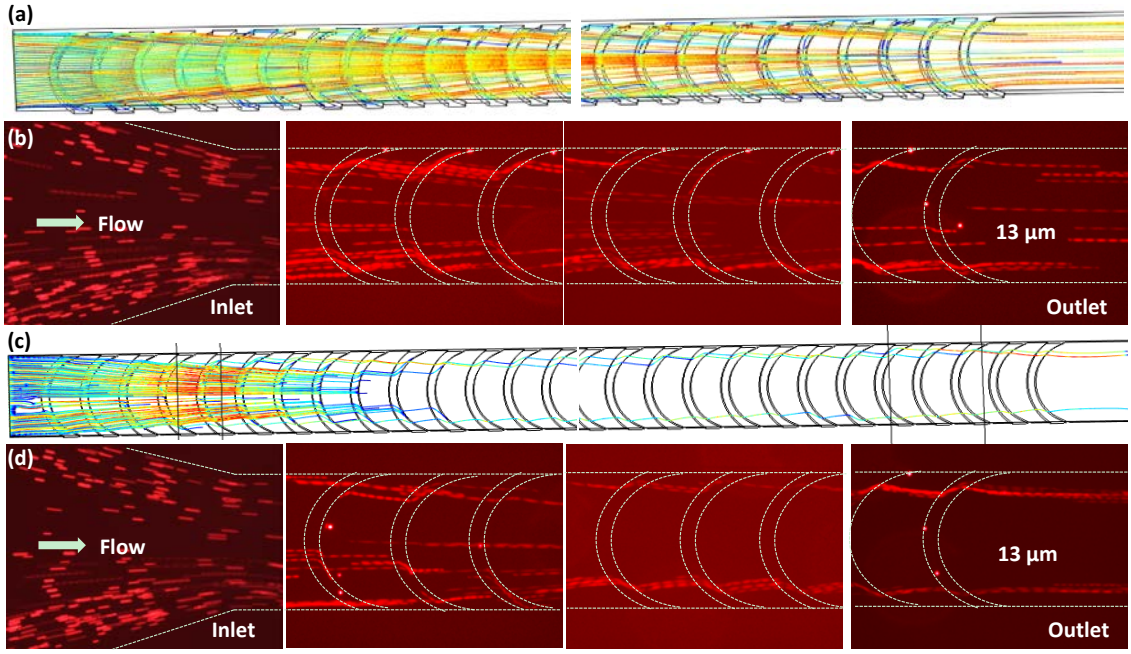

Figure 6-4 Experimentally focused patterns and numerically predicted particle tracing of 13 µm particles. The applied flow rate was 20 µl min^{-1}. The beads were evenly distributed at the inlet. (a) Simulated particle trajectories at both the inlet (Left) and the outlet (Right) without a magnetic field. Particles migrated back and forth were not focused in the channel. Red color represents high speed, blue low velocity. (d) Under a magnetic field, particles were focused onto the sidewalls of the channel once forming the hydrophoretic ordering. Optical microscopy images showing the focusing patterns (b) without a magnetic field and (d) with a magnetic field.

6.3.2. Effect of flow rate

The dependence of magnetophoretic-assisted hydrophoretic particle ordering on the flow rate was verified as the flow rate ranged from 10 to 80 µl min^{-1} in the presence of magnetic field. The particles with a diameter of 13 µm were used as a model. When introduced into the channel, the particles will experience both the inertial and viscous forces. To examine the relative effect of these two forces, we calculated the particle Reynolds number R_p which is the dimensionless ratio of particle inertia to the viscous force [32]., i.e. $R_p = (\rho d^2 u)/(\mu D_h)$, where D_h is the hydraulic diameter defined as $D_h =$

$2wh/(w+h)$. For $R_p>1$, the particle inertia plays a dominant role and the equivalent paths of particles under hydrophoretic ordering are also affected by the inertial force. To simplify the calculation, the presence of the grooves was ignored, so the linear velocities of particles passing through the 600 μm wide by 40 μm high channel ranged from 0.69 to 5.53 cm s^{-1}. The resulting particle Reynolds number is 0.12 for 13 μm beads at the maximum working flow rate of 80 μl $min^{-1.}$ Therefore, under the present experimental conditions, the particle inertial effect can be omitted.

Figure 6-5a shows the focusing efficiency of 13 μm particles under various flow rates. The focusing efficiency is defined as $E_n=(w-d/2-a)/(w-d)$ [42], where a represents the width of the focused particle stream, $a=a_1+a_2$ (Figure 6-5b). Below 20 μl min^{-1}, the flow rate had little effect on the focusing efficiency because the magnetic repulsion force played a dominant role and the particles travelled in a limited space where the particle-groove interactions were enough to focus them well (Figure 6-5b and c). In contrast, the exposure time to magnetic repulsion force was not long enough to keep particles focused well when the particles passed through the channel at a higher flow rate. The focusing efficiency decreased from 82.5±2.2% to 76.4±2.0% with the increase of flow rate from 30 to 50 μl min^{-1} (Figure 6-5d and e). Above 80 μl min^{-1}, the particles occupied the entire channel at the outlet, which meant they could not form self-ordering any longer (Figure 6-5f).

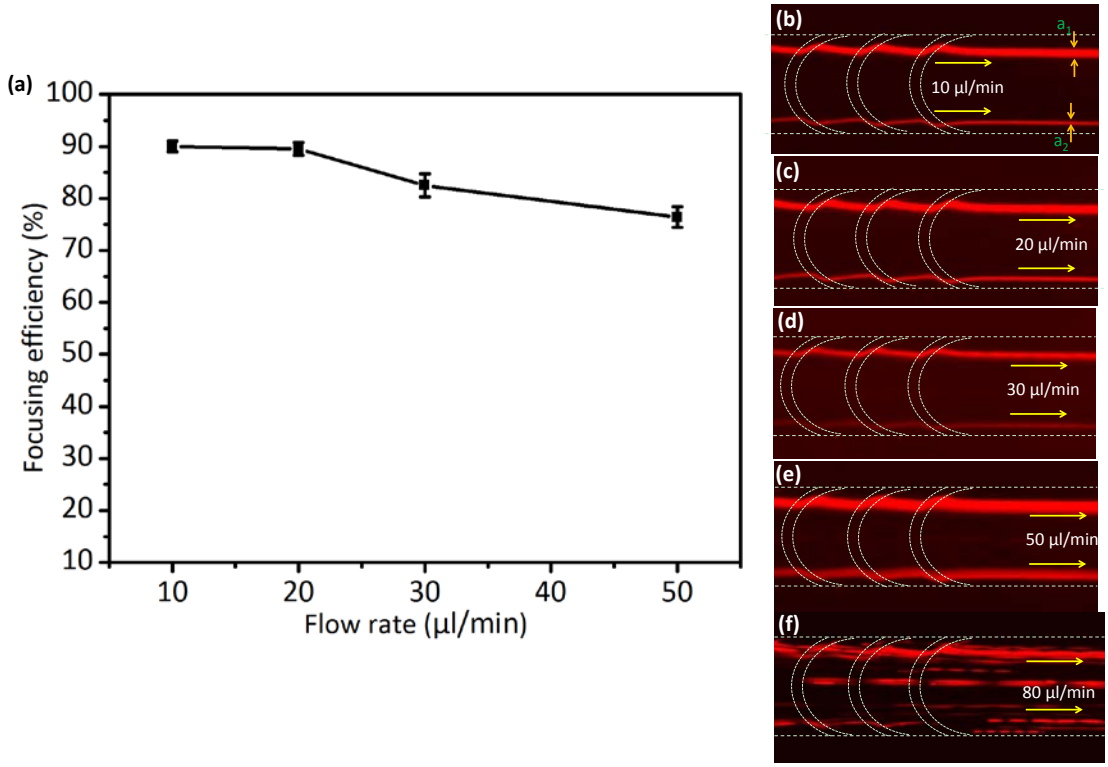

Figure 6-5 (a) Measured focusing efficiency of 13 µm particles. The flow rate ranged from 10 to 50 µl min^{-1} and a magnetic field was applied. The average value was 3 times the measurement. (b)-(f) Optical micrographs showing the particle trajectories in the channel at the flow rate of 10, 20, 30, 50 and 80 µl min^{-1}. The average value was 3 times the measurement and the error bar represented the standard deviation.

6.3.3. Effect of particle diameter

As indicated in Eq. 6-3, the volume of the microsphere is an important parameter to determine the magnetic force. To investigate the effect of diameter on the focusing efficiency, 5, 8, 10, and 13 µm polystyrene particles were suspended in ×0.02 EMG 408 ferrofluid and pumped through the microchannel. They were individually introduced into the microfluidic channel at a flow rate of 20 µL min^{-1}. Before encountering the magnetic field created by magnets, the particles were evenly distributed across the width of the channel. When passing through the magnetic field, the particles experiencing repulsion forces were pushed downwards in the microchannel.

Figure 6-6a-c shows the focusing profiles of different particle diameters at the outlet without a magnetic field (Left) and with a magnetic field (Right). Since the larger

particles (i.e, 10 and 13 μm beads) exerting larger magnetic repulsion force could easily form hydrophoretic ordering, narrower focusing bands were observed. The focusing efficiency of 10 and 13 μm beads reached to 90±2% and 89±2.5%, respectively (Figure 6-6d). Based on the experimental results, the focusing efficiency of 13 μm beads was slightly lower than that of 10 μm beads due to the wider variation of 13 μm particles (CV:~16%). In contrast, the focusing efficiency dropped to 64.1±3% for 8 μm beads, and 40.4±2.2% for 5 μm beads (Figure 6-6d). Even though 5 μm particles had a tendency to focus onto the sidewalls of the channel, the low focusing efficiency proved that helical flows were dominant in the particle motion. However, increasing the concentration of ferrofluid and number of magnets would be good options to improve the focusing efficiency of 5 μm beads.

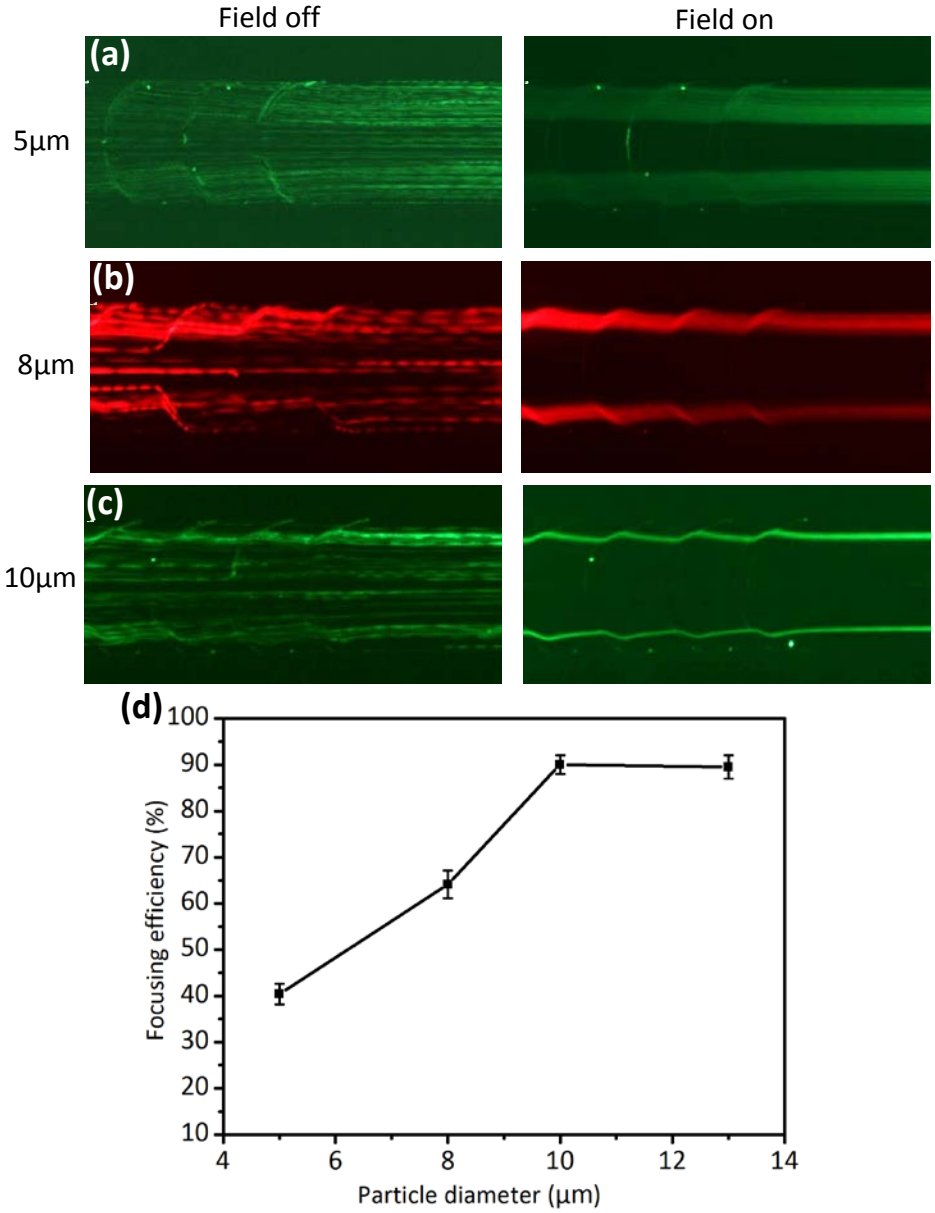

Figure 6-6 (a)-(c) Optical micrographs showing the particle motion of 5, 8 and 10 µm beads at the outlet without a magnetic field (Left) and with a magnetic field (Right). The applied flow rate was 20 µl min^{-1}. (d) Measured focusing efficiency of distinct particles. The average value was 3 times the measurement and the error bar represented the standard deviation.

6.3.4. Effect of ferrofluidic concentration and number of magnets

As demonstrated above, small particles were not focused well in the ×0.02 ferrofluid. To demonstrate the tunability of magnetophoretic-assisted hydrophoretic device, more

magnets and a higher concentration of ferrofluid were used to improve the focusing efficiency of 5 μm beads. The concentration of ferrofluid can affect the magnetic susceptibility of the medium (χ_m). Eq. 6-2 illustrates that increasing χ_m results in increased relative susceptibility between particles and medium, and therefore greater magnetic repulsion force applies on the diamagnetic particles. Here, the ferrofluid was added to the particle suspending with a final dilution of 0.05 and 0.1 to investigate the effect of ferrofluidic concentration on focusing efficiency. In addition, more magnets arranged on the top of the channel can not only increase the exposure time to the magnetic field, enabling beads to migrate a larger distance, but also enhance the magnetic field, which in turn affects the magnetic force. The 5 μm beads were injected through the channel with a flow rate of 20 μL min^{-1} with different numbers of magnets placed in a row as indicated in Figure 6-2e.

Figure 6-7a and b show the focusing profiles of 5 μm beads at the outlet with different working conditions. As the number of magnets increased from 2 to 4 in ×0.05 ferrofluid, the beads were prone to focus along the sidewalls of the channel with narrower bands. The focusing efficiency increased dramatically from 14.4% to 52.4% (Figure 6-7c). The improvement was attributed to the longer exposure time under the magnetic field and stronger magnetic field. At 20 μL min^{-1}, the average velocity of beads in the channel is 13.8 mm s^{-1}. The particle residence time under the magnetic field was 0.29s, 0.43s, and 0.58s, separately, with the number of the magnet from 2 to 4. The greater residence time in 4-magnet setup allowed particles to migrate a longer distance over a greater period. Besides, it should be noted that the intensity of magnetic field varied with the number of the magnet. The values of the magnetic field at a distance of 1 mm (the thickness of glass) were 119, 149 and 190 mT. Thus, as the particles passed through the magnetic field, they experienced a slightly larger repulsive effect in 4-magnet setup.

Although similar behavior was observed in a ×0.1 ferrofluid, the focusing efficiency was higher when compared to that in the ×0.05 ferrofluid. The ×0.1 ferrofluid with more magnetic material content increased the magnetic susceptibility of the medium, resulting in larger magnetic force. The focusing efficiency increased from 52.4% to 62.0% in the presence of 4 magnetic blocks, which was the best result in the work.

However, the focusing efficiency could be further improved by increasing ferrofluidic concentration and using a larger magnet with the stronger magnetic field. Alternatively, particle trajectories can be altered by an electromagnet whose magnetic field can be tuned by the applied current.

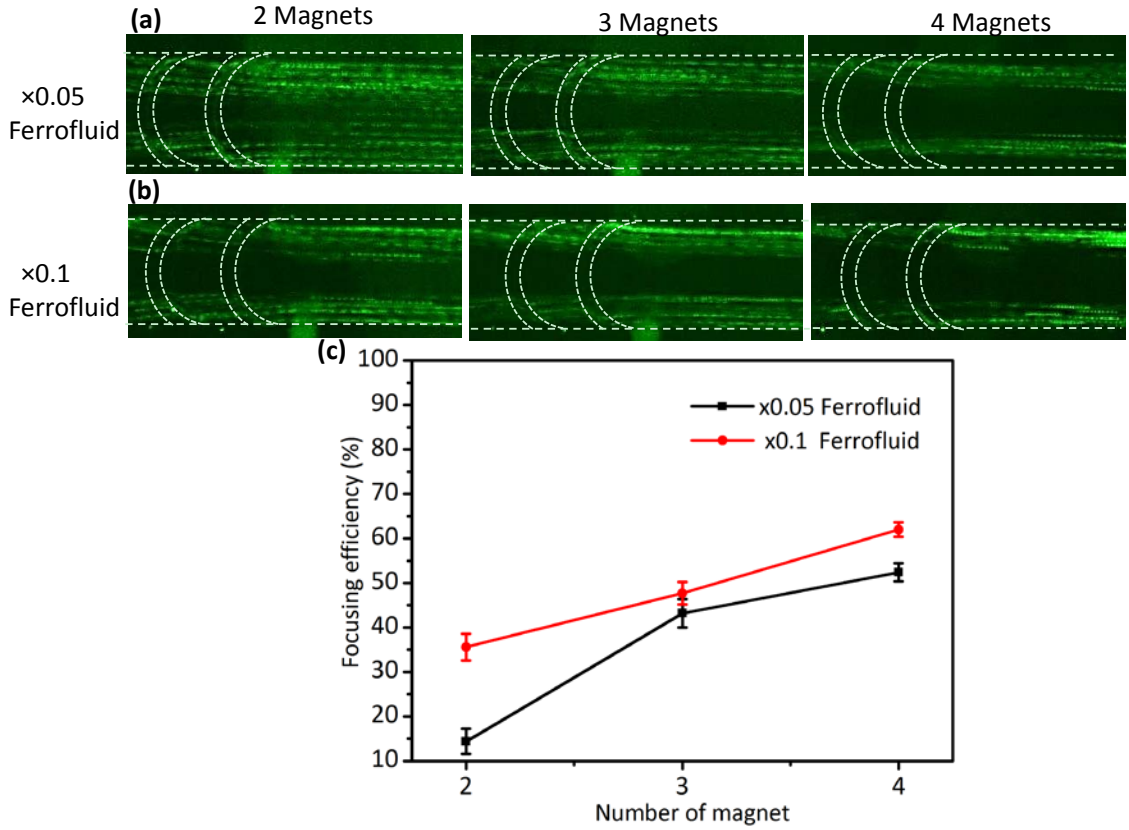

Figure 6-7 Focusing patterns of 5 μm beads at a flow rate of 20 μL min^{-1} with different numbers of magnets, ranging from 2 to 4. The optical microscopy images show the particle trajectories at the outlet in ×0.05 ferrofluid (a) and ×0.1 ferrofuid (b). (d) Measured focusing efficiency of 5 μm particles under different numbers of magnets and ferrofluidic concentration. The average value was 3 times the measurement and the error bar represented the standard deviation.

6.4. Conclusion

The work proposed a new concept of magnetophoresis-assisted hydrophoretic ordering using a simple setup of inexpensive permanent magnets, and without the need for high-powered instruments (e.g. lasers or high voltage power supply). The critical limitation of magnetophoresis-based device operating at a low flow rate and the specific

hydrophoretic device for focusing a given size of particles were overcome by this new microfluidic platform. To implement this method, a novel lateral fluidic port was introduced to keep the flipped chip stable. The motion of the microparticles was investigated and explained using numerically simulated particle trajectories and experimental results with and without the magnetic field. A high-throughput focusing was achieved with this new magnetophoresis-assisted hydrophoretic system, even when the flow rate was increased to 50 μL min^{-1}. The device has been demonstrated to successfully focus polystyrene fluorescent particles with 5, 8, 10, and 13 μm diameters. To achieve the better focusing efficiency of 5 μm beads, the higher concentration of ferrofluid and more magnets were applied to tune the focusing patterns. This novel approach represents a versatile tool for rapid, label-free focusing. It can also facilitate the connection with other microfluidic platforms for downstream sorting and /or analysis.

7. High-throughput, sheathless, magnetophoresis-assisted separation of magnetic and non-magnetic particles in a hydrophoretic channel

7.1. Introduction

Bead-based immunoassays in microfluidics enable biological samples [188, 189] to be detected and separated more accurately. Conjugation with beads can amplify the volume of target objects (*e.g.* cells, DNA, protein) via specific antibody-antigen reactions and also change their magnetic and dielectric properties, and the density [190]. By tagging target cells with immuno-labelled beads to enhance their size, the target cells can be separated from non-target cells of a comparable size [191, 192]. Elastomeric beads are popular in acoustophoretic devices because they can make the tagged target cells less dense [193]. In addition, polystyrene particles are used to bind with target objects so that the bound complexes show different dielectrophoretic behaviour in an alternate field and are thus separate from non-labelled objects [194]. However, cells of interest are labelled with immunomagnetic beads to be handled in a magnetic field are called "positive magnetophoresis". Due to their non-contact nature, the viability of cells can be secured by avoiding potential hazards, and since magnetic separation is no influenced very much by any changes in the chemical or thermal characteristics of the fluid carrier, separating the target cells that have conjugated with magnetic beads can be simplified into separating magnetic particles from non-magnetic particles.

Several microfluidic devices that will separate magnetic from non-magnetic particles have been reported [186]. Magnetophoretic separation normally requires a sheath flow to pre-focus the samples containing paramagnetic beads and diamagnetic beads, and then the paramagnetic beads are deflected from the initial fluid stream in a magnetic field. Zhu *et al*. [86] used permanent magnets to separate magnetic and non-magnetic particles of the same size under a maximum flow rate of 3 µl min^{-1}. Xia *et al*. [195] integrated micro-comb and micro-needle structures to enhance the magnetic field, after which non-magnetic beads (2.0 µm in diameter) and magnetic beads (1.6 µm in diameter) were separated with an efficiency of ~90%, at a flow rate of <1 µl min^{-1}.

In all these studies, a sheath flow is needed to for separation because particle suspension is pushed to one side of the channel and the magnetic beads are deflected laterally from

non-magnetic beads under a magnetic field. To improve the displacement of magnetic beads means increasing the exposure time to the magnetic field because it decreases sharply as the distance from the magnetic source increases [196]. All these factors lead to a low flow rate in magnetophoresis-based chips. Moreover, sheath flow requires an accurate flow control because any unstable pumping means the particles will not be confined perfectly and will be deflected from their original positions [4]. This is why a high-throughput, sheathless magnetophoresis device is needed to address these issues. If magnetic beads migrated vertically, the width of the channel would have almost no effect on their deflection, so increasing the width of the channel will dramatically improve their throughput. Moreover, this type of magnetophoresis can be joined with other hydrodynamic effects to achieve a sheathless particle separation.

Several sheathless techniques for separating particles in microfluidics have been reported in the literature review [99], of which the groove-based channel can separate particles with a different position in the height direction. A groove-based channel for mixing was first proposed by Stroock *et al*. [197] using a vortex; this was then developed for trapping by Gadish and Voldman [198], using a combination of microvortex and dielectrophoretic phenomenon. Later, Hsu *et al*. [199] used the microvortex generated by grooves to separate a binary mixture of beads with differing densities.

The aim here is to develop a microfluidic device that couples magnetophoresis and microvortex for a high-throughput, sheathless separation of magnetic beads from non-magnetic beads. Magnetic and non-magnetic beads are suspended in a diluted ferrofluid and located at different equilibrium positions by balancing magnetophoretic and drag forces without sheath flow (Figure 7-1a and b). Throughput can be improved significantly by widening the channel, even though it is not related particle deflection in a vertical direction. To the best of our knowledge, this is the first work in which magnetophoresis and microvortex are combined in order to have a stable separation of target objects from non-target ones.

7.2. Materials and methods

7.2.1. Methodology

The particles in this device experience two primary forces: a drag force induced by secondary flow, and a magnetophoretic force. The drag force in the *z*-axis is expressed as $F_{dz}=3\pi d\eta v_z$, where d is the diameter of the particle, η is the viscosity of the medium, and v_z is the *z*-velocity of the flow [187]. The magnetic force (F_{mag}) on a particle is expressed in Eq. 6-2 [79].

For a magnetic particle ($\chi_{p1} > 0$) dispersed in an aqueous diamagnetic medium ($\chi_m < 0$), a positive magnetophoresis is generated and the particles migrate to the region of a strong magnetic field, but if the particles are diamagnetic ($\chi_{p2} < 0$) and the medium is paramagnetic ($\chi_m > 0$) then the difference between the values becomes negative and the particles are repelled from the magnetic field towards an area of field minima. In our study the magnetic and non-magnetic beads were prepared in ×0.05 EMG 408 ferrofluid in which $\chi_{p1} > \chi_m > \chi_{p2}$; this is where the magnetic beads experience positive magnetophoresis and the diamagnetic beads exert magnetic repulsion forces.

The equilibrium of magnetic beads (indicated as an orange sphere in Figure 7-1b) is located at the centreline of the channel where two adjacent counter-rotating microvortices converge. The magnetic beads are attracted towards the magnet by the balancing magnetic force and vertical drag force. In a lateral direction (along with the *x*-axis), the drag forces are balanced but non-magnetic particles have two “trap sites” located near the sidewalls, so the magnetic repulsion forces push particles upwards to the upper level of the channel where particle-groove interactions enable hydrophoretic focusing [92].

7.2.2. Device fabrication and design

Microfluidics devices are fabricated by two-step photolithography and soft lithography. Figure 7-1c shows a top view of the 600 μm wide by 2 cm long channel with 60 grooves, each of which has a small 300 μm curvature and a large curvature of 350 μm. Each layer of the SU-8 mould is 40 μm high.

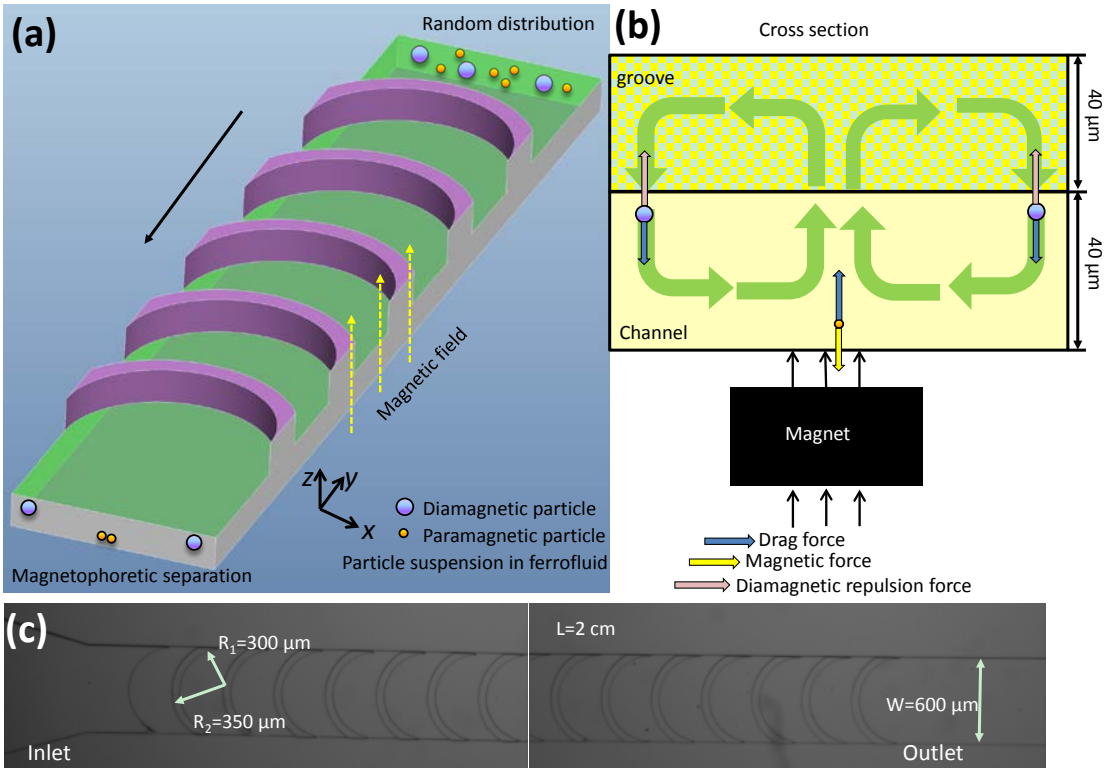

Figure 7-1 A microfluidic device for separating magnetic and non-magnetic particles. (a) Schematic showing the structure of this device and the spatial distributions of particles. The magnetic particles migrate to the centreline of the channel, while non-magnetic particles are focused onto the sidewalls. (b) The cross-sectional force diagram and equilibrium locations of particles in a microchannel patterned with grooves on its ceiling. (c) Optical micrograph images of the groove-based channel.

7.2.3. Material preparation

The SPHERO™ carboxyl magnetic microbeads (6 µm in diameter) were prepared in the DI water at a final concentration of 500 beads per microlitre. For separation experiments, a commercial water-based magnetite ferrofluid (EMG 408, Ferrotec Co., NH) was used. The volume ratio of the magnetite particles for this ferrofluid is 1.1%. The mean diameter of nanoparticles is 10.2 nm. The polystyrene particles with a diameter of 13 µm were purchased from Thermo Fisher Scientific Corporation. The 6 µm magnetic beads and 13 µm non-magnetic particles were re-suspended in ×0.05

EMG 408 ferrofluid to a final concentration of a million particles per millilitre. The magnetic susceptibilities of magnetic (χ_{p1}) and non-magnetic (χ_{p2}) beads were 2 and -8.2×10^{-6}, respectively. The magnetic susceptibilities of water and ×0.05 ferrofluid were -9.1×10^{-6} and 1.1×10^{-3}.

Prior to each experiment, the device was rinsed with DI water at 20 µl min^{-1} for 20 min using a syringe pump. To prevent immediate particle adhesion to the PDMS surface, 0.1% Tween 20 in DI water was injected into the microchannel and incubated at 37 ºC for 30 min to coat the PDMS surface.

7.2.4. Experimental setup

A non-uniform magnetic field was generated by a stack of two NdFeB permanent magnets. A syringe pump (Legato 100, Kd Scientific) was used to inject the particle suspension into the micro-channel. All images were captured through an inverted microscope (CKX41, Olympus, Japan) with a CCD camera (Rolera Bolt, Q-imaging, Australia) and an image processing program (Q-Capture Pro 7, Q-imaging, Australia). For separation experiments, 50 consecutive images were captured at a time interval of 10ms for each experiment. The images were then analysed by the MATLAB software (Mathworks, Australia) to measure the transverse particle positions at the channel outlet, which were then used to calculate the probability distribution function (PDF). More than 500 events were counted for each type of particles.

7.2.5. The effect of gravity on the particle focusing

For those non-magnetic particles, the density is 1.05 g cm^{-3}, which is similar to the medium (~1 g cm^{-3}). Therefore, the gravity effect on the non-magnetic particle focusing is negligible. However, the density of the magnetic particles is 1.4 g cm^{-3}, which is a big difference with the medium. In *z*-axis, the resultant force of buoyant and gravitational

forces is $F=4\pi R^3(\rho_p-\rho_m)g/3$= 0.45pN. The magnetic force applied on a magnetic particle is calculated as 284pN according to Eq.6-2. Therefore, the gravity effect on the movement of magnetic particles can also be neglected in this study.

7.3. Results and discussion

Since arranging a set of two NdFeB magnets under the microchannel will block any view of the inverted microscope, the chip is flipped so that the magnets can be placed on top of the glass side (Figure 7-2a). The particle suspension flows through the channel via lateral ports, while the fabrication of these lateral fluidic ports was reported in our previous work [92]. This device is called a "flipped" setup and consists of magnets, glass, and PDMS with a groove-based channel, from top to bottom (Figure 7-2b). The magnetic beads evenly distributed in the inlet are gradually focused at the centreline of the channel by a balance of magnetic force and drag force.

To verify that the magnetic beads are focusing in the groove-based channel, with help from the magnetic field, the magnetic beads suspended in DI water were injected into the channel. Figure 7-2c shows the particle trajectories of 6 μm magnetic beads captured at a flow rate of 1 μl min^{-1}. Regardless of their original positions, all the beads were focused on the centreline of the channel. The magnetic force then attracted the magnetic beads to the top of the channel, where drag forces gradually forced the beads into a single line moving in a lateral direction. The effect that the flow rate had on particle focusing was further studied with a flow rate ranging from 1 to 100 μl min^{-1}. The Reynolds number for 6 μm magnetic beads at a maximum flow rate was 0.03. Under the present experimental conditions, the inertial effect of particles can be omitted.

Figure 7-2d shows the bright-field microscopy of magnetic beads focused in the groove-based channel under various flow rates. The focusing performance is quantified by introducing the focusing efficiency as [42]: $E_n=(w-d/2-a)/(w-d)$, where a represents the width of the focused particle stream. The focusing efficiency *versus* flow rate is plotted and presented in Figure 7-2e. Focusing efficiency increased (>95%) when the flow rate is less than 30 μl min^{-1}, but focusing efficiency decreased from 92.0±2.9% to 87.1±3.6% when the flow rate increased from 50 to 100 μl min^{-1}. As Hsu *et al*. [199] reported, the drag force in the cross section is linearly proportional to the inlet flow rate

for all Re<2, and although the drag force in the cross section decreases at a lower flow rate, the longer retention time in the channel enables the beads to move to the centreline of the channel. However, a larger drag force is induced as the inlet flow rate increases, but the exposure time to the magnetic field is not enough to attract the beads to the top of the channel, and this leads to a slight drop in focusing efficiency.

Despite the focusing efficiency decreasing slightly as the flow rate increases, focusing efficiency remains around 85% at a maximum flow rate of 100 µl min^{-1}. These higher focusing efficiencies and the wider flow rate range are key parameters for successful separation in the next step. Flow-rate insensitivity is a dispensable characteristic in developing hand-held microfluidic devices where an accurate pumping system is not required. For example, a fluidic sample can be manually introduced into chips via pipettes or syringes. A microfluidic device with an independent flow rate can still achieve good separation or focusing performance, even with a manually operated flow rate that fluctuates and is unstable.

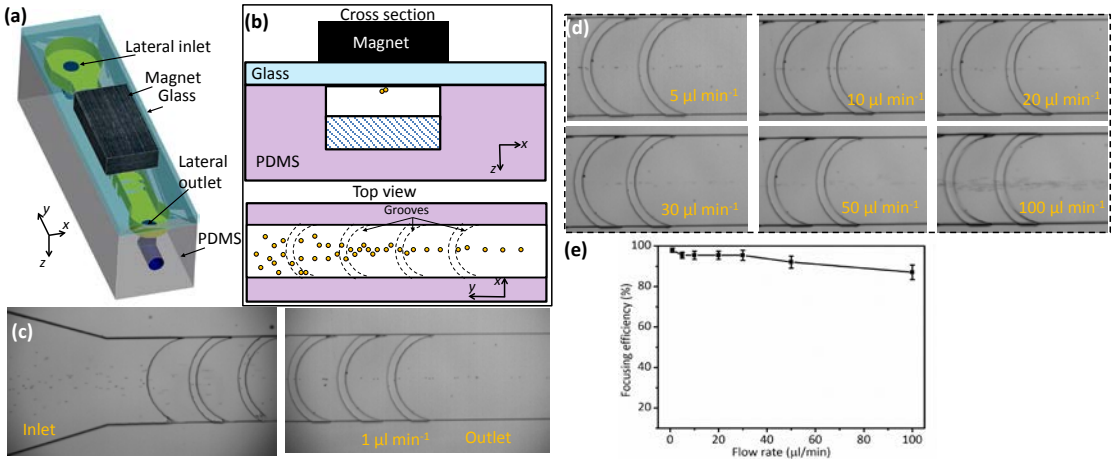

Figure 7-2 (a) A three-dimensional animated model with an overview of the "flipped" setup. (b) Cross section (top) and top view (bottom) show that the magnetic beads are gradually focused due to positive magnetophoresis and microvortices. (c) The micrographic images showing the particle trajectories at the inlet (left) and outlet (right) at a flow rate of 1 µl min^{-1}. (d) Optical micrographs showing the particle trajectories at the channel outlet at the flow rate of 5, 10, 20, 30, 50 and 100 µl min^{-1}. (e) The measured focusing efficiency of the magnetic beads. The average value was 3 times the measurement and the error bar represents standard deviation.

Interestingly, magnetic beads in the “regular” setup have a distinct movement such that a glass slide is placed on the stage of the microscope and the magnets are on top of the PDMS replica (Figure 7-3a). Similarly, magnetic beads are attracted to the magnetic source (*i.e*. the upper level of the channel), where they focus onto the sidewalls of the channel due to hydrophoretic self-ordering (Figure 7-3b). Hydrophoresis has a steric hindrance mechanism which separates or focuses particles or cells under a pressure gradient induced by the grooves [27], so those particles with diameters larger than half the height of the channel will be dominated by steric hindrance and form hydrophoretic ordering. We recently found that particle-groove interaction enables particle focusing [47], and these intense particle-groove interactions are achieved by levitating the particles towards the grooves using electric [112] and magnetic fields [92], even though the particles do not satisfy the criterion of hydrophoretic ordering. In this “regular” setup, those magnetic beads that are evenly released are gradually focused onto the sidewalls of the channel by a combination of positive magnetophoresis and hydrophoresis.

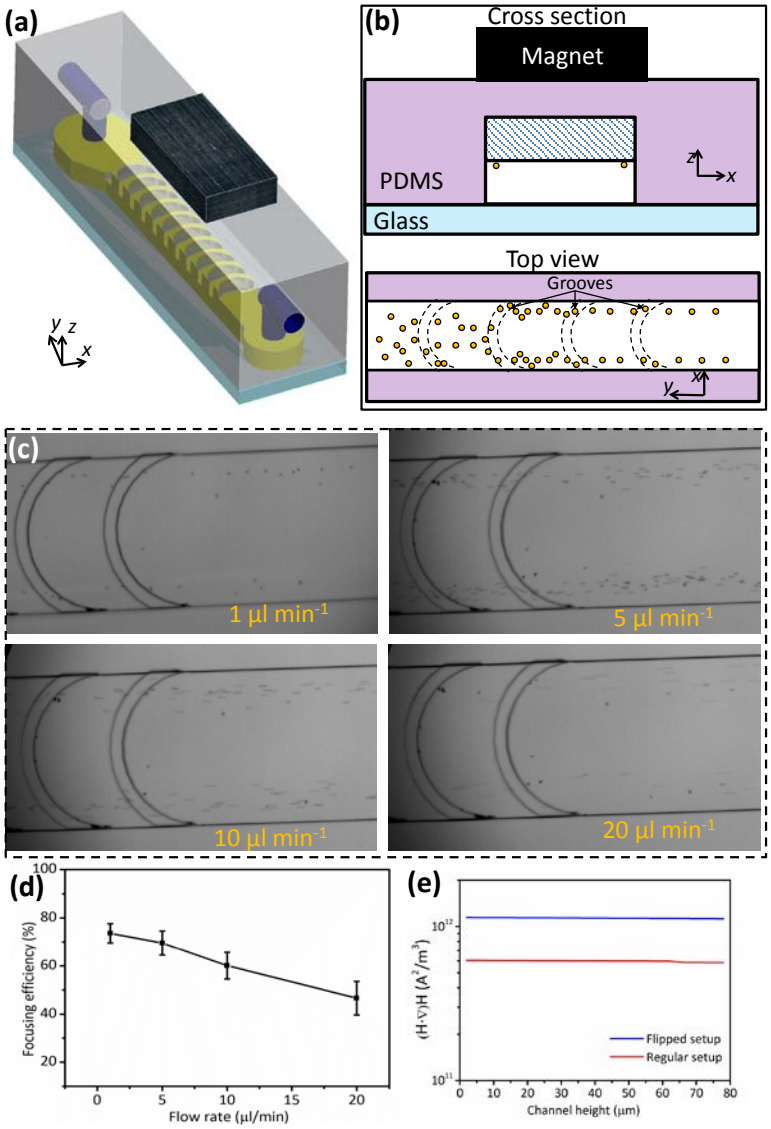

Figure 7-3(a) An overview of the "regular" setup. (b) The cross section (top) and top view (bottom) show that the magnetic beads are gradually focused onto the sidewalls of the channel by a combination of positive magnetophoresis and hydrophoresis. (c) Optical micrographs showing the particle trajectories at the outlet at the flow rate of 1, 5, 10 and 20 µl min^{-1}. (d) The focusing efficiency of the magnetic beads measured in the "regular" setup. The average value was 3 times the measurement and the error bar represents standard deviation. (e) The plot of the calculated gradients of the square of the magnetic field in different setups.

Figure 7-3c shows the focusing patterns of 6 µm magnetic beads at the outlet in a "regular" setup where the flow rates vary from 1 to 20 µl min^{-1}. Figure 7-3d shows the

focusing efficiency under different working conditions; in the “regular” setup the focusing efficiency is similar to the “flipped” setup and on which the flow rate has an adverse effect. The focusing efficiency in this “regular” setup dropped from 73.5 ± 4.1% to 46.6 ± 6.8% as the flow rate increased from 1 to 20 µl min^{-1}. This shorter retention time for the beads passing through the channel is one reason for this phenomenon because at a higher flow rate the magnetic beads do not have enough time to migrate towards the grooves under a magnetic field, and thus their focusing performance is poor.

The biggest difference between these two setups lies in the magnitude of the magnetic fields. The distance between the channel and the magnets was 1 mm (*i.e*. the thickness of the glass side) in the “flipped” setup, whereas this value increased to ~3 mm (the thickness of PDMS) when the magnets were placed on top of the PDMS in the “regular” setup (Figure 7-3b). To study this magnetic field that decreases as the distance increases, a 2D model was built to simulate how the magnetic field is distributed. Based on this model, the gradients of the square of the magnetic field along the height of the channel at different setups were calculated numerically (Figure 7-3e). The average intensity of the magnetic field gradient in the “flipped” setup was ~2 times as high as in the “regular” setup, and therefore the beads experiencing a weaker magnetic force in the “regular” setup were prone to have less focusing efficiency.

The good focusing performance in the “flipped” setup meant that this setup was used for the magnetophoretic separation of magnetic and non-magnetic particles. To create the differences in magnetic susceptibility, 6 µm magnetic beads and 13 µm polystyrene particles were suspended in the ×0.05 ferrofluid. This particle-laden sample was then injected into the micro-channel with a flow rate that varied from 5 to 80 µl min^{-1}, to examine how this variable flow rate affected particle separation. The transverse positions for each type of particle at the outlet were measured statistically as a probability distribution function (PDF) [200]. More than 500 events were counted for each type of particles.

Figure 7-4a shows that the magnetic beads focused to a stream near the centreline of the channel by balancing the magnetic force and drag force, while the non-magnetic beads moved along the sidewalls of the channel in a combination of hydrophoresis and

negative magnetophoresis. Because the equilibrium positions in the groove-based channel are distinct, those particles with different magnetic properties become widely separated. The PDF of magnetic beads in a diluted ferrofluid do not change very often as the flow rate increases (Figure 7-4b), a result that is identical to the results reported above. Since the flow rate caused the hydrophoretic focusing to deteriorate, as reported in our previous work [47], the non-magnetic beads tended towards having a wider distribution at the outlet at a higher flow rate (Figure 7-4b), whereas the magnetic beads were clearly separated from the non-magnetic beads because the magnetic and non-magnetic beads did not overlap with each other, even at a higher flow rate. The throughput capacity demonstrated in this work was 1667 particles s^{-1}.

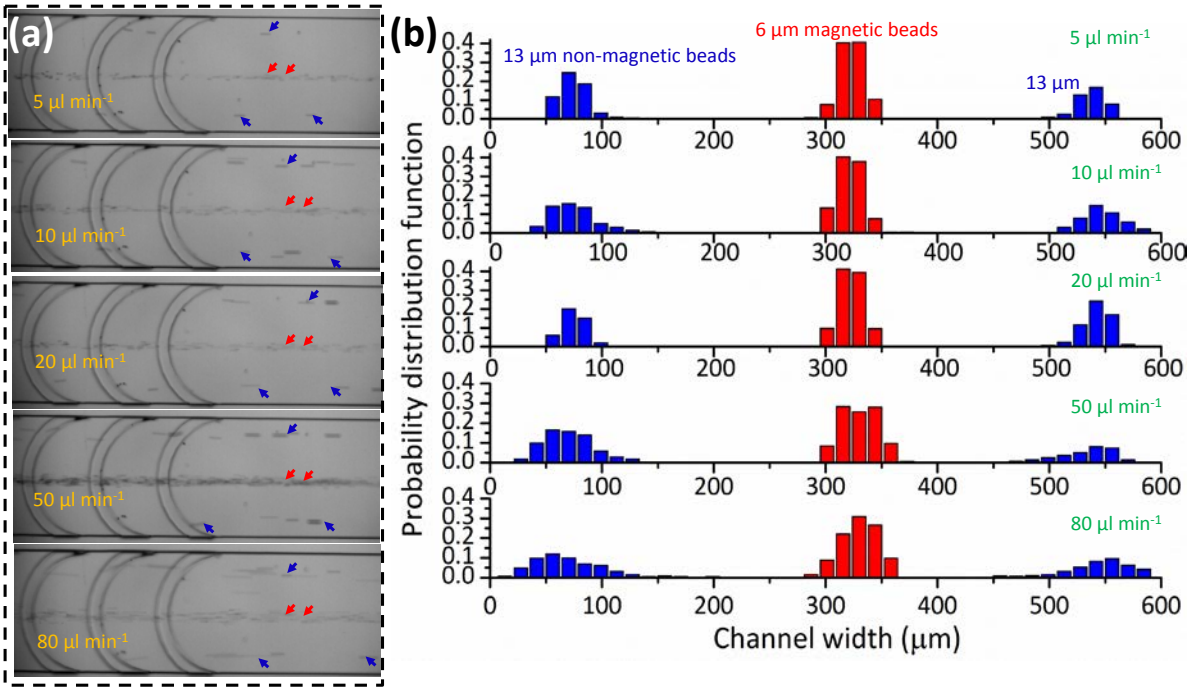

Figure 7-4 (a) The effect that flow rate has on the separation of magnetic and non-magnetic beads in the "flipped" setup. The red arrows point to the 6 µm magnetic beads, while the blue ones highlight the 13 µm non-magnetic beads. (b) A plot of particle PDF at the channel outlet. More than 500 events were counted for each type of particle.

Although the flow rates in this work are less than 100 µl min^{-1}, throughput can be improved by increasing the width of the channel because the focusing mechanism for the magnetic and non-magnetic beads is related to the height of the channel. Alternatively, integrating N columns of grooves into a single chip can create $2N+1$

parallel focused streams of particles (Figure 7-5); this is an easy and very efficient way to improve the throughput of the channel. Another method is to parallelise the microfluidic devices that require the PDMS layers [201] to be stacked because the device with multiple columns of grooves has a simpler structure due to having a single inlet and a single layer of PDMS.

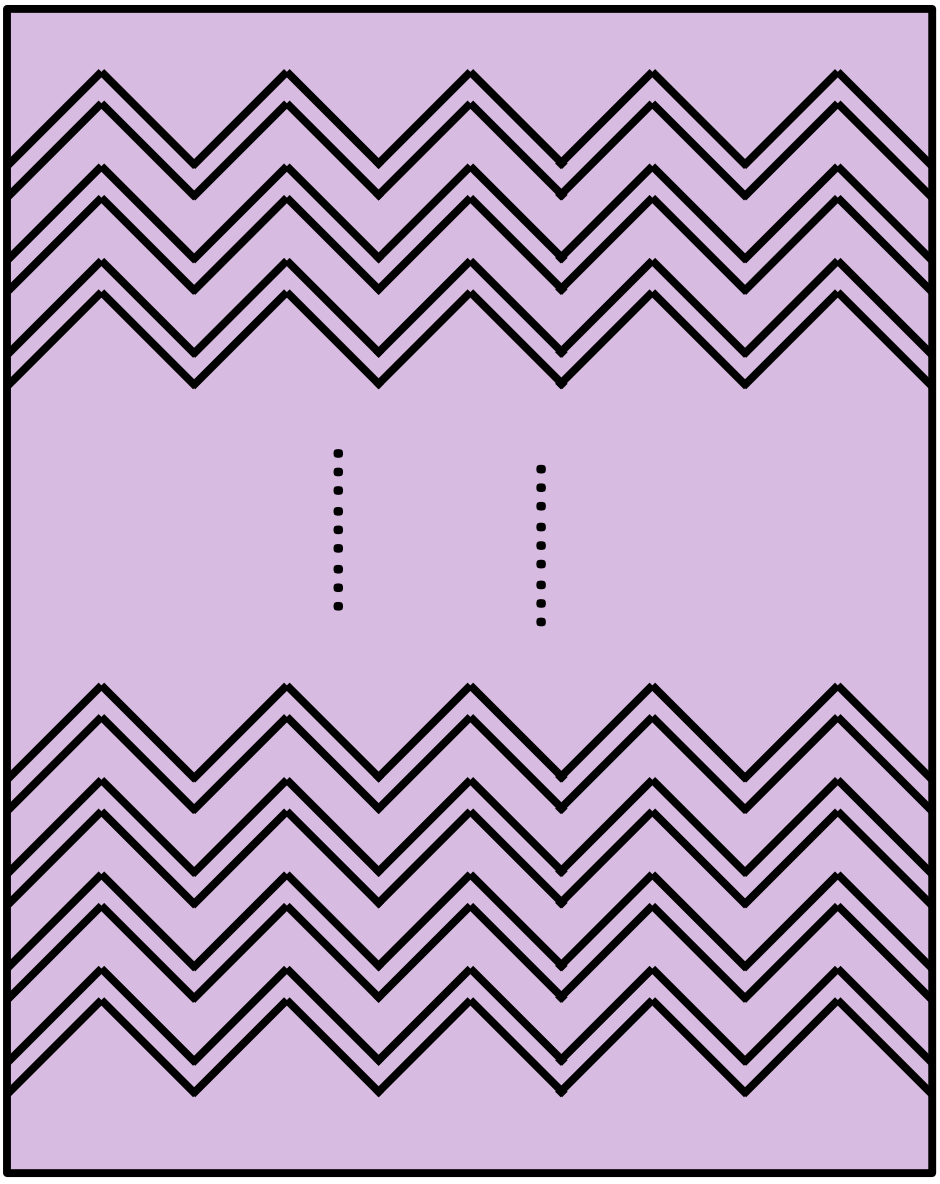

Figure 7-5 Schematic of microfluidic channel with multiple columns of grooves.

7.4. Conclusion

In summary, we have now demonstrated a high-throughput, sheathless, magnetophoretic separation of magnetic and non-magnetic beads in a groove-based channel. It has also been found that magnetic beads have different particle trajectories in different setups. For example, in the “flipped” setup, the magnetic beads were focused onto the centreline of the channel and retained a high focusing efficiency (~85%) at a flow rate of ~100 μl min^{-1}; in fact the focusing efficiency is insensitive to the flow rate so this device can be operated manually; whereas the magnetic beads in the “regular” setup formed hydrophoretic ordering due to positive magnetophoresis and focused onto the sidewalls of the channel. Finally, the magnetic and non-magnetic beads were suspended in a diluted ferrofluid to generate the mismatch of magnetic susceptibility. This separation was achieved in the “flipped” setup where the magnetic beads stayed near the centreline of the channel by balancing the magnetic force and drag force, and the non-magnetic beads moved along the sidewalls of the channel due to hydrophoresis and negative magnetophoresis. The particle distribution at the outlet revealed a clear separation between the magnetic and non-magnetic particles, even at a flow rate of μl min^{-1}. Furthermore, the throughput of the groove-based channel can be enhanced considerably by integrating multiple columns of grooves into a single chip for parallel processing.

8. Conclusion and future work

8.1. Conclusion

The main objective of this research is to develop tunable hydrophoresis using hybrid techniques for particle focusing and separation. The hydrophoresis was tuned by two different mechanisms:

(i) The particles experiencing DEP force were pushed to the higher level of the channel, where the particle-groove interaction enables the hydrophoretic ordering occur.

(ii) Negative MP was employed to assisted the hydrophoretic ordering in a diluted ferrofluid.

8.1.1. DEP-assisted hydrophoresis

A new concept of DEP-assisted hydrophoresis was proposed. This microfluidic device consisted of anisotropic microstructures embedded on the top of the channel which generates lateral pressure gradients while interdigitated electrodes lay on the bottom of the channel which can push particles or cells into a higher level using negative DEP force. The polystyrene particles and MEL cells were used to test the effectiveness of the DEP-assisted hydrophoretic device. High throughput was achieved (maximum flow rate ~150 μL min^{-1}) with good focusing performance. The focusing patterns were modulated by varying the voltage and flow rate.

The DEP-assisted hydrophoretic device was further used for plasma isolation. By reducing the flow velocity and increasing the DEP voltage, both large and small particles or cells (3 μm and 10 μm particles, and red blood cells, white blood cells, and platelets) were focused simultaneously in our DEP-assisted hydrophoretic device, which enabled all the blood cells to separate from the blood and obtain plasma. Based on this principle, all the blood cells were filtrated from whole blood and then plasma was extracted with a purity of 94.2% and a yield of 16.5% at a flow rate of 10 μL min^{-1}.

To extend the DEP-assisted hydrophoresis to particle separation, a modular microfluidics was developed, which consisted of the pre-focusing region and sorting region. Particles or cells were focused in the pre-focusing region and then sorted in the

sorting region. For size-selective separation, the 3 μm and 10 μm beads were separated with a separation efficiency of 95.7 and 96.6. According to the different dielectric property of viable and nonviable CHO cells, the viable CHO cells were sorted with a high purity of 99.6%. To achieve dual function, the microposts were embedded into the DEP-assisted hydrophoretic channel. The filtration or separation mode was switched by altering the power supply voltages.

8.1.2. MP-assisted hydrophoresis

Since the DEP-assisted hydrophoresis requires a power supply, the bulk peripheral equipment limited the tunable hydrophoresis to be miniaturised. Therefore, a MP-assisted hydrophoresis was developed, which employed the hand-held permanent magnets to modulate the particle trajectories in a diluted ferrofluid. Diamagnetic particles suspended in a ferrofluidic medium were repelled to the vicinity of the grooves by negative magnetophoretic force and then interact with grooves to obtain an excellent hydrophoretic ordering. The focusing patterns of particles were tuned by varying the flow rate, ferrofluidic concentration, and numbers of the magnet. Furthermore, the magnetic and non-magnetic beads were separated using MP-assisted hydrophoresis. This separation was achieved in the “flipped” setup where the magnetic beads stayed near the centreline of the channel by balancing the magnetic force and drag force, and the non-magnetic beads moved along the sidewalls of the channel due to hydrophoresis and negative magnetophoresis.

In summary, our study does not only focus on the development of tunable hydrophoretic devices, but also provide versatile and effective chips for cell processing, including isolation of plasma and separation of viable and non-viable cells.

8.2. Future work

8.2.1. Isolation of magnetic bead-conjugated monocytes from the white blood cell subpopulations in the hydrophoretic channel

Monocytes play a significant role in the human immune system and protect the host from the invasion of bacteria, viruses, and parasites. Isolation of highly purified monocytes has an important application in immunological research such as

investigation of infectious diseases. However, the biggest challenge to separate monocytes is that the monocytes have the similar size with other subpopulations of peripheral white blood cells such as lymphocytes and polymorphonuclear cells. This work will conjugate monocytes with magnetic beads for deterministic separation from other subpopulations in the hydrophoretic channel. The magnetic bead-labelled monocytes experiencing positive magnetophoresis will be focused near the centreline of the channel (Figure 7-1 b). Non-tagged white blood cells in a hydrophoretic channel with the height of 20 μm will form hydrophoretic ordering and focus onto the sidewalls of the channel. Therefore, the monocytes will be separated for the downstream analysis.

8.2.2. Continuous enrichment of circulating tumour cells from undiluted blood in a groove-based channel

Cancer metastasis is responsible for approximately 90% of cancer-related deaths, causing by circulating tumour cells (CTCs) [113]. Because extracting blood from cancer patients is a clinically non-invasive mean, CTCs potentially act as biomarkers for prognosis, evaluation of treatment efficacy and studying molecular alterations under therapy [115, 116]. This work will demonstrate to employ the cell-cell interactions and secondary flows generated in a groove-based channel for CTCs enrichment.

A schematic of the device is shown in Figure 8-1a. The fluid inside the channel is altered by the anisotropic grooves and secondary flows are induced in the cross section (Figure 8-1b). On the other hand, the grooves also provide the expansions/contractions in the vertical direction. When RBCs move upwards and “invade” the grooves, the homotypic adhesion of RBCs is dynamically activated with the decrease of shear stresses in expansions, forcing CTCs to move downwards and keep out of grooves. Finally, the CTCs are driven to the right sidewall of the channel by the secondary flow (Figure 8-1 b,c). The CTCs are then filtered using a 2-outlet system, thus achieving a continuous CTCs enrichment from an undiluted blood sample.

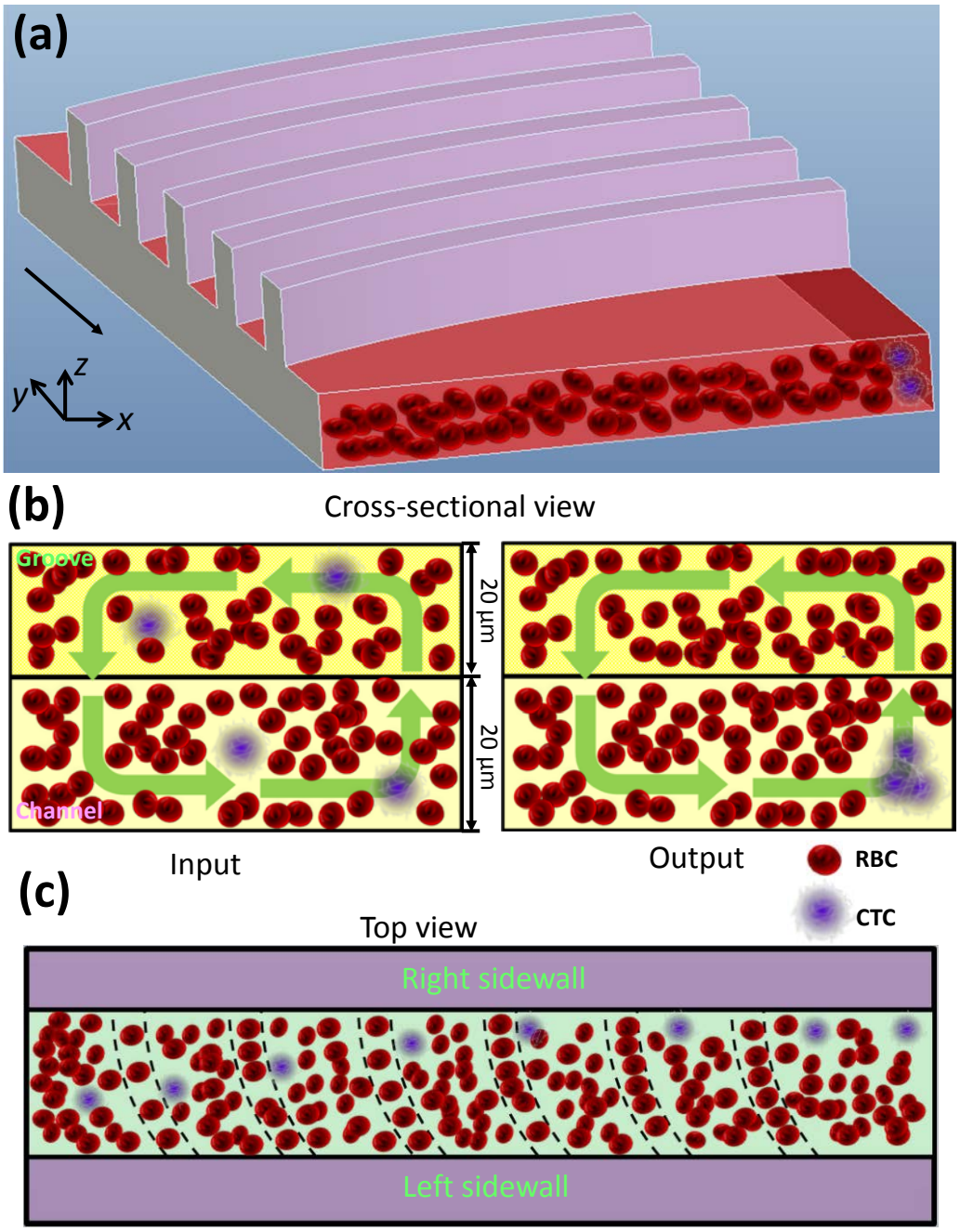

Figure 8-1 A CTCs enrichment device. (a) Schematic showing the structure of this device and the spatial distributions of cells. Cross-sectional (b) and top (c) view of the channel illustrating the filtration process. The CTCs migrate to the right sidewall of the channel, while RBCs are evenly distributed in the channel.

References

1. Figeys, D., and Pinto, D. (2000) Lab-on-a-chip: A revolution in biological and medical sciences, *Anal. Chem. 72*, 330A-335A.

2. Carbonaro, A., and Sohn, L. L. (2005) A resistive-pulse sensor chip for multianalyte immunoassays, *Lab Chip 5*, 1155-1160.

3. Ateya, D. A., Sachs, F., Gottlieb, P. A., Besch, S., and Hua, S. Z. (2005) Volume cytometry: Microfluidic sensor for high-throughput screening in real time, *Anal. Chem. 77*, 1290-1294.

4. Choi, S., Song, S., Choi, C., and Park, J. K. (2008) Sheathless focusing of microbeads and blood cells based on hydrophoresis, *Small 4*, 634-641.

5. Sun, J., Gao, Y., Isaacs, R. J., Boelte, K. C., Charles Lin, P., Boczko, E. M., and Li, D. (2012) Simultaneous on-chip DC dielectrophoretic cell separation and quantitative separation performance characterization, *Anal. Chem. 84*, 2017-2024.

6. Shi, J., Mao, X., Ahmed, D., Colletti, A., and Huang, T. J. (2008) Focusing microparticles in a microfluidic channel with standing surface acoustic waves (SSAW), *Lab Chip 8*, 221-223.

7. Liu, C., Stakenborg, T., Peeters, S., and Lagae, L. (2009) Cell manipulation with magnetic particles toward microfluidic cytometry, *J. Appl. Phys. 105*.

8. Ai, Y., Mauroy, B., Sharma, A., and Qian, S. (2011) Electrokinetic motion of a deformable particle: Dielectrophoretic effect, *Electrophoresis 32*, 2282-2291.

9. Yu, C. H., Vykoukal, J., Vykoukal, D. M., Schwartz, J. A., Shi, L., and Gascoyne, P. R. C. (2005) A three-dimensional dielectrophoretic particle focusing channel for microcytometry applications, *J. Microelectromech. S. 14*, 480-487.

10. Holmes, D., Morgan, H., and Green, N. G. (2006) High throughput particle analysis: Combining dielectrophoretic particle focussing with confocal optical detection, *Biosens. Bioelectron. 21*, 1621-1630.

11. Cheng, I. F., Chang, H.-C., Hou, D., and Chang, H.-C. (2007) An integrated dielectrophoretic chip for continuous bioparticle filtering, focusing, sorting, trapping, and detecting, *Biomicrofluid. 1*.

12. Demierre, N., Braschler, T., Muller, R., and Renaud, P. (2008) Focusing and continuous separation of cells in a microfluidic device using lateral dielectrophoresis, *Sensor. Actuat. B: Chem. 132*, 388-396.

13. Cummings, E. B., and Singh, A. K. (2003) Dielectrophoresis in microchips containing arrays of insulating posts: Theoretical and experimental results, *Anal. Chem. 75*, 4724-4731.

14. Thwar, P. K., Linderman, J. J., and Burns, M. A. (2007) Electrodeless direct current dielectrophoresis using reconfigurable field-shaping oil barriers, *Electrophoresis 28*, 4572-4581.

15. Zhu, J., and Xuan, X. (2009) Dielectrophoretic focusing of particles in a microchannel constriction using DC-biased AC flectric fields, *Electrophoresis 30*, 2668-2675.

16. Zhu, J., Tzeng, T.-R. J., Hu, G., and Xuan, X. (2009) DC dielectrophoretic focusing of particles in a serpentine microchannel, *Microfluid. Nanofluid. 7*, 751-756.

17. Church, C., Zhu, J., Nieto, J., Keten, G., Ibarra, E., and Xuan, X. (2010) Continuous particle separation in a serpentine microchannel via negative and positive dielectrophoretic focusing, *J. Micromech.Microeng. 20*.

18. Zhu, J., and Xuan, X. (2009) Particle electrophoresis and dielectrophoresis in curved microchannels, *J. Colloid Interface Sci. 340*, 285-290.

19. Li, M., Li, S., Cao, W., Li, W., and Wen, W. (2012) Continuous particle focusing in a waved microchannel using negative dc dielectrophoresis, *J. Micromech.Microeng. 22*, 095001.

20. Lee, G. B., Chang, C. C., Huang, S. B., and Yang, R. J. (2006) The hydrodynamic focusing effect inside rectangular microchannels, *J. Micromech.Microeng. 16*, 1024-1032.

21. Chang, C. C., Huang, Z. X., and Yang, R. J. (2007) Three-dimensional hydrodynamic focusing in two-layer polydimethylsiloxane (PDMS) microchannels, *J. Micromech.Microeng. 17*, 1479-1486.

22. Tsai, C. H., Hou, H. H., and Fu, L. M. (2008) An optimal three-dimensional focusing technique for micro-flow cytometers, *Microfluid. Nanofluid. 5*, 827-836.

23. Kummrow, A., Theisen, J., Frankowski, M., Tuchscheerer, A., Yildirim, H., Brattke, K., Schmidt, M., and Neukammer, J. (2009) Microfluidic structures for flow cytometric analysis of hydrodynamically focussed blood cells fabricated by ultraprecision micromachining, *Lab Chip 9*, 972-981.

24. Di Carlo, D. (2009) Inertial microfluidics, *Lab Chip 9*, 3038-3046.

25. Choi, S., and Park, J.-K. (2008) Sheathless Hydrophoretic Particle Focusing in a Microchannel with Exponentially Increasing Obstacle Arrays, *Anal. Chem. 80*, 3035-3039.

26. Choi, S. (2009) Hydrophoretic Sorting of Micrometer and Submicrometer Particles Using Anisotropic Microfluidic Obstacles, *Anal. Chem. 81*, 50-55.

27. Choi, S., and Park, J.-K. (2007) Continuous hydrophoretic separation and sizing of microparticles using slanted obstacles in a microchannel, *Lab Chip 7*, 890-897.

28. Choi, S., and Park, J.-K. (2009) Tuneable hydrophoretic separation using elastic deformation of poly(dimethylsiloxane), *Lab Chip 9*, 1962-1965.

29. Song, S., and Choi, S. (2013) Design rules for size-based cell sorting and sheathless cell focusing by hydrophoresis, *J. Chromatogr. A 1302*, 191-196.

30. Zheng, Y., Nguyen, J., Wei, Y., and Sun, Y. (2013) Recent advances in microfluidic techniques for single-cell biophysical characterization, *Lab Chip 13*, 2464-2483.

31. Beech, J. P., Jonsson, P., and Tegenfeldt, J. O. (2009) Tipping the balance of deterministic lateral displacement devices using dielectrophoresis, *Lab Chip 9*, 2698-2706.

32. Choi, S., Song, S., Choi, C., and Park, J.-K. (2009) Hydrophoretic Sorting of Micrometer and Submicrometer Particles Using Anisotropic Microfluidic Obstacles, *Anal. Chem. 81*, 50-55.

33. Davis, J. A., Inglis, D. W., Morton, K. J., Lawrence, D. A., Huang, L. R., Chou, S. Y., Sturm, J. C., and Austin, R. H. (2006) Deterministic hydrodynamics: Taking blood apart, *Proc. Natl. Acad. Sci. U. S. A. 103*, 14779-14784.

34. Kersaudy-Kerhoas, M., and Sollier, E. (2013) Micro-scale blood plasma separation: From acoustophoresis to egg-beaters, *Lab Chip 13*, 3323-3346.

35. Choi, S., Ku, T., Song, S., Choi, C., and Park, J.-K. (2011) Hydrophoretic high-throughput selection of platelets in physiological shear-stress range, *Lab Chip 11*, 413-418.

36. Choi, S., Song, S., Choi, C., and Park, J.-K. (2007) Continuous blood cell separation by hydrophoretic filtration, *Lab Chip 7*, 1532-1538.

37. Nagrath, S., Sequist, L. V., Maheswaran, S., Bell, D. W., Irimia, D., Ulkus, L., Smith, M. R., Kwak, E. L., Digumarthy, S., and Muzikansky, A. (2007) Isolation of rare circulating tumour cells in cancer patients by microchip technology, *Nature 450*, 1235-1239.

38. Choi, S., Karp, J. M., and Karnik, R. (2012) Cell sorting by deterministic cell rolling, *Lab Chip*.

39. Metreau, J. M., Gallet, S., Cardot, P. J. P., Maire, V. L., Dumas, F., Hernvann, A., and Loric, S. (1997) Sedimentation Field-Flow Fractionation of Cellular Species, *Anal. Biochem. 251*, 178-186.

40. Battu, S., Roux, A., Delebasee, S., Bosgiraud, C., and Cardot, P. J. P. (2001) Sedimentation field-flow fractionation device cleaning, decontamination and sterilization procedures for cellular analysis, *Journal of Chromatography B: Biomedical Sciences and Applications 751*, 131-141.

41. Choi, S. (2009) Optically Coated Mirror-Embedded Microchannel to Measure Hydrophoretic Particle Ordering in Three Dimensions, *Small (Weinheim an der Bergstrasse, Germany) 5*, 2205-2211.

42. Choi, S., and Park, J. K. (2008) Sheathless hydrophoretic particle focusing in a microchannel with exponentially increasing obstacle arrays, *Anal. Chem. 80*, 3035-3039.

43. Jones, T. B. (1995) *Electromechanics of Particles*, Cambridge Unviersity Press, Cambridge.

44. Tang, S. Y., Zhang, W., Baratchi, S., Nasabi, M., Kalantar-Zadeh, K., and Khoshmanesh, K. (2013) Modifying dielectrophoretic response of nonviable yeast cells by ionic surfactant treatment, *Anal. Chem. 85*, 6364-6371.

45. Huang, L. R., Cox, E. C., Austin, R. H., and Sturm, J. C. (2004) Continuous particle separation through deterministic lateral displacement, *Science 304*, 987-990.

46. Chang, S., and Cho, Y.-H. (2008) A continuous size-dependent particle separator using a negative dielectrophoretic virtual pillar array, *Lab Chip 8*, 1930-1936.

47. Yan, S., Zhang, J., Li, M., Alici, G., Du, H., Sluyter, R., and Li, W. (2014) On-chip high-throughput manipulation of particles in a dielectrophoresis-active hydrophoretic focuser, *Sci. Rep. 4*, 5060.

48. Yan, S., Zhang, J., Yuan, Y., Lovrecz, G., Alici, G., Du, H., Zhu, Y., and Li, W. (2015) A hybrid dielectrophoretic and hydrophoretic microchip for particle sorting using integrated prefocusing and sorting steps, *Electrophoresis 36*, 284-291.

49. Lee, M. G., Choi, S., Kim, H. J., Lim, H. K., Kim, J. H., Huh, N., and Park, J. K. (2011) Inertial blood plasma separation in a contraction–expansion array microchannel, *Appl. Phys. Lett. 98*, 253702.

50. Zhang, J., Yan, S., Li, W., Alici, G., and Nguyen, N.-T. (2014) High throughput extraction of plasma using a secondary flow-aided inertial microfluidic device, *RSC Advances 4*, 33149-33159.

51. Warkiani, M. E., Tay, A. K. P., Guan, G., and Han, J. (2015) Membrane-less microfiltration using inertial microfluidics, *Sci. Rep. 5*, Art No. 11018

52. Zhang, J., Yan, S., Sluyter, R., Li, W., Alici, G., and Nguyen, N.-T. (2014) Inertial particle separation by differential equilibrium positions in a symmetrical serpentine micro-channel, *Sci. Rep. 4*, Art No. 4527.

53. Lee, M. G., Choi, S., and Park, J. K. (2011) Inertial separation in a contraction–expansion array microchannel, *J. Chromatogr. A 1218*, 4138-4143.

54. Kuntaegowdanahalli, S. S., Bhagat, A. A. S., Kumar, G., and Papautsky, I. (2009) Inertial microfluidics for continuous particle separation in spiral microchannels, *Lab Chip 9*, 2973-2980.

55. Wu, L., Guan, G., Hou, H. W., Bhagat, A. A. S., and Han, J. (2012) Separation of Leukocytes from Blood Using Spiral Channel with Trapezoid Cross-Section, *Anal. Chem. 84*, 9324-9331.

56. Sollier, E., Amini, H., Go, D., Sandoz, P., Owsley, K., and Di Carlo, D. (2015) Inertial microfluidic programming of microparticle-laden flows for solution transfer around cells and particles, *Microfluid. Nanofluid.*, 1-13.

57. Dudani, J. S., Gossett, D. R., Henry, T., Lamm, R. J., Kulkarni, R. P., and Di Carlo, D. (2015) Rapid inertial solution exchange for enrichment and flow cytometric detection of microvesicles, *Biomicrofluid 9*, 014112.

58. Gossett, D. R., Tse, H. T. K., Dudani, J. S., Goda, K., Woods, T. A., Graves, S. W., and Di Carlo, D. (2012) Inertial manipulation and transfer of microparticles across laminar fluid streams, *Small 8*, 2757-2764.

59. Martel, J. M., Smith, K. C., Dlamini, M., Pletcher, K., Yang, J., Karabacak, M., Haber, D. A., Kapur, R., and Toner, M. (2015) Continuous Flow Microfluidic Bioparticle Concentrator, *Sci. Rep. 5*, Art NO. 11300.

60. Sollier, E., Go, D. E., Che, J., Gossett, D. R., O'Byrne, S., Weaver, W. M., Kummer, N., Rettig, M., Goldman, J., and Nickols, N. (2014) Size-selective collection of circulating tumor cells using Vortex technology, *Lab Chip 14*, 63-77.

61. Che, J., Mach, A. J., Go, D. E., Talati, I., Ying, Y., Rao, J., Kulkarni, R. P., and Di Carlo, D. (2013) Microfluidic purification and concentration of malignant pleural effusions for improved molecular and cytomorphological diagnostics, *PLoS One 8*, e78194.

62. Mach, A. J., Kim, J. H., Arshi, A., Hur, S. C., and Di Carlo, D. (2011) Automated cellular sample preparation using a Centrifuge-on-a-Chip, *Lab Chip 11*, 2827-2834.

63. Lee, M. G., Shin, J. H., Bae, C. Y., Choi, S., and Park, J.-K. (2013) Label-free cancer cell separation from human whole blood using inertial microfluidics at low shear stress, *Anal. Chem. 85*, 6213-6218.

64. Sun, J., Li, M., Liu, C., Zhang, Y., Liu, D., Liu, W., Hu, G., and Jiang, X. (2012) Double spiral microchannel for label-free tumor cell separation and enrichment, *Lab Chip 12*, 3952-3960.

65. Hou, H. W., Warkiani, M. E., Khoo, B. L., Li, Z. R., Soo, R. A., Tan, D. S.-W., Lim, W.-T., Han, J., Bhagat, A. A. S., and Lim, C. T. (2013) Isolation and retrieval of circulating tumor cells using centrifugal forces, *Sci. Rep. 3*, Art No. 1259.

66. Warkiani, M. E., Guan, G., Luan, K. B., Lee, W. C., Bhagat, A. A. S., Chaudhuri, P. K., Tan, D. S.-W., Lim, W. T., Lee, S. C., and Chen, P. C. (2014) Slanted spiral microfluidics for the ultra-fast, label-free isolation of circulating tumor cells, *Lab Chip 14*, 128-137.

67. Warkiani, M. E., Tay, A. K. P., Khoo, B. L., Xiaofeng, X., Han, J., and Lim, C. T. (2015) Malaria detection using inertial microfluidics, *Lab Chip 15*, 1101-1109.

68. Birch, C. M., Hou, H. W., Han, J., and Niles, J. C. (2015) Identification of malaria parasite-infected red blood cell surface aptamers by inertial microfluidic SELEX (I-SELEX), *Sci. Rep. 5*.

69. Lee, W. C., Bhagat, A. A. S., Huang, S., Van Vliet, K. J., Han, J., and Lim, C. T. (2011) High-throughput cell cycle synchronization using inertial forces in spiral microchannels, *Lab Chip 11*, 1359-1367.

70. Kemna, E. W., Schoeman, R. M., Wolbers, F., Vermes, I., Weitz, D. A., and van den Berg, A. (2012) High-yield cell ordering and deterministic cell-in-droplet encapsulation using Dean flow in a curved microchannel, *Lab Chip 12*, 2881-2887.

71. Gossett, D. R., Henry, T., Lee, S. A., Ying, Y., Lindgren, A. G., Yang, O. O., Rao, J., Clark, A. T., and Di Carlo, D. (2012) Hydrodynamic stretching of single cells for large population mechanical phenotyping, *Proc. Natl. Acad. Sci. U.S.A. 109*, 7630-7635.

72. Dudani, J. S., Gossett, D. R., Henry, T., and Di Carlo, D. (2013) Pinched-flow hydrodynamic stretching of single-cells, *Lab Chip 13*, 3728-3734.

73. Zhang, J., Yan, S., Yuan, D., Alici, G., Nguyen, N.-T., Warkiani, M. E., and Li, W. (2016) Fundamentals and applications of inertial microfluidics: a review, *Lab Chip 16*, 10-34.

74. Moon, H. S., Kwon, K., Kim, S. I., Han, H., Sohn, J., Lee, S., and Jung, H. I. (2011) Continuous separation of breast cancer cells from blood samples using multi-orifice flow fractionation (MOFF) and dielectrophoresis (DEP), *Lab Chip 11*, 1118-1125.

75. Zhang, J., Yan, S., Alici, G., Nguyen, N.-T., Di Carlo, D., and Li, W. (2014) Real-time control of inertial focusing in microfluidics using dielectrophoresis (DEP), *RSC Advances 4*, 62076-62085.

76. Gascoyne, P. R. C., Noshari, J., Anderson, T. J., and Becker, F. F. (2009) Isolation of rare cells from cell mixtures by dielectrophoresis, *Electrophoresis 30*, 1388-1398.

77. Gascoyne, P. R. C. (2009) Dielectrophoretic-Field Flow Fractionation Analysis of Dielectric, Density, and Deformability Characteristics of Cells and Particles, *Anal. Chem. 81*, 8878-8885.

78. Shim, S., Stemke-Hale, K., Tsimberidou, A. M., Noshari, J., Anderson, T. E., and Gascoyne, P. R. (2013) Antibody-independent isolation of circulating tumor cells by continuous-flow dielectrophoresis, *Biomicrofluid. 7*, 011807.

79. Peyman, S. A., Kwan, E. Y., Margarson, O., Iles, A., and Pamme, N. (2009) Diamagnetic repulsion—A versatile tool for label-free particle handling in microfluidic devices, *J. Chromatogr. A 1216*, 9055-9062.

80. Adams, J. D., Kim, U., and Soh, H. T. (2008) Multitarget magnetic activated cell sorter, *Proc. Natl. Acad. Sci. U.S.A. 105*, 18165-18170.

81. Lee, H., Jung, J., Han, S.-I., and Han, K.-H. (2010) High-speed RNA microextraction technology using magnetic oligo-dT beads and lateral magnetophoresis, *Lab Chip 10*, 2764-2770.

82. Shen, F., Hwang, H., Hahn, Y. K., and Park, J.-K. (2012) Label-Free Cell Separation Using a Tunable Magnetophoretic Repulsion Force, *Anal. Chem. 84*, 3075-3081.

83. Lou, X., Qian, J., Xiao, Y., Viel, L., Gerdon, A. E., Lagally, E. T., Atzberger, P., Tarasow, T. M., Heeger, A. J., and Soh, H. T. (2009) Micromagnetic selection of aptamers in microfluidic channels, *Proc. Natl. Acad. Sci. U.S.A. 106*, 2989-2994.

84. Pamme, N., and Wilhelm, C. (2006) Continuous sorting of magnetic cells via on-chip free-flow magnetophoresis, *Lab Chip 6*, 974-980.

85. Winkleman, A., Perez-Castillejos, R., Gudiksen, K. L., Phillips, S. T., Prentiss, M., and Whitesides, G. M. (2007) Density-Based Diamagnetic Separation: Devices for Detecting Binding Events and for Collecting Unlabeled Diamagnetic Particles in Paramagnetic Solutions, *Anal. Chem. 79*, 6542-6550.

86. Zhu, T., Cheng, R., Liu, Y., He, J., and Mao, L. (2014) Combining positive and negative magnetophoreses to separate particles of different magnetic properties, *Microfluid. Nanofluid. 17*, 973-982.

87. Hye-Kyoung, S., Yong-Ho, K., Hyun-Ok, K., and Yong-Jun, K. (2010) Hybrid cell sorters for on-chip cell separation by hydrodynamics and magnetophoresis, *J. Micromech.Microeng. 20*, 095019.

88. Kirby, D., Siegrist, J., Kijanka, G., Zavattoni, L., Sheils, O., O'Leary, J., Burger, R., and Ducrée, J. (2012) Centrifugo-magnetophoretic particle separation, *Microfluid. Nanofluid. 13*, 899-908.

89. Mizuno, M., Yamada, M., Mitamura, R., Ike, K., Toyama, K., and Seki, M. (2013) Magnetophoresis-Integrated Hydrodynamic Filtration System for Size- and Surface Marker-Based Two-Dimensional Cell Sorting, *Anal. Chem. 85*, 7666-7673.

90. Ozkumur, E., Shah, A. M., Ciciliano, J. C., Emmink, B. L., Miyamoto, D. T., Brachtel, E., Yu, M., Chen, P.-i., Morgan, B., and Trautwein, J. (2013) Inertial focusing for tumor antigen–dependent and–independent sorting of rare circulating tumor cells, *Sci. Transl. Med. 5*, 179ra147-179ra147.

91. Del Giudice, F., Madadi, H., Villone, M. M., D'Avino, G., Cusano, A. M., Vecchione, R., Ventre, M., Maffettone, P. L., and Netti, P. A. (2015) Magnetophoresis 'meets' viscoelasticity: deterministic separation of magnetic particles in a modular microfluidic device, *Lab Chip 15*, 1912-1922.

92. Yan, S., Zhang, J., Chen, H., Yuan, D., Alici, G., Du, H., Zhu, Y., and Li, W. (2016) Development of a novel magnetophoresis-assisted hydrophoresis microdevice for rapid particle ordering, *Biomed. Microdevices 18*, 1-9.

93. Lenshof, A., Magnusson, C., and Laurell, T. (2012) Acoustofluidics 8: Applications of acoustophoresis in continuous flow microsystems, *Lab Chip 12*, 1210-1223.

94. Augustsson, P., and Laurell, T. (2012) Acoustofluidics 11: affinity specific extraction and sample decomplexing using continuous flow acoustophoresis, *Lab Chip 12*, 1742-1752.

95. Collins, D. J., Alan, T., and Neild, A. (2014) Particle separation using virtual deterministic lateral displacement (vDLD), *Lab Chip 14*, 1595-1603.

96. Lenshof, A., and Laurell, T. (2010) Continuous separation of cells and particles in microfluidic systems, *Chem. Soc. Rev. 39*, 1203-1217.

97. Neuman, K. C., and Nagy, A. (2008) Single-molecule force spectroscopy: optical tweezers, magnetic tweezers and atomic force microscopy, *Nat. Meth. 5*, 491-505.

98. Ashkin, A. (1997) Optical trapping and manipulation of neutral particles using lasers, *Proc. Natl. Acad. Sci. U.S.A. 94*, 4853-4860.

99. Sajeesh, P., and Sen, A. K. (2013) Particle separation and sorting in microfluidic devices: a review, *Microfluid. Nanofluid.*, 1-52.

100. Jonáš, A., and Zemánek, P. (2008) Light at work: The use of optical forces for particle manipulation, sorting, and analysis, *Electrophoresis 29*, 4813-4851.

101. Perroud, T. D., Kaiser, J. N., Sy, J. C., Lane, T. W., Branda, C. S., Singh, A. K., and Patel, K. D. (2008) Microfluidic-Based Cell Sorting of Francisella tularensis Infected Macrophages Using Optical Forces, *Anal. Chem. 80*, 6365-6372.

102. MacDonald, M. P., Spalding, G. C., and Dholakia, K. (2003) Microfluidic sorting in an optical lattice, *Nature 426*, 421-424.

103. Yamada, M., Nakashima, M., and Seki, M. (2004) Pinched flow fractionation: Continuous size separation of particles utilizing a laminar flow profile in a pinched microchannel, *Anal. Chem. 76*, 5465-5471.

104. Lee, K. H., Kim, S. B., Lee, K. S., and Sung, H. J. (2011) Enhancement by optical force of separation in pinched flow fractionation, *Lab Chip 11*, 354-357.

105. Lau, A. Y., Lee, L. P., and Chan, J. W. (2008) An integrated optofluidic platform for Raman-activated cell sorting, *Lab Chip 8*, 1116-1120.

106. Wu, M. C. (2011) Optoelectronic tweezers, *Nat Photon 5*, 322-324.

107. Chiou, P. Y., Ohta, A. T., and Wu, M. C. (2005) Massively parallel manipulation of single cells and microparticles using optical images, *Nature 436*, 370-372.

108. Hwang, H., and Park, J.-K. (2011) Optoelectrofluidic platforms for chemistry and biology, *Lab Chip 11*, 33-47.

109. Birch, C. M., Hou, H. W., Han, J., and Niles, J. C. (2015) Identification of malaria parasite-infected red blood cell surface aptamers by inertial microfluidic SELEX (I-SELEX), *Scientific Reports 5*, 11347.

110. Kim, Y.-G., Moon, S., Kuritzkes, D. R., and Demirci, U. (2009) Quantum dot-based HIV capture and imaging in a microfluidic channel, *Biosens. Bioelectron. 25*, 253-258.

111. Rainer, T. H., Wong, L. K., Lam, W., Yuen, E., Lam, N. Y., Metreweli, C., and Lo, Y. D. (2003) Prognostic use of circulating plasma nucleic acid concentrations in patients with acute stroke, *Clin. Chem. 49*, 562-569.

112. Yan, S., Zhang, J., Alici, G., Du, H., Zhu, Y., and Li, W. (2014) Isolating plasma from blood using a dielectrophoresis-active hydrophoretic device, *Lab Chip 14*, 2993-3003.

113. Gupta, G. P., and Massagué, J. (2006) Cancer Metastasis: Building a Framework, *Cell 127*, 679-695.

114. Aggarwal, C., Meropol, N. J., Punt, C. J., Iannotti, N., Saidman, B. H., Sabbath, K. D., Gabrail, N. Y., Picus, J., Morse, M. A., Mitchell, E., Miller, M. C., and

Cohen, S. J. (2013) Relationship among circulating tumor cells, CEA and overall survival in patients with metastatic colorectal cancer, *Ann. Oncol. 24*, 420-428.

115. Lianidou, E. S., Strati, A., and Markou, A. (2014) Circulating tumor cells as promising novel biomarkers in solid cancers, *Crit. Rev. Clin. Lab. Sci. 51*, 160-171.

116. Qin, X., Park, S., Duffy, S. P., Matthews, K., Ang, R. R., Todenhofer, T., Abdi, H., Azad, A., Bazov, J., Chi, K. N., Black, P. C., and Ma, H. (2015) Size and deformability based separation of circulating tumor cells from castrate resistant prostate cancer patients using resettable cell traps, *Lab Chip 15*, 2278-2286.

117. Jin, C., McFaul, S. M., Duffy, S. P., Deng, X., Tavassoli, P., Black, P. C., and Ma, H. (2014) Technologies for label-free separation of circulating tumor cells: from historical foundations to recent developments, *Lab Chip 14*, 32-44.

118. (2007) Computational modeling and comparison of three co-laminar microfluidic mixing techniques, *Microfluid. Nanofluid.*

119. Sajay, B., Chang, C.-P., Ahmad, H., Khuntontong, P., Wong, C., Wang, Z., Puiu, P., Soo, R., and Rahman, A. (2014) Microfluidic platform for negative enrichment of circulating tumor cells, *Biomed. Microdevices 16*, 537-548.

120. Zhu, T., Cheng, R., Lee, S. A., Rajaraman, E., Eiteman, M. A., Querec, T. D., Unger, E. R., and Mao, L. (2012) Continuous-flow ferrohydrodynamic sorting of particles and cells in microfluidic devices, *Microfluid. Nanofluid. 13*, 645-654.

121. Zhao, W., Zhu, T., Cheng, R., Liu, Y., He, J., Qiu, H., Wang, L., Nagy, T., Querec, T. D., and Unger, E. R. (2015) Label-Free and Continuous-Flow Ferrohydrodynamic Separation of HeLa Cells and Blood Cells in Biocompatible Ferrofluids, *Adv. Funct. Mater.*

122. Park, S., Zhang, Y., Wang, T.-H., and Yang, S. (2011) Continuous dielectrophoretic bacterial separation and concentration from physiological media of high conductivity, *Lab Chip 11*, 2893-2900.

123. Yan, S., Zhang, J., Chen, H., Alici, G., Du, H., Zhu, Y., and Li, W. (2014) Making a hydrophoretic focuser tunable using a diaphragm, *Biomicrofluid. 8*, 064115.

124. Cheng, I. F., Huang, W.-L., Chen, T.-Y., Liu, C.-W., Lin, Y.-D., and Su, W.-C. (2015) Antibody-free isolation of rare cancer cells from blood based on 3D lateral dielectrophoresis, *Lab Chip 15*, 2950-2959.

125. Hou, H. W., Warkiani, M. E., Khoo, B. L., Li, Z. R., Soo, R. A., Tan, D. S.-W., Lim, W.-T., Han, J., Bhagat, A. A. S., and Lim, C. T. (2013) Isolation and retrieval of circulating tumor cells using centrifugal forces, *Sci. Rep. 3*.

126. Chen, H., Sun, J., Wolvetang, E., and Cooper-White, J. (2015) High-throughput, deterministic single cell trapping and long-term clonal cell culture in microfluidic devices, *Lab Chip 15*, 1072-1083.

127. Chan, C. Y., Huang, P.-H., Guo, F., Ding, X., Kapur, V., Mai, J. D., Yuen, P. K., and Huang, T. J. (2013) Accelerating drug discovery via organs-on-chips, *Lab Chip 13*, 4697-4710.

128. Zhao, H., Zhou, L., Zhang, Q., Zhou, X., Zhang, Y., Chen, H., and Du, Y. (2015) Bi-content micro-collagen chip provides contractility-based biomechanical readout for phenotypic drug screening with expanded and profiled targets, *Lab Chip 15*, 3481-3494.

129. Park, S. (2011) Continuous dielectrophoretic bacterial separation and concentration from physiological media of high conductivity, *Lab Chip 11*, 2893-2900.

130. Xuan, X. (2010) Particle focusing in microfluidic devices, *Microfluid. Nanofluid. 9*, 1-16.

131. Markx, G. H. (1994) Separation of viable and non-viable yeast using dielectrophoresis, *J. Biotechnol. 32*, 29-37.

132. Huang, Y., Wang, X. B., Becker, F. F., and Gascoyne, P. R. (1997) Introducing dielectrophoresis as a new force field for field-flow fractionation, *Biophys. J. 73*, 1118-1129.

133. Cheng, I. F. (2009) A continuous high-throughput bioparticle sorter based on 3D traveling-wave dielectrophoresis, *Lab Chip 9*, 3193-3201.

134. Regtmeier, J., Eichhorn, R., Viefhues, M., Bogunovic, L., and Anselmetti, D. (2011) Electrodeless dielectrophoresis for bioanalysis: Theory, devices and applications, *Electrophoresis 32*, 2253-2273.

135. Choi, S., Karp, J. M., and Karnik, R. (2012) Cell sorting by deterministic cell rolling, *Lab Chip 12*, 1427-1430.

136. Zhang, J. (2013) Inertial focusing in a straight channel with asymmetrical expansion–contraction cavity arrays using two secondary flows, *J. Micromech.Microeng. 23*, 085023.

137. Li, M., Li, S., Wu, J., Wen, W., Li, W., and Alici, G. (2012) A simple and cost-effective method for fabrication of integrated electronic-microfluidic devices using a laser-patterned PDMS layer, *Microfluid. Nanofluid. 12*, 751-760.

138. Sharp, K. V., and Adrian, R. J. (2004) Transition from laminar to turbulent flow in liquid filled microtubes, *Exp. Fluids 36*, 741-747.

139. Pethig, R. (2003) Enhancing traveling-wave dielectrophoresis with signal superposition, *IEEE Eng. Med. Biol. Mag. 22*, 43-50.

140. Kersaudy-Kerhoas, M. (2010) Hydrodynamic blood plasma separation in microfluidic channels, *Microfluid. Nanofluid. 8*, 105-114.

141. Tachi, T. (2009) Simultaneous Separation, Metering, and Dilution of Plasma from Human Whole Blood in a Microfluidic System, *Anal. Chem. 81*, 3194-3198.

142. Thorslund, S. (2006) A hybrid poly(dimethylsiloxane) microsystem for on-chip whole blood filtration optimized for steroid screening, *Biomed. Microdevices 8*, 73-79.

143. Moorthy, J. (2003) In situ fabricated porous filters for microsystems, *Lab Chip 3*, 62.

144. Lee, D. S., Choi, Y. H., Han, Y. D., Yoon, H. C., Shoji, S., and Jung, M. Y. (2012) Construction of membrane sieves using stoichiometric and stress-reduced Si 3N 4/SiO 2/Si 3N 4 multilayer films and their applications in blood plasma separation, *ETRI Journal 34*, 226-234.

145. Yang, S. (2006) A microfluidic device for continuous, real time blood plasma separation, *Lab Chip 6*, 871.

146. Zhang, J., Li, W., Li, M., Alici, G., and Nguyen, N. T. (2013) Particle inertial focusing and its mechanism in a serpentine microchannel, *Microfluid. Nanofluid.*, 1-12.

147. Mach, A. J., and Di Carlo, D. (2010) Continuous Scalable Blood Filtration Device Using Inertial Microfluidics, *Biotechnol. Bioeng. 107*, 302-311.

148. Nakashima, Y., Hata, S., and Yasuda, T. (2010) Blood plasma separation and extraction from a minute amount of blood using dielectrophoretic and capillary forces, *Sens. Actuators, B 145*, 561-569.

149. Yan, S., Li, W., Zhang, J., Li, M., Alici, G., Du, H., and Sluyter, R. (submitted.) *Sci. Rep.*

150. Zhang, J., Li, M., Li, W. H., and Alici, G. (2013) Inertial focusing in a straight channel with asymmetrical expansion-contraction cavity arrays using two secondary flows, *J. Micromech.Microeng. 23*.

151. Landau, L., and Lifshitz, E. (1987) *Fluid mechanics*, Vol. vol. 6.

152. Zborowski, M., Ostera, G. R., Moore, L. R., Milliron, S., Chalmers, J. J., and Schechter, A. N. (2003) Red blood cell magnetophoresis, *Biophys. J. 84*, 2638-2645.

153. Li, M., Li, S., Li, W., Wen, W., and Alici, G. (2013) Continuous manipulation and separation of particles using combined obstacle- and curvature-induced direct current dielectrophoresis, *Electrophoresis 34*, 952-960.

154. Han, K.-H., Han, S.-I., and Frazier, A. B. (2009) Lateral displacement as a function of particle size using a piecewise curved planar interdigitated electrode array, *Lab Chip 9*, 2958-2964.

155. Han, K.-H., and Frazier, A. B. (2008) Lateral-driven continuous dielectrophoretic microseparators for blood cells suspended in a highly conductive medium, *Lab Chip 8*, 1079-1086.

156. Adams, J. D., and Soh, H. T. (2010) Tunable acoustophoretic band-pass particle sorter, *Appl. Phys. Lett. 97*.

157. Pamme, N., Eijkel, J. C. T., and Manz, A. (2006) On-chip free-flow magnetophoresis: Separation and detection of mixtures of magnetic particles in continuous flow, *J. Magn. Magn. Mater. 307*, 237-244.

158. Inglis, D. W., Riehn, R., Austin, R. H., and Sturm, J. C. (2004) Continuous microfluidic immunomagnetic cell separation, *Appl. Phys. Lett. 85*, 5093-5095.

159. Zhang, J., Yan, S., Sluyter, R., Li, W., Alici, G., and Nguyen, N.-T. (2014) Inertial particle separation by differential equilibrium positions in a symmetrical serpentine micro-channel, *Sci. Rep. 4*.

160. Choi, S., Levy, O., Coelho, M. B., Cabral, J. M. S., Karp, J. M., and Karnik, R. (2014) A cell rolling cytometer reveals the correlation between mesenchymal stem cell dynamic adhesion and differentiation state, *Lab Chip 14*, 161-166.

161. Ng, E., Hoshino, K., and Zhang, X. (2013) Microfluidic immunodetection of cancer cells via site-specific microcontact printing of antibodies on nanoporous surface, *Methods 63*, 266-275.

162. Han, J., Fu, J., and Schoch, R. B. (2007) Molecular sieving using nanofilters: Past, present and future, *Lab Chip 8*, 23-33.

163. Braasch, K., Nikolic-Jaric, M., Cabel, T., Salimi, E., Bridges, G. E., Thomson, D. J., and Butler, M. (2013) The changing dielectric properties of CHO cells can be used to determine early apoptotic events in a bioprocess, *Biotechnol. Bioeng. 110*, 2902-2914.

164. Zhou, J., Giridhar, P. V., Kasper, S., and Papautsky, I. (2013) Modulation of aspect ratio for complete separation in an inertial microfluidic channel, *Lab Chip 13*, 1919-1929.

165. Loutherback, K., D'Silva, J., Liu, L., Wu, A., Austin, R. H., and Sturm, J. C. (2012) Deterministic separation of cancer cells from blood at 10 mL/min, *AIP Advances 2*.

166. Hu, X., Bessette, P. H., Qian, J., Meinhart, C. D., Daugherty, P. S., and Soh, H. T. (2005) Marker-specific sorting of rare cells using dielectrophoresis, *Proc. Natl. Acad. Sci. U. S. A. 102*, 15757-15761.

167. Zhu, K., Kaprelyants, A. S., Salina, E. G., and Markx, G. H. (2010) Separation by dielectrophoresis of dormant and nondormant bacterial cells of Mycobacterium smegmatis, *Biomicrofluid. 4*.

168. Shafiee, H., Caldwell, J. L., Sano, M. B., and Davalos, R. V. (2009) Contactless dielectrophoresis: A new technique for cell manipulation, *Biomed. Microdevices 11*, 997-1006.

169. Shen, S., Ma, C., Zhao, L., Wang, Y., Wang, J.-C., Xu, J., Li, T., Pang, L., and Wang, J. (2014) High-throughput rare cell separation from blood samples using steric hindrance and inertial microfluidics, *Lab Chip*.

170. Kawaguchi, H. (2000) Functional polymer microspheres, *Prog. Polym. Sci. 25*, 1171-1210.

171. Tan, W.-H., and Takeuchi, S. (2007) A trap-and-release integrated microfluidic system for dynamic microarray applications, *Proc. Natl. Acad. Sci. U.S.A. 104*, 1146-1151.

172. Crosland-Taylor, P. J. (1953) A Device for Counting Small Particles suspended in a Fluid through a Tube, *Nature 171*, 37-38.

173. áHowell Jr, P. B. (2008) Two simple and rugged designs for creating microfluidic sheath flow, *Lab Chip 8*, 1097-1103.

174. Kim, J. S., Anderson, G. P., Erickson, J. S., Golden, J. P., Nasir, M., and Ligler, F. S. (2009) Multiplexed detection of bacteria and toxins using a microflow cytometer, *Anal. Chem. 81*, 5426-5432.

175. Golden, J. P., Kim, J. S., Erickson, J. S., Hilliard, L. R., Howell, P. B., Anderson, G. P., Nasir, M., and Ligler, F. S. (2009) Multi-wavelength microflow cytometer using groove-generated sheath flow, *Lab Chip 9*, 1942-1950.

176. Thangawng, A. L., Kim, J. S., Golden, J. P., Anderson, G. P., Robertson, K. L., Low, V., and Ligler, F. S. (2010) A hard microflow cytometer using groove-generated sheath flow for multiplexed bead and cell assays, *Anal. Bioanal. Chem. 398*, 1871-1881.

177. Choi, S., Song, S., Choi, C., and Park, J.-K. (2009) Microfluidic Self-Sorting of Mammalian Cells to Achieve Cell Cycle Synchrony by Hydrophoresis, *Anal. Chem. 81*, 1964-1968.

178. Song, S., Kim, M. S., and Choi, S. (2014) Smart Microfluidic Pipette Tip Enabled by Flow-Rate Insensitive Particle Ordering, *Small 10*, 4123-4129.

179. Sheng, Y., Jun, Z., Chao, P., Dan, Y., Gursel, A., Haiping, D., Yonggang, Z., and Weihua, L. (2015) An integrated dielectrophoresis-active hydrophoretic microchip for continuous particle filtration and separation, *J. Micromech.Microeng. 25*, 084010.

180. Robert, D., Pamme, N., Conjeaud, H., Gazeau, F., Iles, A., and Wilhelm, C. (2011) Cell sorting by endocytotic capacity in a microfluidic magnetophoresis device, *Lab Chip 11*, 1902-1910.

181. Plouffe, B. D., Lewis, L. H., and Murthy, S. K. (2011) Computational design optimization for microfluidic magnetophoresis, *Biomicrofluid. 5*, 013413.

182. Forbes, T. P., and Forry, S. P. (2012) Microfluidic magnetophoretic separations of immunomagnetically labeled rare mammalian cells, *Lab Chip 12*, 1471-1479.

183. Kose, A. R., Fischer, B., Mao, L., and Koser, H. (2009) Label-free cellular manipulation and sorting via biocompatible ferrofluids, *Proc. Natl. Acad. Sci. U.S.A. 106*, 21478-21483.

184. Rodriguez-Villarreal, A. I., Tarn, M. D., Madden, L. A., Lutz, J. B., Greenman, J., Samitier, J., and Pamme, N. (2011) Flow focussing of particles and cells based on their intrinsic properties using a simple diamagnetic repulsion setup, *Lab Chip 11*, 1240-1248.

185. Zhu, T., Cheng, R., and Mao, L. (2011) Focusing microparticles in a microfluidic channel with ferrofluids, *Microfluid. Nanofluid. 11*, 695-701.

186. Hejazian, M., Li, W., and Nguyen, N.-T. (2015) Lab on a chip for continuous-flow magnetic cell separation, *Lab Chip 15*, 959-970.

187. Massey, B. (1989) Mechanics of Fluids Chapman Hall, *London, UK*.

188. Kim, S., Han, S.-I., Park, M.-J., Jeon, C.-W., Joo, Y.-D., Choi, I.-H., and Han, K.-H. (2013) Circulating Tumor Cell Microseparator Based on Lateral Magnetophoresis and Immunomagnetic Nanobeads, *Anal. Chem. 85*, 2779-2786.

189. Lin, Y.-H., Wang, C.-C., and Lei, K. F. (2014) Bubble-driven mixer integrated with a microfluidic bead-based ELISA for rapid bladder cancer biomarker detection, *Biomed. Microdevices 16*, 199-207.

190. Ng, A. H. C., Uddayasankar, U., and Wheeler, A. R. (2010) Immunoassays in microfluidic systems, *Anal. Bioanal. Chem. 397*, 991-1007.

191. Shin, J. H., Lee, M. G., Choi, S., and Park, J.-K. (2014) Inertia-activated cell sorting of immune-specifically labeled cells in a microfluidic device, *RSC Advances 4*, 39140-39144.

192. Kim, M. S., Sim, T. S., Kim, Y. J., Kim, S. S., Jeong, H., Park, J.-M., Moon, H.-S., Kim, S. I., Gurel, O., and Lee, S. S. (2012) SSA-MOA: a novel CTC isolation platform using selective size amplification (SSA) and a multi-obstacle architecture (MOA) filter, *Lab Chip 12*, 2874-2880.

193. Shields IV, C. W., Johnson, L. M., Gao, L., and López, G. P. (2014) Elastomeric negative acoustic contrast particles for capture, acoustophoretic transport, and confinement of cells in microfluidic systems, *Langmuir 30*, 3923-3927.

194. Yasukawa, T., Suzuki, M., Sekiya, T., Shiku, H., and Matsue, T. (2007) Flow sandwich-type immunoassay in microfluidic devices based on negative dielectrophoresis, *Biosens. Bioelectron. 22*, 2730-2736.

195. Xia, N., Hunt, T. P., Mayers, B. T., Alsberg, E., Whitesides, G. M., Westervelt, R. M., and Ingber, D. E. (2006) Combined microfluidic-micromagnetic separation of living cells in continuous flow, *Biomed. Microdevices 8*, 299-308.

196. Del Giudice, F., Madadi, H., Villone, M. M., D'Avino, G., Cusano, A. M., Vecchione, R., Ventre, M., Maffettone, P. L., and Netti, P. A. (2015) Magnetophoresis 'meets' viscoelasticity: deterministic separation of magnetic particles in a modular microfluidic device, *Lab Chip 15*, 1912-1922.

197. Stroock, A. D. (2002) Chaotic Mixer for Microchannels, *Science 295*, 647-651.

198. Gadish, N., and Voldman, J. (2006) High-throughput positive-dielectrophoretic bioparticle microconcentrator, *Anal. Chem. 78*, 7870-7876.

199. Hsu, C. H., Di Carlo, D., Chen, C., Irimia, D., and Toner, M. (2008) Microvortex for focusing, guiding and sorting of particles, *Lab Chip 8*, 2128-2134.

200. Lu, X., Zhu, L., Hua, R.-m., and Xuan, X. (2015) Continuous sheath-free separation of particles by shape in viscoelastic fluids, *Appl. Phys. Lett. 107*, 264102.

201. Warkiani, M. E., Tay, A. K. P., Guan, G., and Han, J. (2015) Membrane-less microfiltration using inertial microfluidics, *Scientific reports 5*.

Publications

1. **Sheng Yan**, Jun Zhang, Huaying Chen, Dan Yuan, Gursel Alici, Haiping Du, Yonggang Zhu, Weihua Li, Development of a novel magnetophoresis-assisted hydrophoresis microdevice for rapid particle ordering. ***Biomedical Microdevices***, 18, 1-9, 2016.

2. **Sheng Yan**, Jun Zhang, Chao Pan, Dan Yuan, Gursel Alici, Haiping Du, Yonggang Zhu, Weihua Li, An integrated dielectrophoresis-active hydrophoretic microchip for continuous particle filtration and separation. ***Journal of Micromechanics and Microengineering,*** 25, 084010, 2015.

3. **Sheng Yan**, Jun Zhang, Yuan Yuan, George Lovrecz, Gursel Alici, Haiping Du, Yonggang Zhu, Weihua Li, A hybrid dielectrophoretic and hydrophoretic microchip for particle sorting using integrated prefocusing and sorting steps. ***Electrophoresis***, 36, 284-291, 2015.

4. **Sheng Yan**, Jun Zhang, Huaying Chen, Gursel Alici, Haiping Du, Yonggang Zhu, Weihua Li, Making a hydrophoretic focuser tunable using a diaphragm. ***Biomicrofluidics***, 8, 064115, 2014.

5. **Sheng Yan**, Jun Zhang, Gursel Alici, Haiping Du, Yonggang Zhu, Weihua Li, Isolating plasma from blood using a dielectrophoresis-active hydrophoretic device. ***Lab on a Chip***, 14, 2993-3003, 2014.

6. **Sheng Yan**, Jun Zhang, Ming Li, Gursel Alici, Haiping Du, Ronald Sluyter, Weihua Li, On-chip high-throughput manipulation of particles in a dielectrophoresis-active hydrophoretic focuser. ***Scientific Reports***, 4, 5060, 2014.

7. Tiantian Jin, **Sheng Yan**, Jun Zhang, Dan Yuan, Xu-Feng Huang, Weihua Li, A label-free and high-throughput separation of neuron and glial cells using an inertial microfluidic platform. ***Biomicrofluidics***, 10, 034104, 2016.

8. Dan Yuan, Jun Zhang, **Sheng Yan**, Gangrou Peng, Qianbin Zhao, Gursel Alici, Hejun Du, Weihua Li, Investigation of particle lateral migration in sample-sheath

flow of viscoelastic fluid and Newtonian fluid. ***Electrophoresis***, 37, 2147-2155, 2016.

9. Jun Zhang, **Sheng Yan**, Dan Yuan, Gursel Alici, Nam-Trung Nguyen, Majid Ebrahimi Warkiani, Weihua Li, Fundamentals and Applications of Inertial Microfluidics: A Review. ***Lab on a Chip***, 16, 10-34, 2016.

10. Dan Yuan, Jun Zhang, **Sheng Yan**, Chao Pan, Gursel Alici, Nam-Trung Nguyen, Weihua Li, Dean-flow-coupled elasto-inertial three-dimensional particle focusing under viscoelastic flow in a straight channel with asymmetrical expansion-contraction cavity arrays. ***Biomicrofluidics***, 9, 044108, 2015.

11. Jun Zhang, **Sheng Yan**, Gursel Alici, Nam-Trung Nguyen, Dino Di Carlo, Weihua Li, Real-time control of inertial focusing in microfluidics using dielectrophoresis (DEP). ***RSC Advances***, 4, 62076-62084.

12. Jun Zhang, **Sheng Yan**, Weihua Li, Gursel Alici, Nam-Trung Nguyen: High throughput extraction of plasma using a secondary flow-aided inertial microfluidic device. ***RSC Advances***, 4, 33149-33159, 2014.

13. Jun Zhang, **Sheng Yan**, Ronald Sluyter, Weihua Li, Gursel Alici, Nam-Trung Nguyen, Inertial particle separation by differential equilibrium positions in a symmetrical serpentine micro-channel. ***Scientific Reports***, 4, 4527, 2014.

14. Dan Yuan, Jun Zhang, Ronald Sluyter, Qianbin Zhao, **Sheng Yan**, Gursel Alici, Weihua Li, Continuous plasma extraction under viscoelastic fluid in a straight channel with asymmetrical expansion–contraction cavity arrays. ***Lab on a Chip***, in press.

15. Jun Zhang, **Sheng Yan**, Dan Yuan, Qianbin Zhao, Say Hwa Tan, Nam-Trung Nguyen, Weihua Li, A novel viscoelastic-based ferrofluid for continuous sheath-less microfluidic separation of nonmagnetic microparticles. ***Lab on a Chip***, accepted.

16. Fengli Liu, Jun Zhang, Gursel Alici, **Sheng Yan**, Rahim Mutlu, Weihua Li, Tianhong Yan, An inverted micro-mixer based on a magnetically-actuated cilium made of Fe doped PDMS. ***Smart materials and structures***, 2016, accepted.

17. **Sheng Yan**, Jun Zhang, Weihua Li, Hybrid microfluidics combined with active and passive approaches for continuous cell separation, submitted.

18. **Sheng Yan**, Jun Zhang, Dan Yuan, Qianbin Zhao, Junqi Ma, Weihua Li, High-throughput, sheathless, magnetophoretic separation of magnetic and non-magnetic particles with a groove-based channel, submitted.

19. Qianbin Zhao, Jun Zhang, **Sheng Yan**, Dan Yuan, Haiping Du, Gursel Alici, and Weihua Li, High-throughput sheathless and three-dimensional microparticle focusing using a microchannel with arc-shaped groove arrays, submitted.

20. Dan Yuan, Jun Zhang, Say Hwa Tan, **Sheng Yan**, Qianbin Zhao, Ronald Sluyter, Nam-Trung Nguyen, and Weihua Li, Sheathless Dean-flow-coupled elasto-inertial particle focusing and separation in viscoelastic fluid, submitted.